UNIVERSITY OF CALIFORNIA

Los Angeles

Direct Laser Acceleration in Laser Wakefield Accelerators

A thesis submitted in partial satisfaction

of the requirements for the degree of Doctor of Philosophy

in Electrical Engineering

by

Jessica Leigh Shaw

2016

ABSTRACT OF THE DISSERTATION

Direct Laser Acceleration in Laser Wakefield Accelerators

by

Jessica Leigh Shaw

Doctor of Philosophy in Electrical Engineering

University of California, Los Angeles, 2016

Professor Chandra J. Joshi, Chair

In this dissertation, the direct laser acceleration (DLA) of ionization-injected electrons in a laser wakefield accelerator (LWFA) operating in the quasi-blowout regime has been investigated through experiment and simulation. In the blowout regime of LWFA, the radiation pressure of an intense laser pulse can push a majority of the plasma electrons out and around the main body of the pulse. The expelled plasma electrons feel the electrostatic field of the relatively-stationary ions and are thus attracted back towards the laser axis behind the laser pulse where they overshoot the axis and set up a wake oscillation. When ionization injection is used, the inner-shell electrons of higher-Z dopant atoms are tunnel ionized near the peak of the laser pulse. Those electrons slip back relative to the wake until they gain enough energy from the longitudinal wakefield to become trapped. Those electrons that are trapped off-axis will undergo betatron oscillations in response to the linear transverse focusing force of the ions. Through experiments and supporting simulations, this dissertation demonstrates that when there is a

significant overlap between the drive laser and the trapped electrons in a LWFA cavity, the accelerating electrons can gain energy from the DLA mechanism in addition to LWFA.

When laser pulse overlaps the trapped electrons, the betatron oscillations of the electrons in the plane of the laser polarization can lead to an energy transfer from the transverse electric field of the laser to the transverse momentum of the electrons. This enhanced transverse momentum can then be converted into increased longitudinal momentum via the **v** x **B** force of the laser. This process is known as DLA. In this experimental work, the properties of the electron beams produced in a LWFA where the electrons are injected by ionization injection and become trapped without escaping the laser field have been investigated. The maximum measured energy of the produced electron beams scales with the overlap between the electrons and the laser. Undispersed electrons beams are observed to be elliptical in the plane of the laser polarization, and the energy spectrum splits into a fork at higher energies when the electrons beams are dispersed orthogonal to the direction of the laser polarization. These characteristic features are reproduced in particle-in-cell (PIC) code simulations where particle tracking was used to demonstrate that such spectral features are signatures of the presence of DLA in LWFA.

Further PIC simulations comparing LWFA with and without DLA show that the presence of DLA can lead to electron beams that have maximum energies that exceed the estimates given by the theory for the ideal blowout regime. The magnitude of the contribution of DLA to the energy gained by the electron was found to be on the order of the LWFA contribution. In the LWFAs studied here, both DLA and LWFA participate in accelerating the bulk of the electrons in the produced electron beam. The presence of DLA in a LWFA can also lead to enhanced betatron oscillation amplitudes and increased divergence in the direction of the laser polarization.

The dissertation of Jessica Leigh Shaw is approved.

Warren B. Mori

Pietro Musumeci

Oscar M. Stafsudd

Chandra J. Joshi, Committee Chair

University of California, Los Angeles

2016

Table of Contents

List of Figures

Chapter 1

Chapter 2

Chapter 3

Chapter 4

Chapter 5

Acknowledgements

This dissertation would not be possible without the support and guidance of the excellent scientists that I have worked with during my time at UCLA. I would like to thank Professor Chan Joshi for his support and guidance over the years, for taking us students to many conferences, and especially for the hours and hours of meetings, discussions, and editing sessions that have allowed me to publish papers as a graduate student. I would like to thank Ken Marsh for six years of unwavering support whether it helping me navigate classes or interpreting simulation results or spending days in the lab getting the data that I needed. I would like to thank Nuno Lemos for teaching me how to use OSIRIS even before he came to UCLA and for being my constant lab companion for the last three years. From our time traveling for experiments to the late nights at UCLA, I could not have asked to work with anyone better. I would have never survived grad school without my fellow grad students Jeremy Pigeon and Navid Vafaei-Najafabadi, and so I would like to thank them as well for being there for all the late night homework sessions, the prelim preparation, and help with my experimental work. I also would like to extend my thanks to Ligia Diana Amorim, who helped bring the final simulations for my dissertation to fruition. I would also like to thank the UCLA Plasma Simulation group, especially Weiming An, Frank Tsung, and Professor Warren Mori, for their support of my simulation work. I would also like to thank our collaborators at Lawrence Livermore Nation Laboratory, especially Brad Pollock, Felicie Albert, Art Pak, and Joe Ralph. Finally, I would like to thank all my friends and family who have supported me through the Ph.D. process.

Vita

EDUCATION

University of California at Los Angeles, Los Angeles CA
M.Sc. in Electrical Engineering: Plasma Physics and Laser Acceleration of Particles March 2013
Thesis: Characterization of Sub-millimeter-scale Gas Cells as Possible Injectors for Staged Laser Wakefield Acceleration
Thesis Chair: Distinguished Chancellor's Professor C. Joshi
Cumulative GPA: 3.91/4:00

Villanova University, Villanova PA
B.Sc.: Civil and Environmental Engineering May 2010
B.A.: Physics May 2010
Cumulative GPA: 3.99/4:00; Graduated Summa Cum Laude

RESEARCH

University of California Los Angeles Laser Plasma Accelerator Group 2010—Present
Experimental: Design and execute experiments to improve plasma-based electron acceleration and x-ray production using direct laser acceleration and laser wakefield acceleration (LWFA). Operate the laser for these experiments. Develop gas cell targets for LWFA experiments. Construct heat-pipe-oven plasma targets for plasma wakefield experiments. Analyze data from experiments and present or publish results. Mentor junior graduate students.
Simulation: Write, run, and analyze 2D and 3D simulations of laser wakefield acceleration, direct laser acceleration, and plasma wakefield acceleration using the particle-in-cell codes OSIRIS and QuickPIC. Use these simulations to explore new physics ideas for experiments, aid in design of experimental diagnostics, and support experimental results.

Collaboration with Lawrence Livermore National Laboratory 2010—Present
Experimental: Design, setup, and execute large-scale collaborative experimental campaigns on the Jupiter Laser Facility, and then analyze data from these campaigns. Managed day-to-day tasks and laser shots on two experiments. Campaigns have investigated electron and x-ray production in the self-modulated and blowout laser wakefield acceleration regimes and ion production in the blowout laser wakefield acceleration regime.
Simulation: Support the collaboration's experiments by running 2D simulations of laser wakefield acceleration using the code particle-in-cell code OSIRIS.

Lawrence Livermore National Laboratory Plasma Physics Group Internship 2009-2010
Installed novel optical diagnostic to track laser evolution within plasma and developed x-ray diagnostic for imaging plasmas produced in laser wakefield acceleration experiments in the Jupiter Laser Facility. Provided experimental support for Thomson scattering experiments and laser wakefield acceleration experiments, including set-up, component design, data collection, and analysis.

HONORS

Fellowships
University of California of Los Angeles Dissertation Year Fellow Present
University of California of Los Angeles Cota-Robles Fellow 2010—Present
Lawrence Postdoctoral Fellow, Lawrence Livermore National Laboratory (Declined) 2016
Truman Postdoctoral Fellowship, Sandia National Laboratory (Declined) 2016
National Science Foundation Fellow 2010—2015
National Defense Science & Engineering Graduate Fellow 2010—2013
National Nuclear Security Administration Fellowship Finalist (Declined) 2010
Fusion Energy Sciences Fellowship Finalist (Declined) 2010
SMART Fellowship Semi-Finalist 2010

Fellowships, Continued

Hertz Applied Science Fellowship Finalist	2009

Awards

2013 North American Particle Accelerator Conference Best Student Poster	2013
2010 Lawrence Livermore National Laboratory Summer Internship Best Student Poster	2010
Villanova University College of Engineering Dean's Award for Academic Excellence	2010
Villanova University College of Liberal Arts & Science Gregor Mendel Medal	2010
Villanova University Physics Department Medal	2010
Who's Who of Villanova University	2010
Dept. of Energy's Science and Energy Research Challenge Poster Competition Finalist	2009
2009 Lawrence Livermore National Laboratory Summer Internship Best Student Poster	2009
Girl Scout Gold Award	2005

Scholarships

Lockheed Martin Society of Women Engineers Scholarship	2009—2010
Morris K. Udall Scholarship Program Honorable Mention	2009
National Academy of Nuclear Training Scholarship	2008
Villanova University Presidential Scholar	2005—2010

Honorary Societies

Phi Beta Kappa Honor Society	2009—Present
Who's Who in American Universities and Colleges	2009
Sigma Pi Sigma Honor Society	2008—Present
Tau Beta Pi Honor Society (Chapter President 2008-2009)	2007—Present
Chi Epsilon Honor Society (Chapter Editor 2008-2009)	2007—Present
Phi Kappa Phi Honor Society	2007—2008
National Society of Collegiate Scholars	2006—Present

SELECTED PUBLISHED PAPERS IN PEER-REVIEWED JOURNALS

1. **J. L. Shaw**, N. Lemos, K. A. Marsh, F. S. Tsung, W. B. Mori, and C. Joshi, "Estimation of direct laser acceleration in laser wakefield accelerators using particle-in-cell simulations," Plasma Phys. Contr. F. **58**, 034008 (2016).
2. N. Lemos, J. L. Martins, **J. L. Shaw**, F. S. Tsung, K. A. Marsh, F. Albert, B. B. Pollock, and C. Joshi, "Self-modulated laser wakefield accelerators as x-ray sources," Plasma Phys. Contr. F. **58**, 034018 (2016).
3. B. B. Pollock, F. S. Tsung, F. Albert, **J. L. Shaw**, C. E. Clayton, A. Davidson, N. Lemos, K. A. Marsh, A. Pak, J. E. Ralph, W. B. Mori, and C. Joshi, "Formation of ultra-relativistic electron rings from a laser wakefield accelerators," Phys. Rev. Lett. **115**, 055004 (2015).
4. W. Luo, F. Shabbir, C. Gong, C. Gulec, J. Pigeon, **J. L. Shaw**, A. Greenbaum, S. Tochitsky, C. Joshi, and A. Ozcan, "High throughput on-chip analysis of high-energy charged particle tracks using lensfree imaging," Appl. Phys. Lett. **106**, 151107 (2015).
5. **J. L. Shaw**, F. S. Tsung, N. Vafaei-Najafabadi, K. A. Marsh, N. Lemos, W. B. Mori, and C. Joshi, "Role of direct laser acceleration in energy gained by electrons in a laser wakefield accelerator with ionization injection," Plasma Phys. Contr. F. **56**, 084006 (2014). *Featured on cover.*
6. F. Albert, B. B. Pollock, **J. L. Shaw**, K. A. Marsh, J. E. Ralph, Y-H. Chen, D. Alessi, A. Pak, C. E. Clayton, S. H. Glenzer, and C. Joshi, "Measuring the angular dependence of betatron x-ray spectra in a laser-wakefield accelerator," Plasma Phys. Contr. F. **56**, 084016 (2014).
7. F. Albert, B. B. Pollock, **J. L. Shaw**, K. A. Marsh, J. E. Ralph, Y.-H. Chen, D. Alessi, A. Pak, C. E. Clayton, S. H. Glenzer and C. Joshi, "Angular dependence of betatron x-ray spectra from a laser-wakefield accelerator," Phys. Rev. Lett. **111**, 235004 (2013).
8. B. B. Pollock, J. Meinecke, S. Kuschel, J. S. Ross, **J. L. Shaw**, C. Stoafer, L. Divol, G. R. Tynan, and S. H. Glenzer, "Simultaneous imaging electron- and ion-feature Thomson scattering measurements of radiatively heated Xe," Rev. Sci. Instrum. **83**, 10E348 (2012).
9. B. B. Pollock, C. E. Clayton, J. E. Ralph, F. Albert, A. Davidson, L. Divol, C. Filip, S. H. Glenzer, K. Herpoldt, W. Lu, K. A. Marsh, J. Meinecke, W. B. Mori, A. Pak, T. C. Rensink, J. S. Ross, **J. Shaw**, G. R. Tynan, C. Joshi, and D. H. Froula, "Demonstration of a Narrow Energy Spread, ~0.5 GeV Electron Beam from a Two-Stage Laser Wakefield Accelerator," Phys. Rev. Lett. **107**, 045001 (2011).

Ch. 1: Introduction

High-energy radiofrequency (RF) particle accelerators have been at the forefront of fundamental scientific discovery since their inception and have contributed significantly to the understanding of topics such the origin of the universe and how the fundamental particles and forces of the universe interact. Particles gain energy in these conventional particle accelerators by accelerating gradients that are generated when large RF fields are applied to the disk-loaded copper cavities that make up the accelerator. As science has advanced, higher and higher particle energies have been required to probe the frontier of scientific discovery. However, because the operating accelerating gradient in conventional RF accelerators is limited to ~ 20-40 MV/m [1] by the breakdown of the copper cavities, higher particle energies have required larger and larger machines that become prohibitively more expensive. This situation is especially challenging for accelerating light particles (i.e. electrons and positrons) because they require linear accelerators; the light particles would lose excessive energy to synchrotron radiation if they were accelerated in a circular configuration such as the Large Hadron Collider [2].

In 1979, Tajima and Dawson proposed plasma-based particle acceleration [3], which would not be limited by material breakdown and consequently could support significantly-higher acceleration gradients. Their proposed mechanism involved injecting a laser pulse into an underdense plasma and using the pondermotive force of that pulse to generate an electrostatic plasma wave (a wake) behind the laser. Electrons could become trapped in the wake and accelerated by its longitudinal field. This process came to be known as laser wakefield acceleration (LWFA). By their initial estimates, such a system could support longitudinal accelerating fields eE_z on the order of $eE_z \simeq mc\omega_p$ [3], which is > 10 GeV/m for plasma densities ~ $1 \times 10^{18} - 1 \times 10^{19}$

cm^{-3}. Here, $\omega_p = \sqrt{\frac{e^2 n_e}{m_e \epsilon_0}}$ is the plasma frequency, and n_e is the plasma electron density. These gradients are ~ 3 orders of magnitude higher than the average accelerating gradient of 10.2 MV/m at today's highest-energy linear RF accelerator at SLAC National Accelerator Laboratory, which can produce 20.35 GeV electron beams in 2 km.

When Tajima and Dawson first proposed the concept of plasma-based particle acceleration, they also noted that two laser pulses with slightly-different wavelengths could be made to beat together to form a beat packet that is approximately the length of the plasma wavelength and therefore could excite a plasma wave [3]. This method of the plasma beatwave acceleration (PBWA) [3-6] was first demonstrated at UCLA using a CO_2 laser running at wavelengths of 10.59 μm and 10.29 μm, where externally-injected electrons were accelerated from energies of 2.1 MeV to 9.1 MeV [7]. Shortly thereafter, the first evidence of the trapping and acceleration of externally-injected electrons out to energies ~ 30 MeV was shown [8].

Shortly after Tajima and Dawson's paper on LWFA [3], it was realized that relativistic electron beams from conventional RF accelerators could also be used as a driver for plasma-based particle acceleration [9]. This concept, which is known as plasma wakefield acceleration (PWFA), relies on the Coulomb force of the electron beam to drive a wakefield. The first experimental work on PWFA verified that an electron beam could indeed drive a wake and used a second, witness electron beam to map out the field structure of that wake [10]. PWFA was shown to be capable of producing large energy gains by Blumenfeld et al. [11], where they demonstrated more than 43 ± 7 GeV of energy gain for electrons in the tail of a 42 GeV electron beam driver. Since that time, PWFA has continued to make steady progress. In 2014, PWFA demonstrated the acceleration of a discreet, separately-injected electron beam, which gained ~1.6 GeV from the wakefield driven

by a 20.35 GeV drive electron beam with an energy-extraction efficiency that exceeded 30% [12]. Most recently, PWFA has been demonstrated using a positron beam to drive the wakefield [13], which is a critical step towards realizing a plasma-based electron-positron collider [14]. In that experiment, the tail electrons of the positron driver gained over 5 GeV in 1.3 meters of plasma with ~ 30% efficiency, and the accelerated positrons had an energy spread as low as 1.8% [13].

While PWFA has continued to rapidly advance over the years, initial advancements in laser technology ushered in significant advances in LWFA, and subsequent advancements in laser technology have provided access to new regimes of LWFA. These regimes can be distinguished by the ratio of the laser pulse length relative to the nonlinear plasma wavelength Λ_{wake}. This ratio can be represented by the dimensionless pulse length parameter [15]

$$T_p = c\tau_{laser}/\Lambda_{wake} = \omega_p\tau_{laser}/(2\pi a_0^{1/2}) \quad (1.1)$$

If the laser pulse length $c\tau_{laser}$ is equal to the a_0-dependent length of the first bucket [16]

$$\Lambda_{wake} \simeq \sqrt{a_0}\,\frac{2\pi}{k_p} \quad (1.2)$$

then $T_p = 1$. Here, $k_p = \omega_p/c$, and a_0 is the normalized vector potential

$$a_0 = eE_0/mc\omega_0 \simeq 8.6 \times 10^{-10}\sqrt{I_0[W/cm^2]}\lambda[\mu m] \quad (1.3)$$

where I_0 is the laser intensity and λ is the wavelength of the laser.

With the advent of the chirped pulse amplification (CPA) technique in 1985 [17], lasers with pulse lengths ~ 1 ps and energies ~ 1 J – 1 kJ became available. Such laser drivers can be used to drive a LWFA in the so-called self-modulated LWFA (SMLWFA) [18] and/or the Raman forward scattering (RFS) regime [19, 20]. In this regime, the laser pulse is much longer than the plasma wavelength (T_p ~ 2 or longer). When such a laser enters the plasma, the front of the laser pulse undergoes strong stimulated Raman backscatter [21] while the main body of the pulse

undergoes a Raman forward scattering [19, 20] and/or self-modulation [18, 22-24] instability. These modulations lead to a train of laser micropulses coherently driving plasma waves that trap and accelerate electrons. Though SMLWFA was demonstrated by Joshi et al. in 1981, where electrons with energies up to 1.4 MeV were observed in the forward direction [19], the laser intensity in this experiment was rather modest ($a_0 \sim 0.3$). Within 15 years of this first experiment, intensity increases enabled by CPA led to the first observation of a plasma wave produced by the self-modulation of a ~0.7 ps-long laser pulse being driven to wave-breaking and producing electrons with maximum energies up to 44 MeV [20]. As laser technology advanced and laser pulses became shorter than 50 fs, LWFA research moved away from the SMLWFA regime, but recently, there has been renewed interest [25, 26] in this latter regime due to the availability of ps-scale lasers coupled with large high-energy-density science (HEDS) laser drivers such as the OMEGA laser at the University of Rochester and the National Ignition Facility at Lawrence Livermore National Laboratory.

The next advance in laser performance came with the introduction of large-bandwidth lasers around 1990. The most common of these is the Ti:Sapphire laser, which was initially capable of pulse lengths ~50-100 fs with powers P of 10s of TW. With early Ti:Sapphire systems, the length of the laser pulse was on the order of the plasma wavelength ($T_p \sim 1$), and the laser intensity was capable of producing a partial blowout of the plasma electrons. With such a laser, the LWFA is said to be in the forced wakefield regime [27]. In this regime, the laser pulse excites a plasma wave, which in turn shortens the frequency-modulated laser pulse through group velocity dispersion. The laser pulse forms an "optical shock" with a steep front edge, which can then drive an even stronger wake. This regime was first demonstrated in 2002 by Malka et al. [27]. In these experiments, the forced LWFA produced collimated electron beams with a continuous energy

spread and a maximum energy exceeding 200 MeV. The divergence of those electrons with energies exceeding 35 MeV was $5^0 \pm 1^0$, and the normalized vertical emittance was $2.7 \pm 0.9\ \pi$ mm-mrad for electrons with energies exceeding 55 MeV [27]. These electron beam parameters were evidence that LWFA may be able to provide electron beams with emittances and divergences on the order of those from conventional RF particle accelerators.

Shortly after this work, three ground-breaking LWFA papers were published that showed it was possible to generate relativistic (~ 50-200 MeV) LWFA electron beams with sizeable charge (~ 10^8 - 10^9 electrons), low divergence (< 6^0), and small energy spread (< 3% [28, 29] and ~ 24% [30]). Following this work, a serious effort [16, 31] was undertaken at UCLA to understand how LWFA could be optimized to produce electron beams with charges, emittances, energies, and energy spreads competitive with conventional RF accelerator technologies. Through this study [16], it was determined that the ideal LWFA performance (i.e. high electron energies with low emittance, divergence, and energy spread) occurs when the LWFA is operating in the matched blowout regime. In this regime, the radiation pressure of an intense laser pulse pushes a majority of the plasma electrons out and around the main body of the pulse. The expelled plasma electrons feel the electrostatic field of the relatively-stationary ions and are thus attracted back towards the laser axis behind the laser pulse. They overshoot the axis and set up a wake oscillation, which can trap electrons at the rear of the wake where those electrons are accelerated by the longitudinal wakefield.

For a LWFA to be in the blowout regime, the laser pulse must be intense ($a_0 > 4$), short $\left(c\tau_{laser} < \frac{2\sqrt{a_0}c}{\omega_p} \text{ or } T_p < 0.2\right)$, and matched to the plasma density (laser spot size w_0 ~ the blowout radius R_b) to completely expel all the plasma electrons [16]. Simulations also show that

even if $2 \leq a_0 \leq 4$, the LWFA can still operate close to the blowout regime (i.e. the quasi-blowout regime) if the other conditions hold [16]. Additionally, this study [16] developed a series of phenomenological scaling laws for the performance of LWFAs operating in the blowout regime. Since this publication, many, if not most, LWFA experiments have compared their results to these scaling laws even if the laser and plasma parameters are not rigorously in the blowout regime. However, as short-pulse laser technology has continuously improved, there are now lasers with pulse lengths and intensities capable of producing LWFA in the blowout regime.

One of the initial concerns surrounding LWFA driven with short-pulse lasers was the question of whether the laser would defocus after a Rayleigh length and therefore no longer be able to drive a wake, which would limit the acceleration distance [28]. Simulation studies [16, 31] showed that it was possible for short-pulse lasers to be self-guided by the plasma, and experimental verification of this concept was completed by Ralph et al. in 2009 [32, 33], where they showed that a short-pulse laser could self-guide and continue to drive a wake in a plasma for tens of Rayleigh lengths.

As in a conventional RF accelerator, the energy gain in a LWFA is limited by both the accelerating gradient and the length of acceleration. In the blowout regime of LWFA, the average useful accelerating gradient ϵ_{LW} is given by [16]

$$\epsilon_{LW} \equiv \frac{eE_{z,max}}{2mc\omega_p} \simeq \frac{\sqrt{a_0}}{2} \tag{1.4}$$

The length of acceleration is limited by dephasing, which is when the trapped electrons overtake the accelerating field of the wake because their velocity is ~ c while the group velocity of the laser is less than the speed of light. The dephasing length L_d is given by [16]

$$k_p L_d = \frac{4}{3}\frac{n_c}{n_e}\sqrt{a_0} \tag{1.5}$$

Here, n_c is the critical density (i.e. when the laser frequency $\omega_0 = \omega_p$). Taking the two together, the maximum energy gain expected in a LWFA operating in the blowout regime is [16]

$$E_{theory} \simeq \frac{2}{3} mc^2 \frac{n_c}{n_e} a_0 \simeq mc^2 \left(\frac{P}{m^2c^5/e^2}\right)^{1/3} \left(\frac{n_c}{n_e}\right)^{2/3} \tag{1.6}$$

This equation can be written in engineering form [16]

$$\Delta\, E[\mathrm{GeV}] \simeq 1.7 \left(\frac{P[\mathrm{TW}]}{100}\right)^{1/3} \left(\frac{10^{18}}{n_e[\mathrm{cm}^{-3}]}\right)^{2/3} \left(\frac{0.8}{\lambda[\mu\mathrm{m}]}\right)^{4/3} \tag{1.7}$$

This maximum energy gain scales as $1/n_e$, and consequently there has been a large effort in the community to push LWFA experiments to lower and lower plasma densities to increase the energy of the self-generated electron beams.

As the plasma density is reduced, it becomes increasingly difficult to trap charge in the wake. For an electron to be trapped, it must gain enough energy from the wakefield so that its velocity is larger than the phase velocity of the wake. In its initial conception [3], LWFA relied upon "self-trapping," which is where background plasma electrons become trapped in the back of a wake driven by the drive laser pulse. Self-trapping occurs when the wake amplitude reaches a certain threshold value, and it is therefore more efficient at higher plasma densities ($> 10^{19}$ cm^{-3}) or larger laser intensities ($a_0 > 4$). Because this process is nonlinear and frequently relies on the evolution of the wake structure and/or the laser pulse [34], it can be difficult to predict and control. This lack of stability coupled with the trend towards lower plasma densities (for gaining higher electron energies) has led to research on finding different ways in which electrons can be injected into a wake.

In the "colliding pulse" injection scheme, a second laser is used to control the injection of charge into a LWFA. In the simplest configuration, this scheme relies on the collision of two counter-propagating laser pulses to pre-accelerate plasma electrons to sufficient energy so that they can be trapped by the wakefield [35]. A main laser pulse is used to drive the wake, and a second, lower-intensity pulse, which has the same central wavelength and polarization, causes injection. The two counter-propagating laser pulses are overlapped in the plasma where they interfere with each other and form a beat pattern that is approximately stationary ($v_{beatpattern} \sim 0$) and has a small spatial scale. This small scale leads to a large pondermotive force from the beatwave, which can pre-accelerate the background plasma electrons so that they can be trapped in the wakefield. The concept of using a second, orthogonal laser pulse to inject charge was originated by Umstadter et al. [36] in 1996, but it required high intensities in both the main and injection laser pulses. A configuration with two counter-propagating injection pulses, where the intensity of each was $a_0 \sim 0.2$, was proposed by Esarey et al. [37] in 1997. Further analytical [38] and simulation [38, 39] work showed that colliding pulse injection could lead to high-quality, narrow-energy-spread, and low-divergence electron beams. Faure et al. demonstrated that this mechanism worked in a two-beam counter-propagating configuration with a drive laser (a_0 as low as ~1) and an injection laser (a_0 as low as ~0.3) [35, 40].

Though the results with colliding pulse injection were successful, it is a technically challenging route to inject charge in a LWFA. Tailoring the plasma density profile was proposed [41, 42] as a simpler route to inject charge in a LWFA. As seen in Equation 1.2, the a_0-dependent wake wavelength scales as $1/\sqrt{n_e}$. Therefore, if the drive laser propagates through a plasma density profile that suddenly transitions from a higher density to a lower density, the wake wavelength lengthens, which effectively reduces the phase velocity of the wake. Consequently,

the velocity required for the electrons to be trapped is reduced, and they are more easily trapped. This method of tailoring a plasma density gradient to control trapping is commonly known as "downramp injection." The downramp injection of charge was experimentally demonstrated in the SMLWFA regime in 2005 by Chien et al., who used a second laser pulse propagating transversely to the drive laser pulse to heat the plasma and create a local density upramp and downramp in which charge was trapped [43]. In 2008, Geddes et al. conducted experiments in the forced LWFA regime where they controlled the plasma density profile by varying the focal location of the drive laser pulse [44]. They were able to generate stable electron beams with reduced momentum spread in both the longitudinal and transverse directions [44]. Downramp injection has become a workhorse in the LWFA field, and tailored density profiles are now created in a variety of ways such as modifying the gas flow in a supersonic gas jet with a knife edge to produce a shock front [45].

In the ionization injection technique, the plasma is produced by the laser ionization of a neutral gas mixture comprised of a gas with a low ionization potential (commonly He or H_2) doped with a gas with high ionization potential (commonly N_2 or Ar). The lower-intensity front edge of the laser pulse ionizes the outer (typically L) shell electrons of the dopant gas along with all the electrons in the gas with a low ionization potential. Because the inner (typically K) shell electrons of the higher-z atoms have a much higher ionization potential, they are only ionized close to the peak of the laser pulse within a fully-formed wake and are subsequently trapped without slipping all the way to the back of the wake [46, 47]. Compared to self-trapping, this method of ionization injection permits trapping in a LWFA at reduced plasma densities and laser powers. The only drawback is that the injection is not localized, which can lead to energy spread in the produced electron beams [46, 48]. Ionization injection was first shown in PWFA by Oz et al. in 2007 [49].

Ionization injection in LWFA was claimed by Rowlands-Rees et al. in 2008 [50] and then conclusively demonstrated by Pak et al. [46] and McGuffey et al. [47] in 2010.

Despite these advanced injection methods allowing LWFA to operate at lower plasma densities, dephasing is still a fundamental limitation on the amount of energy that can be gained in a single stage of LWFA. To make LWFA competitive as an alternative to conventional RF linear accelerators, multiple LWFAs will need to be staged [14].

A first path towards staging multiple LWFAs was two-stage LWFA [51, 52], which can provide high-energy, low-energy-spread electron beams using ionization injection. In this scheme, a LWFA is driven in a divided gas cell or in two adjacent gas cells (Figure 1. 1). The first stage is an injector, which traps a large amount of charge and accelerates it to between 50 MeV and 100 MeV with a relatively large energy spread. This injector stage uses ionization injection and is therefore filled with He and a trace amount of a higher-Z gas (typically N_2). Ideally, this first stage is kept short to control both the total amount of injected charge and its maximum energy (and therefore ultimately the energy spread). The injection stage is followed by an acceleration stage that accelerates the trapped charge to high energies while maintaining its energy spread. In this way, the energy spread is actually reduced. This second gas cell is filled with pure He at low density so that it is unlikely that any He electrons will become self-trapped. Therefore, the electron injection is effectively shut off as the laser, wake, and trapped electrons pass into this stage. Only the electrons from the injector will be accelerated, and it may be possible to increase their energy without further increasing their energy spread since electron injection is turned off in the accelerator section. Thus, for any given laser, two-stage LWFA can produce electron beams with a large amount of charge and with high energies but with low energy spread. Two-stage LWFA was demonstrated by several groups [53, 54], including by Pollock et al. in 2011 [52]. Using this

configuration, an ~0.5 GeV quasi-monoenergetic electron beam with less than a 5% full-width, half-maximum (FWHM) energy spread was observed [52].

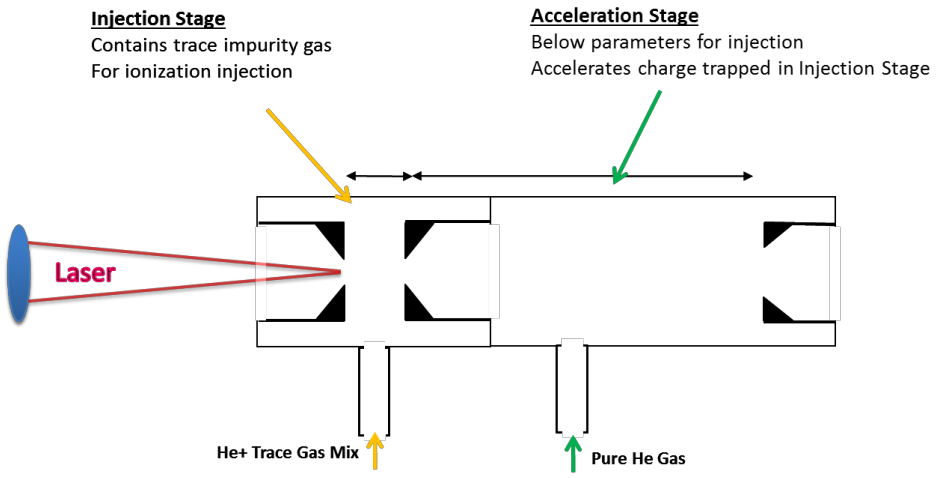

Figure 1. 1:Concept of two-stage LWFA.

Since the initial two-stage LWFA experiments [52-54], there has been considerable effort in the LWFA community to improve staged LWFA [14]. Recently, the first staging of LWFA where each stage was powered by an independent laser pulse was demonstrated by Steinke et al [55]. Here, a first LWFA stage was driven by a 1.3 J, 45 fs, 800 nm laser beam and produced an electron beam with a central energy of 120 MeV. The electron beam produced in the first stage was refocused using a discharge capillary, which served as an active plasma lens [56], into a second LWFA stage. This second LWFA stage was driven by a 450 mJ, 45 fs, 800 nm laser beam, which was coupled into the system using a plasma mirror that was created when that laser pulse struck a VHS tape and created a critical-density plasma [57]. The second LWFA stage boosted the energy of a portion of that electron beam by 100 MeV. Although the charge-coupling efficiency was only

3.5% [55], this experimental demonstrated that it is possible to couple an electron beam from one LWFA stage into the next, which is an important step towards a LWFA-based linear collider [14].

LWFA shows promise as more than just a source of electrons. It is well known that if electrons are injected off-axis in a LWFA or a PWFA, they undergo betatron oscillations because of the focusing field of the ions and therefore emit x-rays, which are known as betatron x-rays [58, 59]. Betatron x-rays were first measured in PWFA experiments in 2002, where the electrons in a 28.5 GeV drive beam executed betatron oscillations under the influence of the ion channel and emitted broadband x-rays [58]. Limited work on betatron x-ray production was initially done in the SMLWFA regime [60], but betatron radiation has mostly been studied in the forced and blowout LWFA regimes. These LWFA regimes are of interest because they produce the most energetic electron beams, and since both the critical energy of the emitted betatron x-ray spectrum and its radiated power scale as γ^2 and its divergence scales as $1/\gamma$ [61], where γ is the Lorentz factor of the electrons, this regime produces highly-directional and bright x-ray beams. Early betatron radiation experiments in the forced LWFA regime measured x-rays up to 6 keV in a beam with a divergence as low as 20 mrad FWHM [59]. The first simultaneous spatial and spectral measurements were carried out in 2013 by Albert et al. [62]. Developing betatron x-ray sources is an ongoing field of research and is finding wide applications including medical [63], biological [64], and HEDS [25, 26] applications.

The first experimental efforts to demonstrate plasma-based particle acceleration using CPA laser systems were accompanied by a significant theory and simulation effort to understand how particles could be accelerated by such laser-plasma systems. This work extended beyond plasma wakefields and included various methods of stochastic heating [65-68] and of acceleration of the particles directly from the laser [69-77]. One such mechanism, which came to be called “direct

laser acceleration" (DLA), proposed to accelerate electrons in the longitudinal direction using the transverse field of a laser through a resonance with the betatron motion of the electrons in an ion column, which gives the electrons a velocity component in the direction of the laser polarization. This transverse momentum can then be converted to longitudinal momentum via the **v** x **B** force [78-80]. The one-dimensional resonance condition for DLA of a single electron is commonly given by [78, 79]

$$N\omega_\beta = \left(1 - {}^{v_\parallel}/_{v_\phi}\right)\omega_0 \tag{1.8}$$

where N is an integer indicating the harmonic of the betatron frequency,

$$\omega_\beta = \frac{\omega_p}{\sqrt{2\gamma}} \tag{1.9}$$

is the betatron frequency, $v_\parallel$ is the velocity of the electron in the longitudinal direction, and v_ϕ is the phase velocity of the electromagnetic wave (i.e. laser).

It was quickly recognized that CPA laser systems running with a_0 values > 1 were capable of generating ion channels through electron cavitation [81]. Electrons can be pre-accelerated either by the longitudinal field of a plasma wave excited by the laser before all the plasma electrons are expelled or by the fields of a surface wave surrounding the ion cavity. These electrons can oscillate under the combined influence of the laser field and the ion field and gain energy through DLA.

The first experiment reporting the DLA of electrons was conducted by Gahn et al. in 1999 [82]. In this experiment, they used an F/3 off-axis parabola to focus a relatively-long-pulse (200 fs), low-energy (< 1 J) laser onto a high-density He gas jet (n_e up to 4 x 10^{20} cm^{-3}). Accelerated electrons with energies up to 12 MeV were observed and attributed to the DLA mechanism using three-dimensional (3D) particle-in-cell (PIC) simulations. These simulations showed that the laser

self-focused in this high plasma density, and the resulting high a_0 (estimated to be at least 3) generated an ion channel. No electrons appeared for plasma densities less than 3 x 10^{19} cm^{-3}, which was the threshold for the self-focusing of the laser. 3D simulations indicated that though a wakefield was present, it primarily served to decelerate the electrons; DLA was the dominant acceleration mechanism [82].

In 2005, Mangles et al. conducted an experiment using the Vulcan laser with a much longer 650 fs laser pulse where a_0 values $\simeq$ 15 were used to generate an ion channel in a plasma [83]. In this experiment, maximum electron energies ~ 300 MeV were observed. The relative intensity of the side bands of the transmitted laser spectrum was measured. These side bands at the Stokes and anti-Stokes frequencies indicate that the Raman forward-scattering instability is driving a relativistic wave in the plasma [84, 85]. In prior experiments performed on the Vulcan laser where a_0 ~ 1-2 [20, 86], the temperature of the electrons beams produced from a SMLWFA was found to increase with the strength of the laser-driven plasma waves as measured by the increased modulation of the transmitted laser spectrum. However, in Mangles 2005 experiment [83], the highest electron beam temperatures were measured when the modulation of the transmitted laser spectrum was small (i.e. the laser did not drive a strong relativistic plasma wave). This finding strongly suggests that the wakefield was not the principle acceleration mechanism but rather that the highest-energy electrons were accelerated by DLA [83].

In 2008, Kneip et al. [60] conducted an experiment where they measured the betatron radiation from the electrons trapped in an ion channel formed by a laser with a_0 values between 9 and 29. Based on the measured electron and x-ray spectra, the betatron oscillation amplitude required to produce the x-rays was consistent with the electrons being accelerated by DLA [60]. Based on this initial work, Kneip et al. then published a thorough comparison of betatron radiation

from systems were the electrons were accelerated by LWFA or DLA [87]. In this study, they found that LWFA was capable of producing narrow-divergence, quasi-monoenergetic electron spectra out to 400 MeV, whereas DLA produced Maxwellian beams whose maximum energy did not surpass 200 MeV. They found through measurements of the x-ray spectra, divergence, and source size that the brightness of the LWFA source was four times larger than the DLA source, but that the betatron oscillation amplitude of the DLA source was ~ 15 times that of the LWFA source and that the DLA source had a higher cutoff energy.

In 2010, Nilson et al. [88] directly measured of the formation of an ion channel in a laser-driven plasma, which is requisite for DLA. They also found that multiple channel formation was possible in such laser-plasma systems, and these multiple channels could lead to multiple electron beams with energies > 100 MeV.

Each of these prior experiments showing the DLA of electrons was conducted in a regime where the laser intensity, the pulse length, and/or the plasma density were such that no wakefield acceleration of the electrons was expected. However, for the range of plasma densities (mid-10^{18} to a few 10^{19} cm^{-3}) and laser pulse durations (35-45 fs FWHM) that are typically used in many current LWFA experiments in the forced or quasi-blowout regime, the laser pulse may occupy the entire first bucket of the wake. The wakefield structure has a desirable transverse and longitudinal field structure for generating a high-quality electron bunch, but it also has all the conditions needed for DLA if there is an overlap between the trapped electrons and the transverse electric field of the laser pulse. It is therefore important to understand the role of not only the wakefield, but also DLA plays in determining the ultimate energy gained by the electrons.

In a LWFA operating in the forced or quasi-blowout regime, the ion column acts as a very strong wiggler. Trapped electrons that are being accelerated by the wake undergo betatron oscillations in response to the transverse electric field of the ion column. Therefore, if a LWFA is configured such that some of the trapped electrons undergo betatron oscillations in the plane of polarization of the laser's electric field soon after they are trapped, those electrons directly exchange energy with the laser field through DLA.

It has been noted that DLA is the inverse of the ion channel laser mechanism [89]. DLA in LWFA is also similar to inverse free electron laser (IFEL) acceleration [90, 91], except that the static magnetic undulator used in an IFEL is replaced by the transverse electric field of the ions in DLA. The resonance condition for DLA is similar to that for an IFEL [92]; i.e. in an ideal situation, the laser pulse overtakes the electrons by one wavelength per betatron oscillation once the electrons come into resonance with the fundamental (N=1) harmonic, where the electrons are bunched on a laser-wavelength scale [78, 93-96]. However, unlike in an IFEL, sustained resonance for DLA is more difficult to design because in the latter case, the normalized undulator strength $K >> 1$ and the energy and betatron frequency of the electrons as well as the laser properties are continuously and rapidly changing [15, 97].

Until recently, there has been very little work exploring the presence of DLA in systems where LWFA is thought to be the dominant acceleration mechanism. In some early simulation work on LWFA, Tzeng et al. recognized that for a_0 values ≥ 2, there should be some effect on the acceleration of the electrons if they overlap the drive laser [98]. An effort at UCLA to experimentally verify the phenomenological scaling laws for LWFA in the blowout regime [16] led to a renewed interest in both experiment and simulation to examine DLA in LWFA, but specifically in the forced and quasi-blowout LWFA regimes.

In 2013, we used two-dimensional (2D) PIC simulations with the code OSIRIS [99] to investigate the relative importance of LWFA and DLA in LWFAs operating with laser and plasma parameters typical in many current LWFA experiments [100]. Through these simulations, we showed that DLA was present as an additional acceleration mechanism and that its presence led to the accelerated electron beams having higher maximum energies than is expected from wake acceleration alone. For a constant plasma density, the laser pulse length was varied to demonstrate that the laser pulse must overlap the trapped electrons for DLA to be present. For a constant laser pulse duration, the plasma density was varied such that at lowest densities the laser pulse occupies only a fraction of the accelerating bucket, whereas at the highest density the same duration laser pulse fills the entire first bucket. It was shown that the DLA contribution to the total energy gain increases with the plasma density because at higher densities, the decreased wake wavelength will cause the trapped electrons to overlap with the more intense regions of the laser, leading to higher DLA contributions. This initial detailed study was followed by a second simulation study showing that electrons in a LWFA can gain energy from the DLA mechanism over extended distances, despite the fact that the physical quantities in the DLA resonance condition (Equation 1.8) all evolve over the entire acceleration distance, provided that the resonance condition is satisfied for more than one half of a betatron oscillation [97].

These papers on DLA in LWFA sparked renewed interest in the LWFA community, and in 2015, Zhang et al. published simulations of a scheme to induce DLA in LWFA using one laser pulse to drive the wake and a second to overlap the charge trapped at the back of that pulse [101], and in 2016, they showed through simulations that this method will also work with ionization injection [102]. There was some question from the LWFA community as to whether the DLA of electrons in LWFA seen in these four publications was due to numerical heating. In response, we

showed that the DLA of electrons in LWFA simulations was not an artifact of numerical heating but rather that DLA persists with improved resolution [103]. Most recently, we demonstrated through experiments that DLA is indeed an additional acceleration mechanism in LWFA when $T_p \sim 1$ and that a signature of its presence can be discerned through characteristic spectral features [15]. The renewed interest in DLA in LWFA is also leading to a re-examination of the presence of the two mechanisms in SMLWFA due to its implications in betatron x-ray production. Lemos et al. showed that in the SMLWFA regime with moderate a_0 values, electrons at the front of the laser pulse are trapped and accelerated via the longitudinal electric field of the plasma wave, but at the rear of the pulse, there is no wake and electrons are accelerated by DLA [26].

This dissertation explores through simulations and experiments the presence of DLA in LWFA. Simulations are utilized to demonstrate that electrons can gain significant energy from DLA for extended acceleration distances as long as they gain energy from DLA for more than one half of each betatron cycle. Simulations results comparing LWFA with and without DLA are presented, and the changes in the properties of the electron beam due to the presence of DLA are explored. The effect of the resolution on the presence of DLA in PIC simulations is then addressed. The characterization of the gas cells developed for LWFA experiments at UCLA is presented followed by the experimental results exploring DLA in LWFA. These results show definite evidence of the presence of DLA in LWFA. Finally, this dissertation concludes with suggestions for future work with DLA in LWFA.

Ch. 1 References

[1] D. H. Whittum, Introduction to Electrodynamics for Microwave Linear Accelerators SLAC-PUB-7802 (1998).

[2] L. Evens and P. Byrant, Journal of Instrumentation, 3:SO8001 (2008).

[3] T. Tajima and J. Dawson, Phys. Rev. Lett. **43**, 267 (1979).

[4] C. Joshi et al., Nature **311**, 525-529 (1984).

[5] B. I. Cohen et al., Phys. Rev. Lett. **29**, 581 (1972).

[6] C. M. Tang and P. Sprangle, Appl. Phys. Lett. **45**, 375 (1984).

[7] C. E. Clayton et al., Phys. Rev. Lett. **70**, 37 (1993).

[8] M. Everett et al., Nature **368**, 527-529 (1994).

[9] P. Chen et al., Phys. Rev. Lett. **54**, 693-696 (1985).

[10] J. B. Rosenzweig et al., Phys. Rev. Lett. **61**, 98-101 (1998).

[11] I. Blumenfeld et al., Nature **445**, 741 (2007).

[12] M. Litos et al., Nature **515**, 92-95 (2014).

[13] S. Corde et al., Nature **524**, 442 (2015).

[14] W. Leemans and E. Esarey, Phys. Today **62**, 44 (2009).

[15] J. L. Shaw et al., *Submitted to Phys. Rev. Lett.*

[16] W. Lu et al., Phys Rev. Spec. Top. – Accel. Beams **10**, 061301 (2007).

[17] D. Strickland and G. Mourou, Opt. Commun. **56**, 219-221 (1985).

[18] E. Esarey et al., Phys. Rev. Lett. **72**, 2887 (1994).

[19] C. Joshi et al., Phys. Rev. Lett. **47**, 1285 (1981).

[20] A. Modena et al, Nature **377**, 606-608 (1995).

[21] C. B. Darrow et al., Phys. Rev. Lett. **69**, 85-88 (1992).

[22] N. E. Andreev et al., Pisma Zh. Eksp. Teor. Fiz. **55**, 551 (1992).

[23] T. M. Antonsen and P. Mora, Phys. Rev. Lett. **69**, 2204 (1992).

[24] P. Sprangle et al., Phys. Rev. Lett. **69**, 2200 (1992).

[25] F. Albert et al. OSA Technical Digest FTh4A.l (2015).

[26] N. Lemos et al., Plasma Phys. Contr. F. **58**, 034018 (2016).

[27] V. Malka et al., Science **298**, 1596 (2002).

[28] C. G. R. Geddes et al., Nature **431**, 538-451 (2004).

[29] S. P. D. Mangles et al., Nature **431**, 535-538 (2004).

[30] J. Faure et al., Nature **431**, 541-544 (2004).

[31] W. Lu et al., Phys. Rev. Lett. **96**, 165002 (2006).

[32] J. E. Ralph et al., Phys. Rev. Lett. **102**, 175003 (2009).

[33] J. E. Ralph et al., Phys. Plasmas **17**, 056709 (2010).

[34] S. Kalmykov et al., Phys. Rev. Lett. **103**, 135004 (2009).

[35] J. Faure et al., Nature **444**, 737 (2006).

[36] D. Umstadter et al., Phys. Rev. Lett. **76**, 2073 (1996).

[37] E. Esarey et al., Phys. Rev. Lett., **79**, 2682 (1997).

[38] G. Fubiani et al., Phys. Rev. E **70**, 016402 (2004).

[39] H. Kotaki et al., Phys. Plasmas **6**, 3296-3302 (2004).

[40] J. Faure et al, Comptes Rendus Physique **10**, 148-158 (2009).

[41] S. Bulanov et al., Phys. Rev. E **58**, R5257-R5260 (1998).

[42] H. Suk et al., Phys. Rev. Lett. **86**, 101-1014 (2001).

[43] T. -Y. Chien et al., Phys. Rev. Lett. **94**, 115003 (2005).

[44] C. G. R. Geddes et al., Phys. Rev. Lett., **100**, 215004 (2008).

[45] K. Schmid et al., Phys Rev. Spec. Top. – Accel. Beams **13**, 091301 (2010).

[46] A. Pak et al., Phys. Rev. Lett. **104**, 025003 (2010).

[47] C. McGuffey et al., Phys. Rev. Lett. **104**, 025004 (2010).

[48] C. E. Clayton et al., Phys. Rev. Lett. **105**, 105003 (2010).

[49] E. Oz et al., Phys. Rev. Lett. **98**, 084801 (2007).

[50] T. P. Rowlands-Rees et al. Phys. Rev. Lett. **100**, 105005 (2008).

[51] R. G. Hemker et al. Phys Rev. Spec. Top. – Accel. Beams **5**, 041301 (2002).

[52] B. B. Pollock et al., Phys. Rev. Lett. **107**, 045001 (2011).

[53] J. S. Liu et al., Phys. Rev. Lett. **107**, 03001 (2011).

[54] A. J. Gonsalves et al., Nature Physics **7**, 862-866 (2011).

[55] S. Steinke et al., Nature **530**, 190 (2016).

[56] J. van Tilborg et al., Phys. Rev. Lett. **115**, 184802 (2015).

[57] T. Sokollik et al. AIP Conf. Proc. **1299**, 233 (2010).

[58] S. Wang et al., Phys. Rev. Lett. **88**, 135004 (2002).

[59] A. Rousse et al., Phys. Rev. Lett. **93**, 135005 (2004).

[60] S. Kneip et al. Phys. Rev. Lett. **100**, 105006 (2008).

[61] I. Kostyukov et al., Phys. Plasmas **10**, 4818 (2003).

[62] F. Albert et al., Phys. Rev. Lett. **111**, 235004 (2013).

[63] J. M. Cole et al., Scientific Reports **5**, 13244 (2015).

[64] S. Kneip et al., Appl. Phys. Lett. **99**, 093701 (2011).

[65] G. R. Smith and A. N. Kaufman, Phys. Rev. Lett. **34**, 1613 (1975).

[66] C. R. Menyuk et al., Phys. Rev. Lett. **58**, 2071 (1987).

[67] Z. -M. Sheng et al., Phys. Rev. Lett. **88**, 055004 (2002).

[68] J. Meyer-ter-Vehn and Z. M. Sheng, Phys. Plasmas **6**, 641 (1999).

[69] G. Schmidt and T. Wilcox, Phys. Rev. Lett. **31**, 1380 (1973).

[70] C. I. Moore et al., Phys. Rev. Lett. **74**, 2439 (1995).

[71] F. V. Hartmann et al., Phys. Rev. E **51**, 4833 (1995).

[72] B. Rau et al., Phys. Rev. Lett. **78**, 3310 (1997).

[73] E. Esarey et al., Phys. Rev. E **52**, 5443 (1995).

[74] C. J. McKinstrie and E. A. Startsev, Phys. Rev. E **56**, 2130 (1997).

[75] B. Quesnel and P. Mora, Phys. Rev. E **58**, 3719 (1998).

[76] S. Kawata et al., Phys. Rev. Lett. **66**, 2072 (1991).

[77] M.S. Hussein and M. P. Pato, Phys. Rev. Lett. **68**, 1136 (1992).

[78] A. Pukhov et al., Phys. Plasmas **6**, 2847 (1999).

[79] A. Pukhov, Reports on Progress in Physics **66**, 47 (2003).

[80] G. D. Tsakiris et al., Phys. Plasmas **7**, 3017 (2000).

[81] G. Z. Sun et al., Phys. Fluids **30**, 526 (1987).

[82] C. Gahn et al., Phys. Rev. Lett. **83**, 4772 (1999).

[83] S. P. D. Mangles et al., Phys. Rev. Lett. **94**, 245001 (2005).

[84] D. W. Forslund et al. Phys. Fluids **18**, 1002-1016 (1975).

[85] W. B. Mori et al., Phys. Rev. Lett. **72**, 1482-1485 (1994).

[86] Z. Najmudin et al., Phys. Plasmas **10**, 2071 (2003).

[87] S. Kneip et al., *Proceedings of SPIE*, edited by D. A. Jaroszynski and A. Rousse, **7359**, 73590T-73590T-9 (2009).

[88] P. M. Nilson et al., New J. Phys. **12**, 045014 (2010).

[89] D. Whittum et al., Phys. Rev. Lett. **64**, 2511 (1990).

[90] R. B. Palmer, J. Appl. Phys. **43**, 3014 (1972).

[91] E. Courant et al., Phys. Rev. A **32**, 2813 (1985).

[92] P. Musumeci et al., Phys. Rev. Lett. **94**, 154801 (2005).

[93] K. Németh et al., Phys. Rev. Lett. **100**, 095002 (2008).

[94] M. J. H. Luttikhof et al., Phys. Rev. Lett. **105**, 124801 (2010).

[95] I. Nam et al., Phys. Plasmas **18**, 043107 (2011).

[96] S. Y. Tochitsky et al., Phys. Rev. Spec. Top. – Accel. Beams **12**, 050703 (2009).

[97] J. L. Shaw et al., *Proceedings of the 2014 Advanced Accelerator Concepts Workshop. http://arxiv.org/abs/1502.07664v1.*

[98] K. -C. Tzeng et al., Phys. Rev. Lett. **79**, 5258 (1997).

[99] R. A. Fonseca et al., in *Lecture Notes in Computer Science*, Vol. 2331 (Springer Berlin Heidelberg, 2002) pp. 342-351.

[100] J. L. Shaw et al., Plasma Phys. Contr. F. **56**, 084006 (2014).

[101] X. Zhang et al., Phys. Rev. Lett. **114**, 184801 (2015).

[102] X. Zhang et al., Plasma Phys. Contr. F. **58**, 034011 (2016).

[103] J. L. Shaw et al. Plasma Phys. Contr. F. **58**, 034008 (2016).

Ch. 2: Simulations

Introduction

As introduced in the last chapter, when a LWFA is configured such that the drive pulse overlaps the electrons trapped in the wakefield ($T_p \sim 1$ or larger), those electrons can gain energy from both the DLA and the LWFA mechanisms. Unlike in the work presented in this dissertation, where both LWFA and DLA can participate in the acceleration of the electrons, in the initial theoretical work on DLA, Pukhov et al. [1, 2] were developing an understanding of that mechanism alone. Because they were only considering DLA, they were able to study the process with several simplifying assumptions including modeling the process for a single electron only, using a plane electromagnetic wave with non-evolving properties, and assuming a static transverse electric field. In the case of DLA-assisted LWFA considered in our body of work, we are not able to make these simplifying assumptions. DLA occurs in the ion column of the LWFA structure and, in this case of interest, is driven by the same laser that drives the LWFA. The properties of the drive laser evolve in a LWFA due to self-focusing [3], photon acceleration [4], self-steepening [5, 6], and pump depletion [5-8]. This laser evolution can change the properties of the ion column by increasing the percentage of plasma electrons that are expelled from the laser axis [9]. Both the change in the laser properties and the change in the ion column affect DLA. Having a laser pulse that is long enough to overlap the trapped electrons can itself change the structure of the wakefield, most notably by lengthening the period of the wake. Thus, in the LWFA system studied in this work, both DLA and LWFA play a role in the acceleration of the electrons, and these roles are closely intertwined due to the dependence of DLA on LWFA. Therefore, to gain a better

understanding of this unique interplay between DLA and LWFA in a self-consistent model, we extensively utilized PIC simulations using the code OSIRIS [10].

This chapter summarizes the major simulation work completed on the DLA of electrons being accelerated in a LWFA. Section 2.1 reviews the DLA resonance condition and explains how electrons can gain energy from DLA for a long distance in a LWFA without rigorously satisfying the DLA resonance condition [9]. In Section 2.2, we compare the acceleration of electron beams in LWFA with and without DLA [11]. We conclude this chapter in Section 2.3 with a study on how the resolution used in a PIC code affects DLA in simulations of LWFA [12].

Section 2.1: Satisfying the DLA Resonance Condition in a LWFA

The condition for energy gain from the DLA mechanism is typically expressed using the 1D resonance condition for a single electron [1, 2]

$$N\omega_\beta = \left(1 - v_\parallel / v_\phi\right)\omega_0 \tag{1.8}$$

which assumes that the properties of the electron and the electromagnetic wave (i.e. laser in the LWFA case) do not evolve. Essentially, this resonance condition means that in order for an electron to gain energy from DLA, a harmonic of the betatron frequency $N\omega_\beta$ must equal the Doppler-shifted laser frequency $\left(1 - v_\parallel / v_\phi\right)\omega_0$ witnessed by the electron [1, 2, 9]. However, it is well-known that in LWFAs, especially those not in the ideal blowout regime [13], the properties of the drive laser, including ω_0 and v_ϕ [14], evolve throughout the acceleration distance. Furthermore, as electrons are accelerated in a LWFA, their longitudinal momentum, and therefore their $v_\parallel$, increases, and their betatron frequency is expected to fall as $\gamma^{-1/2}$ as seen in Equation 1.9. Given that all the four quantities present in Equation 1.8 are evolving, it would appear unlikely that the DLA resonance condition could be satisfied long enough for electrons in a LWFA to gain net energy from DLA. In this Section, we demonstrate through PIC simulations of LWFA-

produced electrons that it is not necessary for these electrons to continuously satisfy Equation 1.8 to gain sizable energy from DLA over extended distances.

To investigate how electrons in a LWFA can gain energy from DLA over extended distances, we utilized a 2D OSIRIS PIC code simulation of a LWFA where the produced electrons show energy gain from DLA. For the simulation, the laser pulse had an a_0 of 2.1 and a central wavelength of 815 nm. Its pulse length τ_{laser} was 45 fs so that it overlapped the electrons trapped in the first bucket of the wake ($T_p = 0.8$). The laser ionized a neutral gas, which was comprised of 99.9% He and 0.1% N_2 so that the inner-shell N_2 electrons would be trapped via the ionization injection mechanism [15]. The resulting plasma density was 8×10^{18} cm^{-3}, and the plasma density profile consisted of an 1800-μm-long plateau region with 100-μm-long linear entrance and exit ramps. The simulation was completed with a speed-of-light moving window and used a 2494 x 452 grid. The longitudinal and transverse resolutions were $k_0 dx_{\parallel}=0.21$ and $k_p dx_{\perp}=0.12$, respectively.

The simulation was run to completion once to identify the highest-energy electrons produced. Those electrons were tagged, and the simulation was then rerun to determine the position, momentum, and fields sampled by those electrons at each time step in the simulation. With this information, it was possible to calculate the relative contribution $W_{\parallel}$ of the longitudinal electric field $\mathbf{E}_{\parallel}$ to the total energy of the electrons using

$$W_{\parallel} = -e\int_0^t \mathbf{E}_{\parallel}\cdot\mathbf{v}_{\parallel}\,dt' \qquad (2.1)$$

The dominant longitudinal electric field is the wakefield, and therefore this value will be called the "LWFA contribution" to the final electron energy. Similarly, the relative contribution $W_{\perp}$ due to the transverse electric field $\mathbf{E}_{\perp}$ was calculated using

$$W_{\perp} = -e\int_0^t \mathbf{E}_{\perp}\cdot\mathbf{v}_{\perp}dt' \qquad (2.2)$$

where $\mathbf{v}_{\perp}$ is the transverse velocity of the electron. The dominant transverse electric field is the transverse laser field, and so this value will be called the "DLA contribution" to the final electron energy. The highest-energy electrons reached a maximum energy of 290 MeV by the end of the simulation as shown in Figure 2.1. Net energy gain from DLA occurred for 1180 μm and included nearly 4 complete betatron oscillations of the electrons. Using Equations 2.1 and 2.2, it was determined that 197 MeV of the 290 MeV was due to LWFA and 93 MeV was due to DLA. In other words, for this LWFA configuration, the contribution of DLA to the final electron energy is comparable to the wakefield contribution. One of these highest-energy electrons, which gained 38% of its total energy from DLA, was randomly selected, and this test electron will be used in all subsequent calculations in this Section to investigate the DLA resonance condition in such a LWFA.

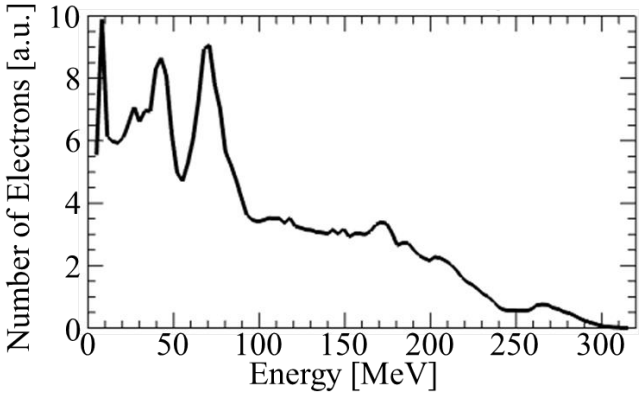

Figure 2. 1: Energy spectrum of the electron beam produced in the simulation.

In order to determine if this test electron satisfies the DLA resonance condition (Equation 1.8) for the regions where it gained energy from DLA, the evolution of its relevant parameters was followed throughout the simulation. The betatron frequency was measured by first plotting the

test electron's trajectory, which shows its betatron oscillations, as a function of distance in the simulation. From this plot, the locations in the simulation where the electron reaches a minimum, reaches a maximum, or crosses a zero (i.e. the laser axis) of its betatron oscillation can be determined. Once the locations are known for each of the minima, maxima, or zeros, the instantaneous half betatron wavelength $\lambda_\beta/2$ at each of these points can be measured by taking the distance between the points $\lambda_\beta/4$ before and after a given point. A sample of this measurement is shown by the red bars on a portion of the betatron trajectory in Figure 2. 2. λ_β was then converted to ω_β. This measured ω_β (solid blue curve in Figure 2. 3) does not fall as predicted by Equation 1.9, which is the betatron frequency expected for an electron in an ion column (dotted blue curve in Figure 2. 3).

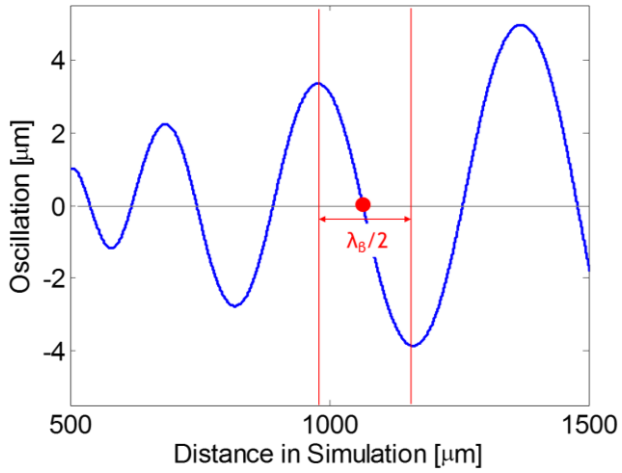

Figure 2. 2: Plot of a portion of the test electron's trajectory in the lab frame (blue curve). The red dot marks a zero of the betatron oscillation, and the instantaneous betatron wavelength $\lambda_\beta/2$ can be determined by finding the next-closest minima and maximum as marked by the red lines.

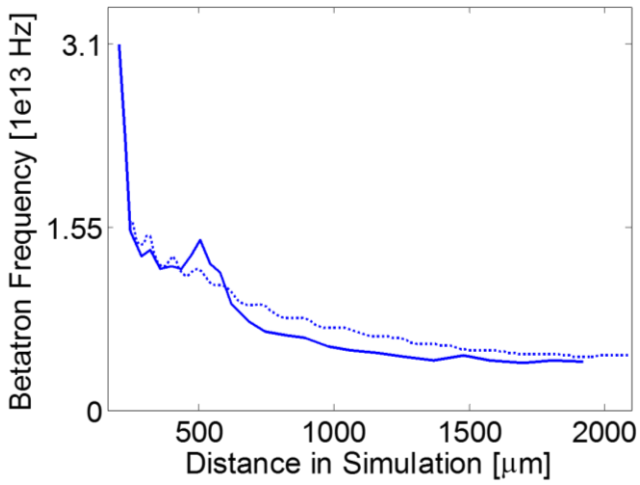

Figure 2. 3: Theoretical (dotted blue line) and measured-in-simulation (solid blue line) ω_β as a function of distance.

For this particular simulation, an instantaneous frame of the transverse electric field is recorded every 500 time steps. The phase velocity v_ϕ was calculated by measuring the advance of a constant-phase front of the laser cycle at the location of the test electron in each of those recorded simulation frames. An example of this measurement showing an advance Δz in a time Δt is shown in Figure 2. 4. Since the simulation window is moving at the speed of light, if the constant-phase front advances with respect to the simulation window as it does in Figure 2. 4, it indicates a phase velocity that is greater than the speed of light. This v_ϕ is expected from the plasma dispersion relation since there is residual plasma electron density on axis.

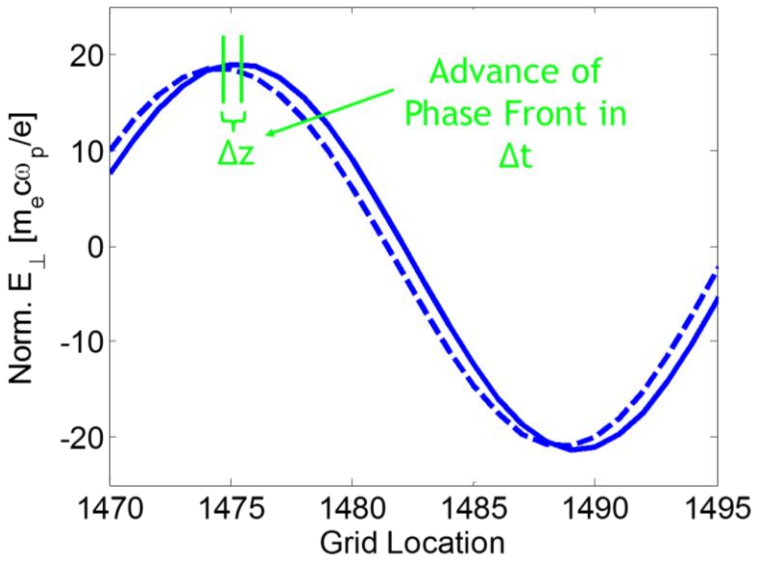

Figure 2. 4: Illustration of method used to calculate v_ϕ. The solid blue curve shows the advance Δz of the transverse electric field relative to the dashed blue curve 500 time steps (i.e. Δt) earlier. This method yields an average value of v_ϕ as long as the electron samples a particular laser cycle. When the electron slips into the next laser cycle, there is a discontinuity in the measurement of v_ϕ due to this method.

Figure 2. 5 shows that v_ϕ/c -1 (black curve) decreases with propagation distance because the percentage of blowout is increasing (i.e. the number of electrons on-axis is decreasing) as the drive laser and wake evolve. The quantity v_ϕ/c -1 is plotted instead of v_ϕ/c to emphasize the evolution of the phase velocity since Equation 1.8 is very sensitive to this quantity. The discrete nature of this curve is due to the method of measurement. Since the measurement considered the phase velocity of the laser cycle at the location of the electron, the average Δz of the phase front relative to the moving window can be measured for the Δt over which the test electron samples that particular cycle. That gives an average v_ϕ for one sampling period. However, when the electron slips to the next laser cycle, the continuity of the measurement is broken. The v_ϕ measurement must start again, which yields discrete jumps in the sampled v_ϕ.

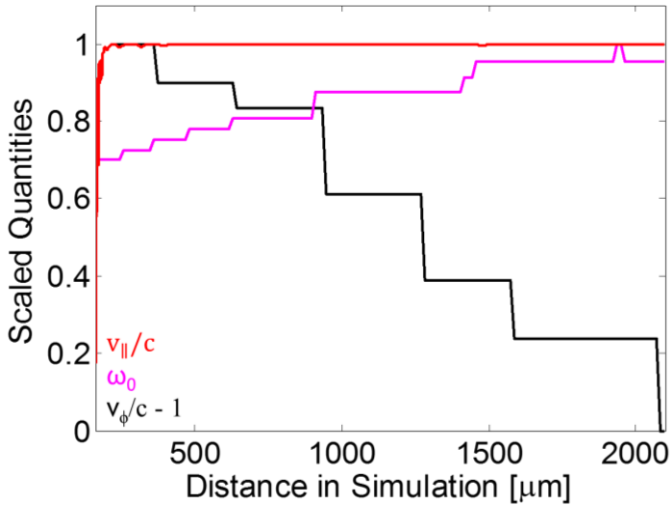

Figure 2. 5: Plot of the scaled quantities $v_{\|}/c$ (red curve), ω_0 (magenta curve), and v_ϕ/c -1 (black curve) as a function of propagation distance in the simulation. ω_0 and v_ϕ/c -1 are scaled to their maximum values of 3.3 x 10^{15} Hz and 1.0017, respectively. The plot starts at 160 μm into the simulation, which is where the test electron was born and which is located at the start of the constant-density region of the plasma. Where the electron is born, $v_\phi/c = 1.0017$ and $\omega_0 = 2.3 \times 10^{15}$ Hz. By the end, $v_\phi/c = 1.0004$ and $\omega_0 = 3.3 \times 10^{15}$ Hz.

Since γ and the longitudinal momentum $\mathbf{p}_{\|}$ are known as a function of distance from tracking the test electron through the simulation, $\mathbf{v}_{\|}$ can be directly calculated using $\mathbf{p}_{\|} = \gamma m_e \mathbf{v}_{\|}$. As Figure 2. 5 shows, $v_{\|}/c$ (red curve) quickly asymptotes to 1 because the test electron rapidly gains energy after it is born. Finally, the laser frequency was calculated by taking the on-axis lineout of the laser at each simulation frame, measuring the wavelength λ of the laser cycle at the location of the electron in that frame, and converting that wavelength to a frequency using $\omega_0 = 2\pi v_\phi/\lambda$. The discrete nature of the measurement of the laser wavelength is caused by the resolution (i.e. simulation grids per laser wavelength) of the simulation. Overall, it is clear from Figure 2. 6 that all four quantities (ω_β, $v_{\|}$, ω_0, and v_ϕ) present in the DLA resonance condition evolve significantly in a LWFA. The question that remains is whether that resonance condition holds while these quantities evolve.

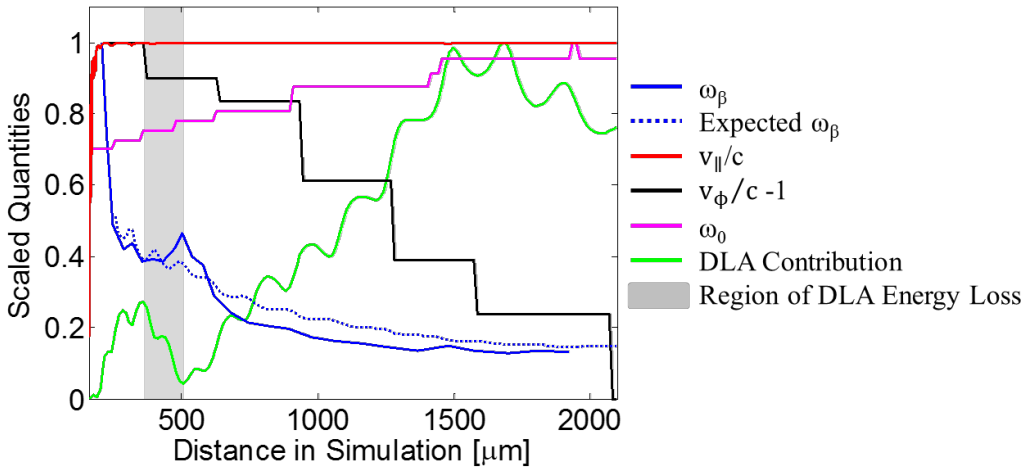

Figure 2. 6: Plot of the scaled quantities ω_β (solid blue curve), $v_\parallel/c$ (red curve), v_ϕ/c -1 (black curve), and ω_0 (magenta curve) as a function of propagation distance in the simulation. ω_β, ω_0, and v_ϕ/c -1 are scaled to their maximum values 3.1 x 10^{13} Hz, 3.3 x 10^{15} Hz, and 1.0017, respectively. The plot starts at 160 μm into the simulation, which is where the test electron was born and which is located at the start of the constant-density region of the plasma. Also plotted for reference is the DLA contribution calculated using Equation 2.2 (green curve) scaled to its maximum value of 93 MeV. For comparison, the expected ω_β (blue dotted curve) is also plotted after being scaled to 3.1 x 10^{13} Hz, which was the same value used to normalize the measured ω_β. The region over which the test electron first loses net energy to the transverse laser field is shaded gray.

Though all the quantities present in the DLA resonance condition are individually evolving, energy gain from DLA depends on how they change relative to each other. The evolution of $v_\parallel$, ω_0, and v_ϕ all affect the down-shifted laser frequency witnessed by the electron, which is given by the right-hand side of Equation 1.8 as $\left(1-v_\parallel/v_\phi\right)\omega_0$. This quantity, which was calculated using the measured values shown in Figure 2. 6, is plotted (red curve) in Figure 2. 7. This frequency oscillates over the duration of the simulation and reduces in magnitude where the test electron first loses energy to the transverse laser field (shaded region in Figure 2. 6 and Figure 2. 7). The value of the down-shifted laser frequency using the measured parameters from Figure 2. 6 is validated by a direct measurement of the down-shifted laser frequency $\omega_{0,frame}$ in the frame of the test electron (black curve in Figure 2. 7). $\omega_{0,frame}$ was directly measured in the simulation by finding the phase of the test electron relative to the peak of the laser cycle at the electron's location in each frame of the simulation as shown in Figure 2. 8 and then using $\omega_{0,frame} = d\phi/dt$.

Seeing that the right-hand side of Equation 1.8, $\left(1-v_{\parallel}/v_{\phi}\right)\omega_0$, accurately predicts the down-shifted laser frequency witnessed by the electron, it can then be compared to the left-hand side of Equation 1.8, $N\omega_{\beta}$, to see if the DLA resonance condition is satisfied where the test electron is gaining net energy from DLA. For this comparison, the value N=1 is taken because the electron slips roughly one laser cycle per betatron oscillation in this simulation.

Comparing the values of $N\omega_{\beta}$ and $\left(1-v_{\parallel}/v_{\phi}\right)\omega_0$ in Figure 2. 7 shows that right after the electron is born, both the betatron frequency and the down-shifted laser frequency sampled by the test electron are rapidly changing, which makes a one-to-one comparison difficult in this region where the test electron rapidly gains energy from DLA. However, shortly after this initial energy gain, the test electron experiences a rapid energy loss to the transverse laser field. In this region, not only does the betatron frequency stop falling, but also the down-shifted laser frequency is reduced significantly; as expected, the DLA resonance condition cannot be satisfied in this region. However, after this first and rapid loss of energy to the transverse laser field, the test electron again begins gaining energy from DLA for an extended duration. During this net energy gain from DLA, one would expect the left-hand side (blue curve in Figure 2. 7) and right-hand side (red curve in Figure 2. 7) of the DLA resonance condition to agree. However, this is not the case. Instead, the down-shifted laser frequency only agrees intermittently with the betatron frequency. Even though the test electron does not exactly satisfy the DLA resonance condition, it gains substantial energy over nearly four complete betatron oscillations. How this electron gains energy from DLA while only intermittently satisfying the resonance equation will now be explained.

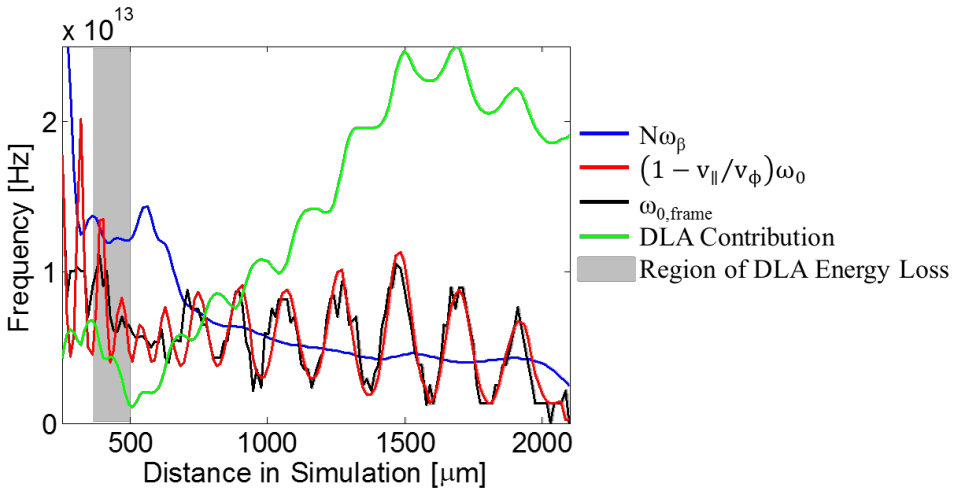

Figure 2. 7: $N\omega_\beta$ (blue curve) and $(1-v_\parallel/v_\phi)\omega_0$ (red curve) calculated for the test electron as a function of the distance into the simulation. Both curves were calculated using the values measured in Figure 2. 6. Also shown (black curve) is the laser frequency $\omega_{0,frame}$ witnessed by the electron in its frame. The green curve is the DLA contribution to the total energy gain scaled to its maximum value, and the shaded region marks where the electron first loses net energy to the transverse laser field.

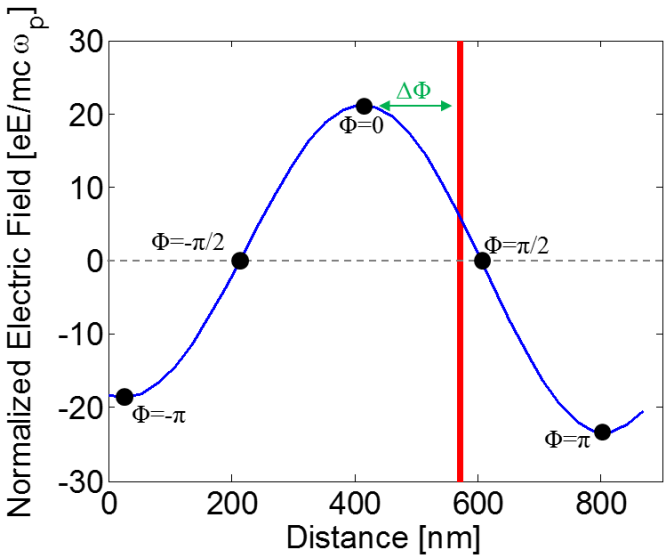

Figure 2. 8: Example measurement of the laser phase sampled by the test electron. The blue curve shows one complete laser cycle. The red line marks the location of the test electron, and the phase $\Delta\Phi$ that it samples is measured relative to the point $\Phi = 0$ assigned to the laser cycle.

The test electron can be used to investigate how DLA energy gain occurs even if the test electron can only intermittently satisfy the resonance condition. Energy gain occurs when the

transverse laser field and the transverse momentum of the electron have opposite signs. Therefore, since both $\mathbf{p}_\perp$ and $\mathbf{E}_\perp$ are known at each frame in the simulation, the locations where the test electron gains energy from the transverse laser field can be determined. Even though the resonance condition is not satisfied continuously where the electron gains net energy from DLA, the test electrons can gain this energy over an extended distance because the transverse momentum (dashed blue curve in Figure 2. 9) of the test electron and the transverse laser field (red curve in Figure 2. 9) evolve such that the electron is in an accelerating phase (solid blue portion of the transverse momentum in Figure 2. 9) for more than half of each betatron oscillation.

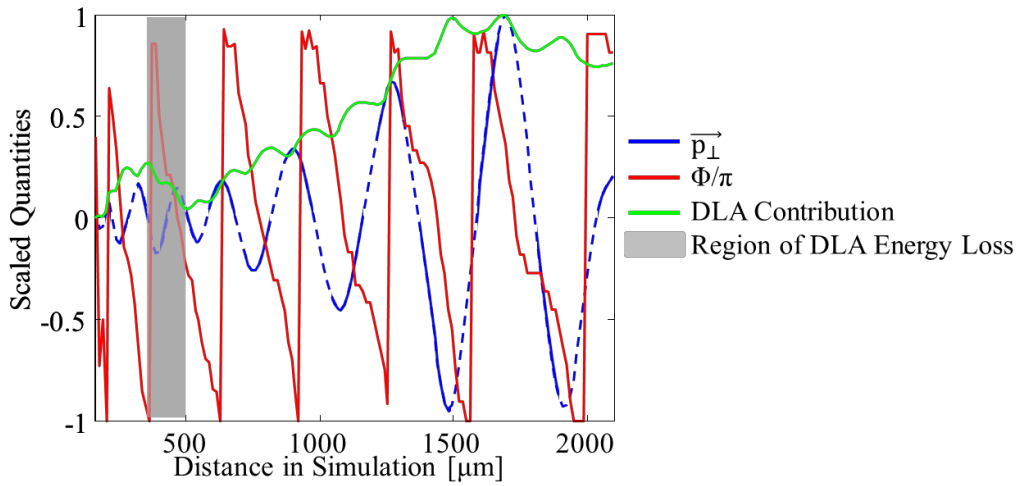

Figure 2. 9: Plot of the phase ϕ/π (red curve) of the test electron relative to the sampled laser cycle and of the transverse momentum (dashed blue curve) of the test electron scaled to its maximum value $p_\perp/mc=36.4$. As seen in Figure 2. 8, where the normalized Φ/π is between -0.5 and 0.5, the transverse laser field is positive. The solid blue regions along the transverse momentum curve indicate where the test electron is gaining energy from DLA. The discrete jumps in the phase curve mark where the test electron slipped back one laser cycle. The green curve is the DLA contribution to the energy gained by the test electron scaled to its maximum value, and the shaded area indicates where the test electron first experiences net energy loss to the transverse laser field.

In conclusion, in a LWFA system where both the properties of the electrons and the properties of the drive laser are evolving, trapped electrons can gain energy from DLA as long as the drive laser overlaps the trapped electrons. In this Section, we have shown that though such

electrons at best can only satisfy the 1D DLA resonance condition [1, 2] given by Equation 1.8 intermittently, they gain net energy from DLA in such regions because they are accelerated by the transverse laser field for more than one-half of each betatron cycle.

Section 2.2: Electron Beam Properties in Presence of DLA

With the understanding of how electrons that are being accelerated in a LWFA can gain energy from DLA over long portions of their propagation distance, we can now investigate through simulations how the presence of DLA in LWFAs affects the properties of the produced electron beams. In this Section, the simulations were again carried out using 2D OSIRIS in the speed-of-light frame with the Ammosov-Delone-Krainov (ADK) [16] ionization package. The simulation box size ranged between 36 x 54 c/ω_p = 67.8 x 101.6 μm where c/ω_p was 1.88 μm for the lowest-density (8 x 10^{18} cm^{-3}) simulation and 80 x 94 c/ω_p = 87.0 x 102.2 μm where c/ω_p was 1.09 μm for the highest-density (2.4 x 10^{19} cm^{-3}) simulation. The number of grid points was varied from 2494 x 452 = 1.13 x 10^6 to 3200 x 456 = 1.46 x 10^6 for the 8 x 10^{18} to 2.4 x 10^{19} cm^{-3} simulations, respectively. Sixteen particles per cell were used for a total of ~18-23 million particles for the 8 x 10^{18} to 2.4 x 10^{19} cm^{-3} simulations, respectively. The transverse resolution $k_p dx_\perp$ was between 0.12 and 0.21 for the 8 x 10^{18} to 2.4 x 10^{19} cm^{-3} simulations, respectively. The longitudinal resolution in the direction of laser propagation was $k_0 dx_{||}$ = 0.21 in all cases. At the outset, it should be stated that the transverse evolution of the laser pulse, the trapping efficiency of the ionization-injected electrons, and the degree of electron blowout will be somewhat different in 3D simulations compared to the 2D simulations presented here. Therefore, the results of the cases presented here are meant to qualitatively highlight the relative importance of the physical effects.

In the simulations, the initial neutral gas profile was trapezoidal with a uniform gas region that was 1800 μm long with 100 μm linear entrance and exit ramps on either side. The neutral gas

was comprised of 99.9% He and 0.1% N_2. The ionization of the K-shell electrons of the N_2 served to inject charge into the wake formed predominantly by the ionization of He atoms as soon as it is formed. The plasma density was varied from 8 x 10^{18} cm^{-3} to 2.4 x 10^{19} cm^{-3}. The central laser wavelength was 815 nm, and the laser pulse was focused in the center of the density upramp at the entrance of the plasma (see Figure 2. 10).

For the first two cases described below, the plasma density was 8 x 10^{18} cm^{-3}, and the FWHM laser pulse durations τ_{laser} were 30 fs and 45 fs. These pulse lengths correspond to T_p values of 0.5 and 0.8, respectively. The laser power P was 6.4 TW or P/P_{crit} was 1.8, where

$$P_{crit}\,[GW] \cong 17.4 \frac{\omega_0^2}{\omega_p^2} \tag{2.3}$$

is the critical power for self-focusing [3]. The laser spot size w_0 was 6.7 μm (half-width, half-max (HWHM) of intensity) giving a vacuum a_0 of 2.1. The laser's temporal profile was a polynomial fit to a Gaussian. In the $T_p = 0.5$ simulation, which acted as the control case, the laser pulse did not significantly overlap the trapped electrons, and therefore one does not expect a DLA contribution to the wakefield acceleration. The $T_p = 0.8$ simulation models the case where the back (falling intensity) of the laser pulse overlaps the trapped electrons, and therefore one might expect some contribution from DLA to the maximum energy gain.

The simulations were run to completion once to obtain the total energy gained by the trapped K-shell N_2 electrons and to identify the 40 electrons that had gained the most energy. The same simulations were subsequently run again to track the trajectories of these 40 electrons, while recording their position, their momentum, and the fields that the electrons sampled for each time step. The energy gained by the electrons due to LWFA was calculated for each tracked particle using Equation 2.1, and the DLA contribution was calculated using Equation 2.2. Note that no

direct energy exchange between an electromagnetic wave and a charged particle is possible unless the electron has a velocity component in the direction of the plane of the polarization of that wave. As stated earlier, in a LWFA such a transverse velocity component comes from the betatron motion of the electrons in the ion cavity of the wake. In DLA, this perpendicular momentum component is then amplified by the transverse field of the laser.

We first describe the results of the $T_p = 0.5$ "control" simulation in Figure 2. 10(a). For these laser and plasma parameters, complete expulsion of the plasma electrons, which characterizes the ideal blowout regime, was not observed. Only 73% of the electrons were evacuated resulting in a residual, on-axis plasma electron density of 2.1×10^{18} cm^{-3} within the first bucket. The energy gain due to the wakefield is approximately linear with distance, and the maximum energy gain is limited by dephasing [13]. The maximum energy gain (black curve) of these electrons is 234 MeV, which occurs at 1440 μm into the plateau region of the plasma. This location is 660 μm beyond the predicted dephasing length (Equation 1.5) of 780 μm, which is primarily due to the lengthening of the first bucket by the non-optimal 30-fs-long laser pulse. Consequently, the maximum electron energy exceeds the dephasing-length-limited energy gain ΔE of 150 MeV predicted by Equations 1.6 and 1.7. Recall that in this case, there is no significant overlap between the trapped electrons and the laser field at the back of the bucket where trapping occurs; thus, no DLA is expected. Figure 2. 10(a) indeed shows this to be the case. The wakefield contribution (red curve calculated using Equation 2.1) is the same as the total energy gain of the electrons (black curve). The DLA contribution (blue curve calculated using Equation 2.2) in this case is negligible. Therefore, for the LWFA regime where the laser pulse does not overlap the trapped electrons ($T_p \leq 0.5$), the wakefield is the only source of the energy gain for these highest-energy electrons as expected.

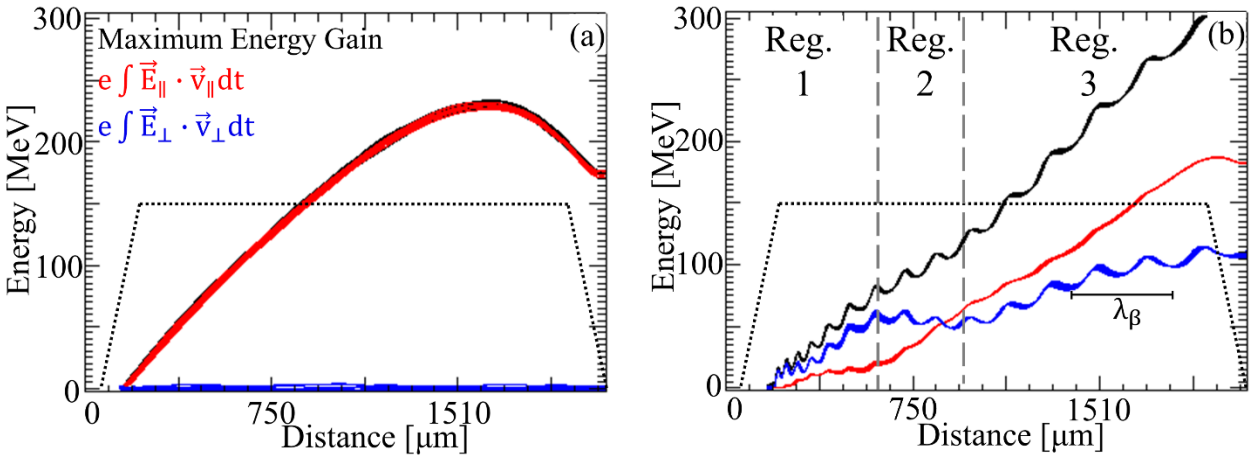

Figure 2. 10: (a) Plot of the maximum energy gain (black curve), LWFA contribution (red curve calculated using Equation 2.1), and DLA contribution (blue curve calculated using Equation 2.2) for the tracked electrons in the 2D OSIRIS simulation of a 30 fs laser pulse with an a_0 of 2.1 propagating through 1800 μm of 8 x 10^{18} cm^{-3} plasma. The dotted black curve marks the plasma density profile. (b) Plot of the maximum energy gain, LWFA contribution, and DLA contribution as a function of the distance for a 45 fs laser pulse with an a_0 of 2.1 propagating in the same plasma as (a). In Regions 1 and 3, the electrons are gaining energy from DLA. In Region 2, the electrons are slowly losing energy to the transverse laser field. Note that all the electrons in (b) oscillate nearly in phase with one another.

The results of the energy gain by the highest-energy electrons for the T_p = 0.8 case are shown in Figure 2. 10(b). In this simulation, complete blowout of the plasma electrons is again not seen. The typical residual on-axis plasma density was 3.2 x 10^{18} cm^{-3}, which corresponds to 60% blowout. Figure 2. 10(b) shows that the maximum energy gain (black curve) in the T_p = 0.8 case is 302 MeV, which is 29% higher than the energy gain in the control simulation (T_p = 0.5) with no DLA and corresponds to an acceleration gradient of 168 GeV/m. The maximum LWFA contribution (red curve) is 187 MeV and occurs 11 μm into the density downramp. There is negligible energy gain in this 11 μm of density downramp. The acceleration due to LWFA persisted for a distance more than twice the dephasing length of 780 μm predicted by the scaling for the ideal blowout regime [13]. There are two primary factors that contribute to this increased dephasing length. First, the 45-fs laser pulse elongates the bucket even more than the 30-fs pulse.

Second, the increase in transverse momentum due to DLA slightly reduces the longitudinal velocity of the electrons, effectively further increasing their dephasing length compared to the T_p = 0.5 simulation where no DLA is observed [11, 17]. For this case, the maximum DLA contribution (calculated using Equation 2.2) is 115 MeV. Comparing the LWFA contribution of 204 MeV to the maximum energy gain of 302 MeV shows that the wakefield only accounts for approximately 2/3 of the maximum energy gain.

In Figure 2. 10(b), one can clearly see a sinusoidal structure on both the DLA contribution and the maximum energy gain. This structure is due to the betatron motion of the accelerating electrons. The betatron wavelength λ_β was measured for each oscillation in the simulation and plotted against the average electron energy over that period in Figure 2. 11. To put some theoretical bounds on this plot, the theoretical λ_β is plotted for full blowout (blue curve) and for 60% blowout (red curve), which is representative of the blowout seen in the simulation. Figure 2. 11 shows that the measured data falls within the theoretical expectations and verifies that the sinusoidal structure on the maximum electron energy and the DLA contribution curves in Figure 2. 10(b) is caused by the betatron motion of the trapped electrons in the ion column. As the energy of the electrons increases, so does the oscillation wavelength as might be expected since

$$\lambda_\beta = \frac{2\pi c\sqrt{2\gamma}}{\omega_p} \tag{2.4}$$

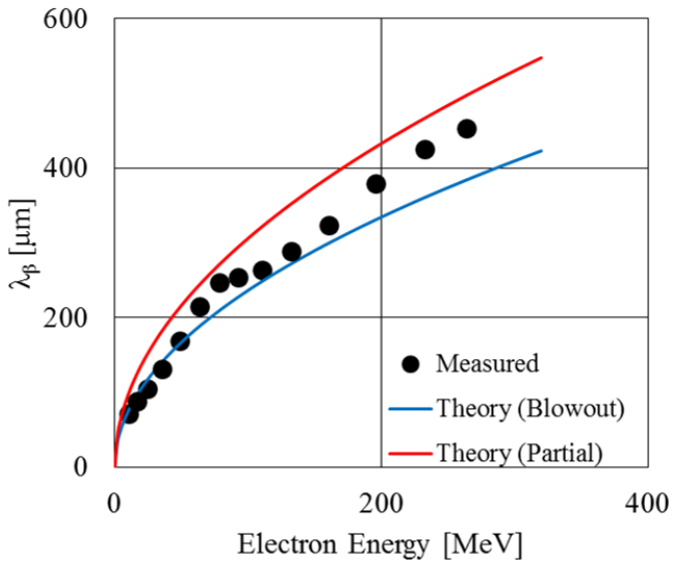

Figure 2. 11: Plot of the betatron wavelength measured in the $T_p = 0.8$ simulation (black dots) versus the average electron energy over that oscillation. The blue curve shows the theoretical betatron wavelength calculated using Equation 2.4 assuming complete blowout. The red curve shows the theoretical betatron wavelength accounting for the partial (60%) blowout seen in the simulation.

A closer examination of the DLA contribution in Figure 2. 10(b) reveals that the DLA contribution does not steadily increase. Rather, it initially increases up to 620 μm (Region 1), then slightly falls until 930 μm (Region 2), and then begins rising again (Region 3). This behavior of the DLA contribution arises because the electrons gain and return energy to the transverse laser field depending on their relative phase with respect to the laser field as discussed in Section 2.1.

Since the total possible DLA contribution is proportional to the transverse field of the laser as shown in Equation 2.2, it should increase if the electrons are overlapped with the more intense regions of the laser pulse. To investigate this hypothesis, five simulations were carried out that had parameters identical to the control ($T_p = 0.5$) simulation except that the plasma density was varied between 8×10^{18} cm^{-3} to 2.4×10^{19} cm^{-3} so that different regions of the $\tau_{laser} = 30$ fs laser pulse would overlap the trapped electrons. The maximum possible DLA and LWFA contributions were measured in each simulation, and the results are shown in Figure 2. 12. This figure confirms

that the maximum possible DLA contribution increases with T_p in this regime of LWFA. Figure 2. 12 also shows that the maximum possible LWFA contribution decreases with increasing T_p, which suggests that the contribution of DLA can exceed that of the wake. Therefore, Figure 2. 12 shows that the dominant energy gain mechanism for the highest-energy electrons can transition from LWFA to DLA as T_p is increased.

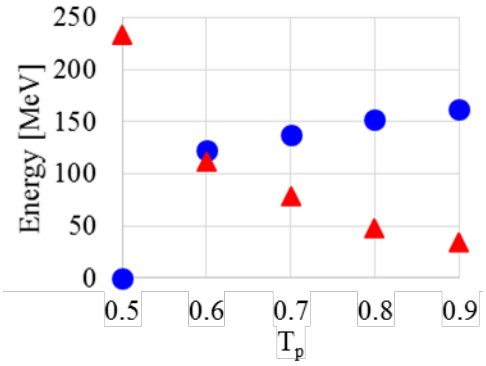

Figure 2. 12: Plot of the maximum possible DLA and LWFA contributions versus T_p. The blue dots mark the maximum possible DLA contribution in each simulation, which occurs at 1163, 832, 611, and 513 µm into the constant density regions of the 1.2 x 10^{19} (T_p = 0.6), 1.6 x 10^{19} (T_p = 0.7), 2.0 x 10^{19} (T_p = 0.8), and 2.4 x 10^{19} (T_p = 0.9) cm^{-3} simulations, respectively. The red triangles mark the maximum LWFA contribution, which occurs at 1457, 825, 561, 303, and 269 µm into the constant density regions of the 8 x 10^{18} (T_p = 0.5), 1.2 x 10^{19} (T_p = 0.6), 1.6 x 10^{19} (T_p = 0.7), 2.0 x 10^{19} (T_p = 0.8), and 2.4 x 10^{19} (T_p = 0.9) cm^{-3} simulations, respectively.

In conclusion, we have used 2D OSIRIS PIC simulations to investigate LWFA with ionization injection of electrons in a quasi-blowout regime where the laser pulse overlaps the trapped electrons. The electron beams produced have maximum electron energies that exceed the dephasing-length-limited energy estimates given by the theory for the ideal blowout regime. The simulations show that DLA can be an additional acceleration mechanism when the LWFA is operating in this regime. The relative contributions to the maximum electron energy from LWFA and DLA were determined, and it was demonstrated that the DLA contribution increases with T_p as expected.

Section 2.3: Resolution Effects on DLA in PIC Simulations of LWFA

In 2014, Lehe et al. [18] found that in PIC code simulations of a laser field interacting with an electron in vacuum, numerical effects can lead to an overestimation of the transverse momentum and excursion of an electron and can ultimately lead to spurious heating. This overestimation can happen when the magnetic field is not calculated with enough precision in a PIC code that is using the standard Yee algorithm [19]. In such a code, the macroparticles are distributed across the grid and therefore may not fall exactly on the grid itself. Consequently, before calculating the force on each particle, the electric and magnetic fields need to be extrapolated from the grid to the location of the macroparticles. Additionally, since the magnetic field is defined at half time steps in the Yee algorithm, it needs to be interpolated in time since the Lorentz force on the macroparticles is calculated at integer time steps. If a simple time average is used to interpolate the magnetic field, the resulting error can lead to artificial growth in the transverse trajectories and momentum of the electrons; this artificial growth disappears when a third-order interpolation method is used [18]. Since the DLA mechanism depends upon the transverse motion of the electrons in an ion column, in this Section we explore the extent to which the DLA of electrons in LWFAs may be affected by these numerical effects in PIC code simulations. We find that contrary to expectation, the DLA effect persists and can significantly contribute to the total energy of the electrons even when the simulation resolution is significantly increased.

To explore if the numerical effects are influencing the estimation of the relative contribution of DLA in LWFA, we ran a series of 2D OSIRIS PIC code simulations with increasing longitudinal and transverse resolutions. In the transverse direction, the laser phase is approximately constant and the laser amplitude envelope is slowly varying on the scale of the grid,

so the transverse resolution is not expected to have a large impact on the results. Indeed, there was no appreciable difference when the transverse resolution was increased, and therefore only the effects of the longitudinal resolution are presented in this Section. The longitudinal resolution is expected to have a much larger effect because the laser phase varies rapidly in the longitudinal direction and the speed of light in these simulations is dominated by the value of the longitudinal resolution. The longitudinal resolution effects were examined by reducing the grid size in the longitudinal direction. This increase in longitudinal resolution increases the accuracy when extrapolating the fields to the macroparticles, and subsequently reduces the time step, which improves the accuracy of the interpolation of the magnetic field in time. Though the best practices in the choice of resolutions used in PIC code simulations of LWFA vary from research group to research group, our research group at UCLA has settled on a standard resolution of 40 grid points per laser spot size and of 30 grid points per laser wavelength (pts/λ) [20] for LWFA simulations. Testing via convergence studies [20] has demonstrated that when using this longitudinal resolution in OSIRIS, any error in the laser propagation becomes small and the wakefields converge.

The laser and plasma parameters used in this particular series of simulations model the achievable experimental parameters of our experiments on the 10-20 TW Ti:Sapphire laser in the Xtreme Plasma Laboratory at UCLA. The simulation box is comprised of a 63.63 μm by 18.86 μm window that moves at the speed of light. The grid in that window is 2342 x 472 with 16 particles per cell. The laser pulse is focused to a spot size w_0 of 7.2 μm halfway up a 150-μm-long density upramp. The laser pulse ionizes an initially-neutral mixture of 0.5% N_2 and 99.5% He so that charge is trapped in the wake via ionization injection. The produced plasma density has a maximum value of 6.3×10^{18} cm^{-3} and a constant-density plateau of 1400 μm with 150-μm-long linear density upramp and downramp. The laser pulse has a central wavelength of 815 nm and an

a_0 of 2.8. Its pulse length is 60 fs (FWHM of intensity) so that the laser overlaps the trapped electrons ($T_p = 0.8$); thus DLA is expected to contribute to the final energy of these electrons. The standard-resolution simulation uses $k_0\Delta z = 0.209$ and $k_p\Delta x = 0.085$ to resolve the longitudinal and transverse dimensions, respectively. The resulting normalized time step is 0.01265.

The next two simulations in the series are identical to the standard-resolution simulation with the exception of the number of grid points in the longitudinal direction and the subsequent change in the time step. For the double-resolution case (where the longitudinal resolution is increased to 60 points per laser wavelength), the grid is 4682 x 472. The resulting $k_0\Delta z$ is reduced to 0.105, and the normalized time step is reduced to 0.00638. For the quadrupole-resolution case (longitudinal resolution of 120 points per laser wavelength), the grid is 9368 x 472. The resulting $k_0\Delta z$ is further reduced to 0.052 and results in a reduced normalized time step of 0.00320. Each simulation was run to completion, and the trapped electrons were filtered to select only those electrons that were accelerated in the first bucket and exited the plasma. From those electrons, the 5 highest-energy electrons and 500 random electrons were tagged. The simulation was then rerun with those tagged particles so that the momentum, position, and fields sampled by those electrons at each time step are known. From this information, it is possible to determine whether the electrons gain energy from DLA, from LWFA, or from both.

When DLA is present in a LWFA, the electrons' motions become remarkably different than in the case with only wakefield acceleration. This difference is especially pronounced when ionization injection is used because the electrons are ionized inside the first period of the wake and they can gain sizeable transverse momentum as they slip backwards in the wake. These two effects can change the position of the electron trapping relative to the case where no laser field is present. Also, the effective distance for dephasing in the longitudinal field is affected by both this change

in the trapping location and the length of the laser pulse relative to the wake wavelength. Furthermore, electrons can continue to gain energy due to DLA even after dephasing with respect to the wake. In this case, the final energy of the electrons may increase or decrease depending on the relative contribution of the two mechanisms to the overall energy of the particle. To isolate the LWFA effect, we therefore carried out one additional simulation where the pulse length was reduced to 35 fs so that there is no overlap between the laser and the trapped electrons ($T_p = 0.5$). This additional simulation is identical to the standard-resolution simulation in all other respects and therefore the results serve as a baseline to examine the transverse momentum and oscillation when DLA is not present.

The oscillation radius and the transverse momentum of 5 of the highest-energy W_{max} electrons for the simulations with a 35 fs pulse (where no DLA is present and $W_{max} = 331$ MeV) and a 60 fs pulse (where DLA contributes to the energy gained by the electrons and $W_{max} = 199$ MeV) are compared in Figure 2. 13. Figure 2. 13(a) shows that the typical extent of the betatron oscillation in the 60 fs case is ~ 4 μm, which is more than 5 times the typical excursion of ~ 0.7 μm in the 35 fs simulation. Furthermore, Figure 2. 13(b) shows that the normalized transverse momentum $p_\perp/mc$ can reach 35 when DLA is present in the $\tau_{laser} = 60$ fs case, where the wake-only $\tau_{laser} = 35$ fs case reaches a much more modest 5. It is clear from this figure that both the transverse oscillation amplitude (Figure 2. 13(a)) and momentum (Figure 2. 13(b)) are significantly increased when the laser pulse overlaps the trapped electrons and DLA is present in addition to LWFA, and it emphasizes why it is critical to determine whether these dramatic increases in the transverse momentum and excursion are physical or merely a numerical artifact of the PIC algorithm as described earlier.

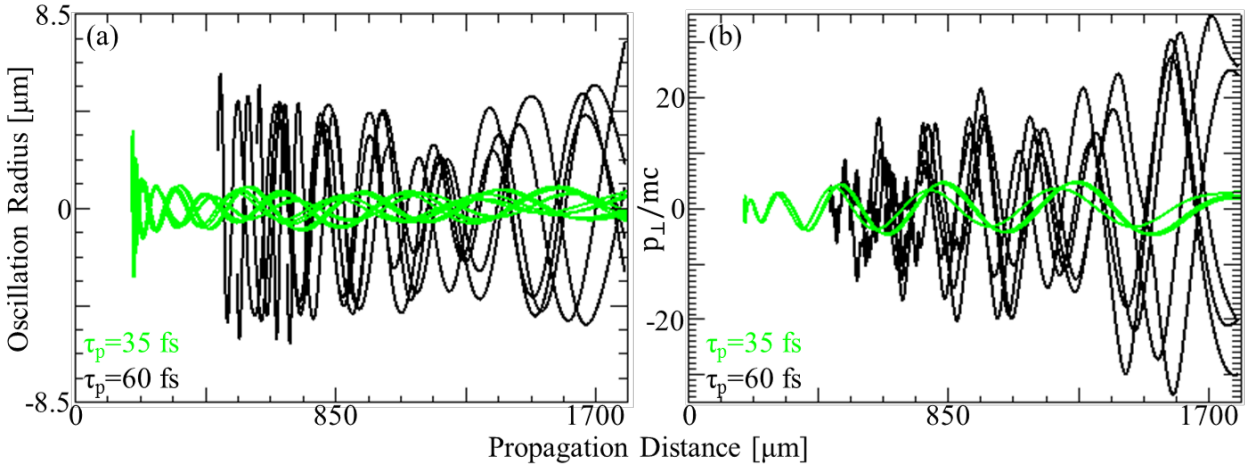

Figure 2. 13: (a) Plot of the electron trajectories for the 5 highest-energy electrons in the τ_{laser} = 35 fs (green curves) and τ_{laser} = 60 fs (black curves) simulations. (b) Normalized transverse momentum as a function of the propagation distance for the τ_{laser} = 35 fs (green curves) and τ_{laser} = 60 fs (black curves) simulations. Note that the highest-energy electrons are trapped much earlier in the τ_{laser} = 35 fs case.

To investigate if reduced resolution can lead to an artificial growth of the transverse oscillation extent of electrons in a laser field [18], we carried out the exact same 60 fs simulation but with three different longitudinal resolutions (see Figure 2. 14). The color bar has been slightly saturated to emphasize the extent of the trapped charge. For the standard-resolution case (Figure 2. 14(a)), the trapped charge has a large transverse extent of ~ ±8.5 μm and is deeply modulated at half of the laser wavelength [21]. Here, the charge density is the largest at the farthest extents of the modulation. When the resolution is doubled (Figure 2. 14(b)), the bunching is reduced. Though there is still charge bunched at half of the laser wavelength, its maximum transverse extent is reduced to ~ ±7 μm and the depth of modulation has decreased. In this case, more of the trapped charge is located on-axis relative to the standard-resolution case. The bunching is further washed out when the resolution is quadrupled (Figure 2. 14(c)). This finding suggests that reduced resolution indeed enhances the transverse motion of the electrons. This enhanced transverse motion also leads to increased divergence at lower resolutions. For the standard-resolution case, the divergence of the electron beam after exiting the plasma was 100 mrad. The divergences of the double- and quadruple-resolution cases were 70 and 50 mrad, respectively. Though 2D PIC

code simulations typically over-estimate the divergence of the electron beam produced from a LWFA as compared to an equivalent experimental system, the relative magnitudes illustrate the effect of the longitudinal resolution on the divergence.

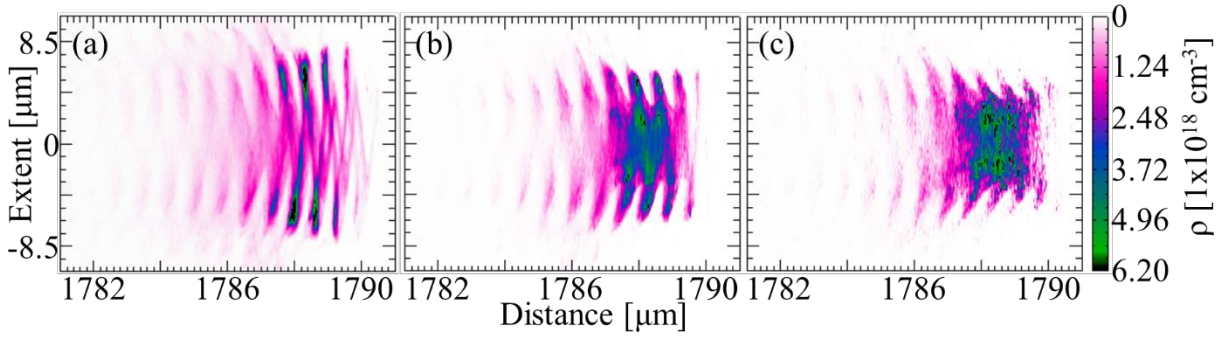

Figure 2. 14: Plots of the trapped charge after it exits the plasma for the (a) standard-, (b) double-, and (c) quadrupole-resolution simulations. τ_{laser} = 60 fs in all cases.

In a LWFA where the laser pulse overlaps the trapped electrons, DLA can be expected to contribute sizably to the final energy of the highest-energy electrons [9, 11, 12, 17, 22-24]. If this energy gain due to DLA is purely a numerical artifact, then the reduced extent of the transverse oscillations seen in the higher-resolution simulations in Figure 2. 14 should correlate with a decreased DLA contribution to the energy gained by the electrons and hence a reduction in the maximum electron energies produced by the LWFA. However, as Figure 2. 15 shows, the high-energy tails of the electron spectra in the higher-resolution simulations actually push to larger energies, and the electron spectra converge within 10% for resolutions greater than 60 grid points per laser wavelength due to the improved interpolation of the magnetic field and the improved extrapolation to the macroparticles. To understand why the higher-energy tails of the spectra shown in Figure 2. 15 do not decrease with resolution as expected given the results of Figure 2. 14, the relative contributions to the final energies of those highest-energy electrons must be explored.

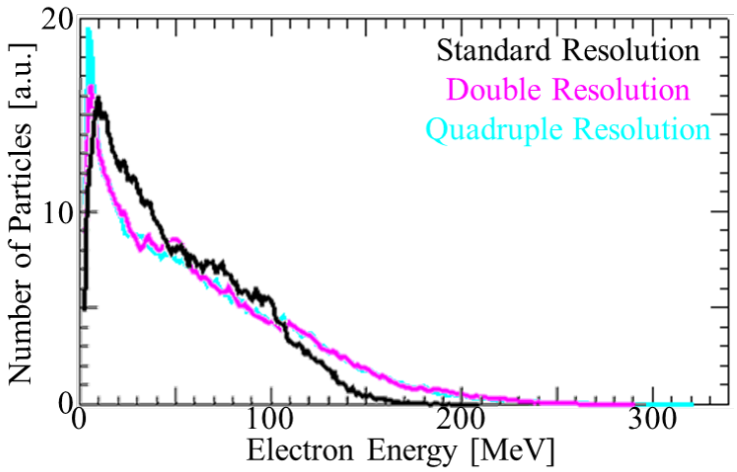

Figure 2. 15: Final energy spectra of the electrons accelerated in the first bucket of the wake for the standard 30 pts/λ (black), double 60 pts/λ (magenta), and quadrupole 120 pts/λ resolution (cyan) simulations. The two higher-resolution spectra have converged. The small random variation between the three spectra arises because only 20% of the macroparticles are extracted and saved.

Using the values from tracking the 5 highest-energy particles, the LWFA and DLA contributions to the final energy of the electrons was calculated using Equation 2.1 and Equation 2.2, respectively. Figure 2. 16(a) shows that in the standard-resolution $\tau_{laser} = 60$ fs simulation, the trapped electrons reach a maximum energy of 199 MeV upon exiting the plasma. Comparing the LWFA contribution (red curve) to the total electron energy curve (black curve) shows that the wakefield only accounts for approximately half of the total energy gained by the electrons. The other half of the energy gains comes from DLA as shown by the blue curve in Figure 2. 16(a). However, these electrons do not continuously gain energy from DLA. Rather, once they are trapped, they gain energy from DLA for ~ 360 μm before coming out of resonance [9, 22] and losing all the energy that they had gained from DLA. At ~ 1250 μm, they regain resonance and are accelerated by DLA until exiting the plasma.

A similar comparison for the double-resolution case (Figure 2. 16(b)) shows that the DLA contribution to the final energy gain is not merely a numerical artifact. In this case, the maximum energy reaches 285 MeV, and the DLA contribution has actually increased relative to the standard-

resolution case because the electrons are able to maintain the DLA resonance condition for much longer distances. In this case, after the electrons are trapped, they gain a small amount of energy from DLA and then quickly lose it. But then they regain the DLA resonance and maintain it for a long acceleration distance, which permits large energy gain from DLA. In fact, for the highest-energy electrons in the double-resolution case, LWFA only contributes up to 31.6 MeV to the final electron energy, and some electrons are actually losing energy to the wake as they exit the plasma. The LWFA contribution is reduced in this case relative to the standard-resolution case because these electrons propagate farther forward in the wake and are therefore in either a weakly-accelerating or a decelerating longitudinal field as they continue to gain energy from DLA.

In the quadruple-resolution case (Figure 2. 16(c)), the maximum electron energy has increased yet again to a final energy of 328 MeV at the exit of the plasma. The DLA contribution to the highest-energy electrons has increased 28% relative to the double-resolution case, and all of the 5 highest-energy electrons are actually losing energy to the wake. In this case, the DLA contribution has increased even relative to the double-resolution case because the electrons come into resonance earlier and therefore gain energy from DLA for an even longer acceleration length. Further, the gradient is 10% larger in this case, which coupled with the larger loss of energy to the wake, means that the electrons have dephased and are propagating farther forward in the wake relative to the double-resolution case in a decelerating longitudinal field while continuing to be accelerated by DLA in a higher-intensity portion of the laser pulse.

The differing ability of each resolution case to maintain DLA resonance can be clearly seen when examining the trajectories of one of the 5 highest-energy electrons as shown in row 2 of Figure 2. 16. The oscillation radius is expected to be largest for the standard-resolution case (Figure 2. 16(d)), and indeed we see that when the electron is first trapped and gaining energy from

DLA, it has the largest radius. However, as soon as that electron comes out of resonance, its radius is drastically reduced. Yet once it regains resonance, its transverse oscillation amplitude quickly surpasses the oscillation radii of the double- (Figure 2. 16(e)) and quadruple- (Figure 2. 16(f)) resolution cases. In the double-resolution case, when the electron is initially in resonance, its oscillations grow in radii, but not to as large of an extent as in the standard-resolution case. The electron then comes out of resonance and the oscillation radius decreases. It then regains resonance and the oscillation radii again grow, but again these amplitudes are lower than in the standard-resolution case. In the quadruple-resolution case (Figure 2. 16(f)), the electron is trapped and then comes in and out of the DLA resonance in a short distance. Then that electron again comes into DLA resonance, and its oscillation radius grows slowly as the electron remains in resonance. However, even with the sustained resonance, the oscillation radii never grow larger than in the standard-resolution case. Therefore, an inspection of the trajectories supports the idea that lower resolutions can lead to enhanced transverse motion, but it also shows that such an increase does not lead to artificial energy gain by DLA because the electrons maintain the DLA resonance condition for shorter distances in lower-resolution simulations.

It is also predicted that the transverse momentum should be artificially enhanced in the lower-resolution case. Examining the normalized transverse momentum of the electrons (third row of Figure 2. 16), shows the same trend as the transverse oscillations— the transverse momentum is reduced when an electron is out of DLA resonance, yet once in DLA resonance, the transverse momentum of the electron in the standard-resolution case quickly grows to larger values than in the double- and quadruple-resolution cases.

Thus, Figure 2. 16 confirms that DLA is not purely a numerical artifact but rather that it is a physical effect that continues to play a large role in the energy gained by the highest-energy

electrons produced from a LWFA in the forced or blowout regimes with a_0 ~2 – 4 and $T_p > 0.5$ even at increased resolutions. The required resolution for a LWFA with a_0 values larger 4 may be somewhat different and would require further study. Furthermore, Figure 2. 16 shows that the highest electron energies actually increase with increasing resolution because the electrons are better able to maintain the DLA resonance. The resulting increase in the DLA contribution to the final electron energies explains why the maximum energy of the electron spectra (Figure 2. 15) increases with resolution despite the reduction in the transverse extent as seen in Figure 2. 14.

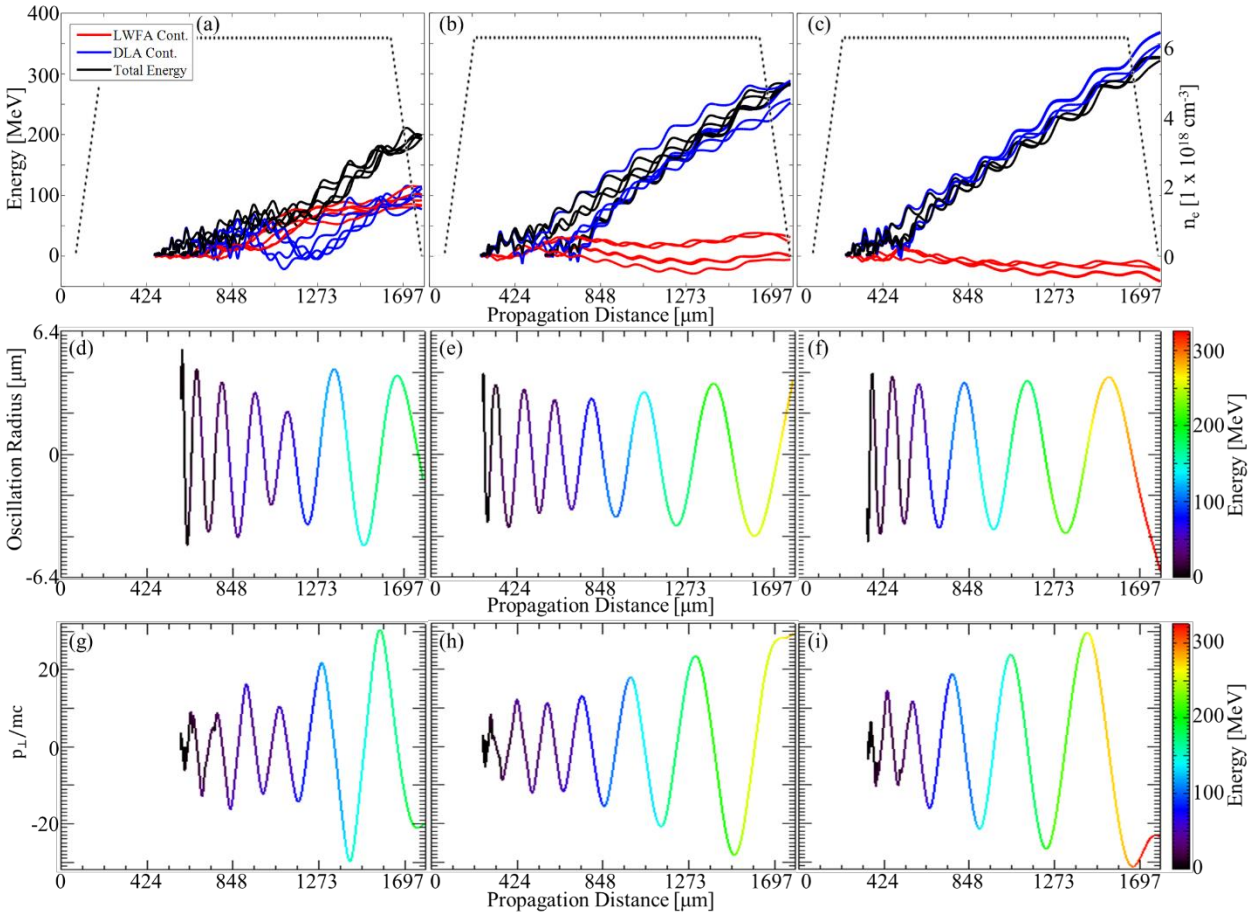

Figure 2. 16: First Row: Plots of total electron energy (black curves), LWFA contribution to the electron energy (red curves), and DLA contribution to the electron energy (blue curves) as a function of the propagation distance for the (a) standard-, (b) double-, and (c) quadruple-resolution cases. Curves are shown for the 5 highest-energy electrons in each simulation. Black dotted line shows the plasma density profile used in the simulation. For all three cases, there was ~ 10% residual electron density on axis inside the first period of the wake. Second Row: Plots of the trajectories of one of the 5 highest-energy electrons for the (d) standard-, (e) double-, and (f) quadruple-resolution cases. Third Row: Plots of the normalized transverse momentum of the same electrons as in row 2 as a function of propagation distance for the (g) standard-, (h) double-, and (i) quadruple-resolution simulations.

The relative contribution of DLA and LWFA to the final energies of the 500 randomly-tagged electrons, which are representative of the total electron spectrum, is also examined to determine if the role that DLA plays in accelerating the bulk of the electrons also increases when the resolution is increased. For each resolution, the LWFA contribution to the final electron energy was calculated for the 500 random electrons using Equation 2.1. For the standard-resolution case, 92% of the electrons gain some energy from LWFA. For the double- and quadruple-resolution

cases, this percentage is 81% and 87%, respectively. These percentages are similar and show that LWFA is still important in accelerating the bulk of the charge in a LWFA where the drive laser overlaps the trapped electrons. In the double- and quadruple-resolution cases, the maximum LWFA contributions of 176 MeV and 177 MeV, respectively, cannot account for the energies of the highest-energy electrons. Therefore, as already seen in Figure 2. 16, DLA is necessary in addition to LWFA to produce those highest electron energies.

The DLA contribution to the final electron energy of the randomly-tagged particles was calculated using Equation 2.2. For the standard-resolution case, the maximum DLA contribution is 97 MeV, and 87% of the electrons gain some energy from the DLA mechanism. In the double-resolution case, the maximum DLA contribution is 229 MeV, and 76% of the electrons gain energy from DLA. In the quadruple-resolution case, the maximum DLA contribution is 243 MeV, and 83% of the electrons gain energy from DLA. These percentages are similar in all three cases and show that DLA is also important for accelerating the bulk of the electrons. Furthermore, even in the bulk of the electrons, the maximum DLA contribution increases relative to the standard-resolution simulation when the resolution is increased.

In conclusion, by investigating a series of OSIRIS simulations with increasing longitudinal resolutions, this Section has demonstrated that the DLA of electrons in a LWFA is a physical effect that contributes significantly to the energy gain of the electron beam. Although the transverse momentum and oscillation extent experience some numerical heating in the lower-resolution simulations, that artificial heating does not translate to artificial DLA. In fact, at lower resolutions, the highest-energy electrons are not able to maintain the DLA resonance for as long of a distance, which results in lower contributions of DLA to their final energies relative to the higher-resolution simulations. For all resolutions, DLA contributes to the acceleration of the bulk of the electrons.

Clearly, higher-resolution simulations are required to fully explore the role that DLA plays in the energy gain of electrons.

Conclusion

This chapter has presented the findings of the major simulation work investigating the DLA of electrons that are being accelerated in a LWFA in the quasi-blowout regime. It was shown that DLA can be an additional acceleration mechanism in a LWFA where the drive laser overlaps the trapped electrons. In this regime, those trapped electrons gain net energy from DLA because they are accelerated by the transverse laser field for more than one-half of each betatron cycle. This allows those electrons to gain energy from DLA even though such electrons at best can only satisfy the 1D DLA resonance condition intermittently. The produced electron beams were shown to have maximum electron energies that exceed the dephasing-length-limited energy estimates given by the theory for the ideal blowout regime and a matched laser pulse. The relative contributions to the maximum energy of these electron beams from LWFA and DLA were determined, and it was demonstrated that the DLA contribution increases with T_p as expected. Finally, by investigating a series of OSIRIS simulations with increasing longitudinal resolutions, it was shown that the DLA of electrons in a LWFA is not merely a numerical artifact, but rather that it is a physical effect that contributes significantly to the energy gain of the electron beam.

Ch. 2 References

[1] A. Pukhov et al., Phys. Plasmas **6**, 2847 (1999).

[2] A. Pukhov, Reports on Progress in Physics **66**, 47 (2003).

[3] G. Z. Sun et al., Phys. Fluids **30**, 526 (1987).

[4] S. C. Wilks et al., Phys. Rev. Lett. **62**, 22 (1989).

[5] A. Ting et al., Phys. Fluids B **2**, 1390 (1990).

[6] S. V. Bulanov et al., Phys. Fluids B **4**, 1935 (1992).

[7] W. Horton and T. Tajima, Phys. Rev. A **34**, 5 (1986).

[8] D. Teychenné et al., Phys. Plasmas **1**, 1771 (1994).

[9] J. L. Shaw et al., *Proceedings of the 2014 Advanced Accelerator Concepts Workshop. http://arxiv.org/abs/1502.07664v1*.

[10] R. A. Fonseca et al., in *Lecture Notes in Computer Science*, Vol. 2331 (Springer Berlin Heidelberg, 2002) pp. 342-351.

[11] J. L. Shaw et al., Plasma Phys. Contr. F. **56**, 084006 (2014).

[12] J. L. Shaw et al. Plasma Phys. Contr. F. **58**, 034008 (2016).

[13] W. Lu et al., Phys Rev. Spec. Top. – Accel. Beams **10**, 061301 (2007).

[14] W. B. Mori, IEEE J. Quantum Electron. **33**, 1942 (1997).

[15] A. Pak et al., Phys. Rev. Lett. **104**, 025003 (2010).

[16] M. Ammosov, N. Delone, and V. Krainov, Sov. Phys. JETP **64**, 1191 (1986).

[17] X. Zhang et al., Phys. Rev. Lett. **114**, 184801 (2015).

[18] R. Lehe et al., Phys Rev. Spec. Top. – Accel. Beams **17**, 121301 (2014).

[19] K. Yee, IEEE Trans. Antennas Propag. **14**, 302 (1966).

[20] F. S. Tsung et al., Phys. Plasmas **13**, 056708 (2006).

[21] N. Lemos et al., *Proceedings of the 2014 Advanced Accelerator Concepts Workshop. http://arxiv.org/abs/1502.07764v1*.

[22] J. L. Shaw et al., *Submitted to Phys. Rev. Lett.*

[23] X. Zhang et al., Plasma Phys. Contr. F. **58**, 034011 (2016).

[24] N. Lemos et al., Plasma Phys. Contr. F. **58**, 034018 (2016).

Ch. 3: Experimental Methods

Introduction

In this chapter, we present an overview of the laser and plasma parameters typically used in our experimental work to investigate DLA in LWFA. This overview is followed by a detailed description of the variable-length gas cells that we designed for LWFA experiments to generate reproducible, constant-density plasma sources with short entrance and exit ramps [1]. We conclude this chapter by describing in detail a curve-fitting method [2] that we developed to determine the maximum energy of LWFA-produced electron beams that have a continuous energy spread.

Section 3.1: Experimental Setup

The experiments presented in this dissertation were conducted at UCLA's Xtreme Plasma Laboratory using the 815-nm Ti:Sapphire laser with a fixed pulse length τ_{laser} of 45 ± 5 fs FWHM of intensity and a spot size w_0 of 6.7 μm. The laser was run with powers P up to 10 TW, which correspond to an a_0 up to 2.6. An f/6 off-axis parabola (OAP) system focused the main laser pulse at the entrance of a variable-length (0.1-2 mm) gas cell [1, 3]. The plasma density was measured on every shot using a Michelson interferometer and was varied by changing the gas pressure [1, 3]. The electron beam was dispersed in energy with a 0.92 tesla dipole magnet onto a plastic scintillator or a lanex screen and recorded using a PI-MAX intensified CCD camera. Figure 3. 1 shows an overview of the experimental setup.

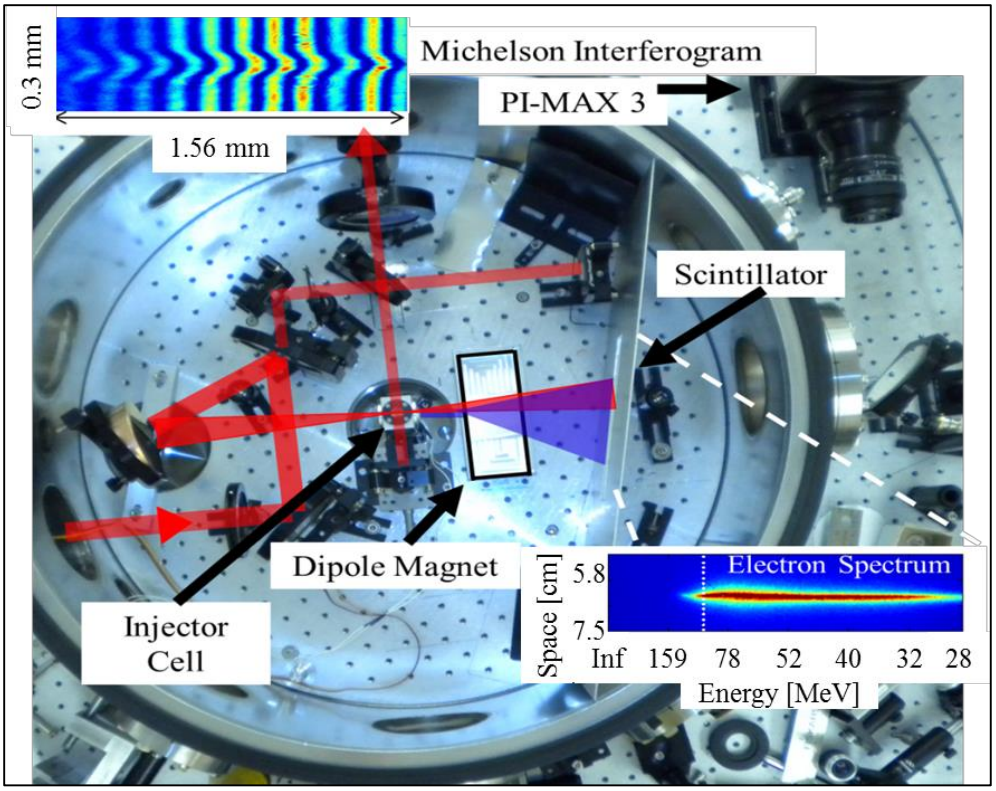

Figure 3. 1: Typical experimental setup. The thick red line shows the main laser pulse being focused by the f/6 OAP system at the entrance of the gas cell. The thin red line shows how a portion of the main pulse transmitted through a turning mirror is used for the Michelson interferometer. A typical interferogram is shown. The electrons are dispersed by the dipole magnet shown in the figure onto a scintillator or a lanex and imaged by a PI-MAX 3 camera. The dipole magnet typically was located 3.2 cm downstream from the gas cell, and the distance from the end of the magnet to the screen was 7.0 cm. A typical measured electron spectrum is also shown.

The plasma source for these LWFA experiments was a self-aligning, variable-length (0.1-2 mm) gas cell that was designed [1, 3] to deliver reproducible, constant-density plasma profiles with short entrance and exit ramps. The main body of the gas cell was machined out of a solid piece of aluminum. There were two side windows in the plane of but orthogonal to the direction of the laser propagation for probing the plasma. These windows are labelled in Figure 3. 2(a) and Figure 3. 2(b). The bottom of the main body connected to the gas delivery system, and the top had a window for aligning as can be seen in Figure 3. 2(a) and Figure 3. 2(b). In the direction of the laser propagation, a plug-type fixture could be inserted into each end. The outer portion of one of

these plugs is labelled on the left side of Figure 3. 2(a), and both are shown in Figure 3. 2(b). By varying the length of the inserted plugs, the gas cell length could be varied from 100 μm to 2 mm as shown in Figure 3. 2(c). The entrance and exit pinholes of the gas cell were drilled in situ by puncturing the faces of the front and rear plugs using the laser pulse at 10 Hz and 100 mJ until the pinholes were cleanly formed. Since they are laser-drilled, the pinhole diameters can be kept as small as 100 μm and typically are between 150 – 300 μm. Though the configuration of the gas cell does not permit direct measurement of the down ramps, because the pinholes have small diameters, the density ramps are expected to be on the order of the pinhole diameter as predicted by Reference [4]. Further, by laser drilling the pinholes in situ, this injector is automatically aligned in the xy plane.

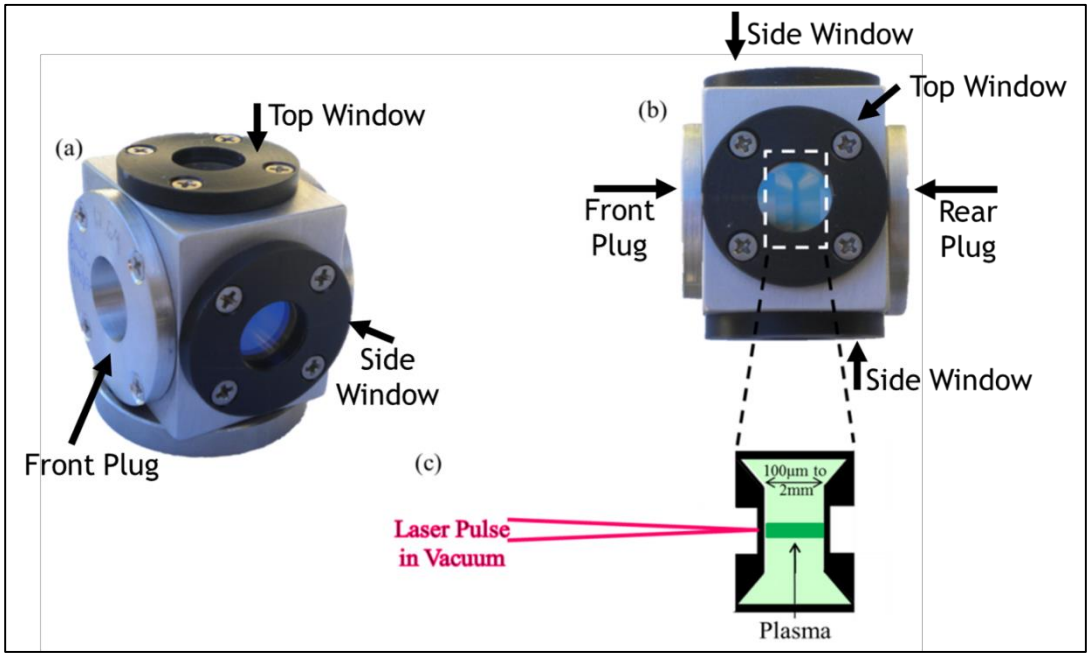

Figure 3. 2: (a) Photograph of gas cell developed at UCLA [3]. (b) Top view of gas cell showing interaction region. (c) Schematic of cross section of interior of gas cell.

The gas cell was filled with a 95% He/5% N_2 neutral gas mixture using a pulsed solenoid valve. The gas mixture was used so that ionization injection could be used to both inject charge

early into the wake and to increase the amount of trapped charge. The measured plasma densities typically ranged from 8 x 10^{18} cm^{-3} to 2.8 x 10^{19} cm^{-3}. Because the fill pressure is expected to be more uniform throughout the gas cell compared to gas jets, which are commonly used in LWFA experiments, the laser-produced plasma is similarly expected to be more uniform, stationary, and reproducible. The two typical density profiles measured from a 1140 μm cell are shown in Figure 3. 3 and highlight both the uniformity and reproducibility of the plasma density in this gas cell. Additionally, the plasma density produced in this gas cell scales linearly with backing pressure as shown in Figure 3. 4, which enables a desired plasma density to be achieved by controlling the fill pressure.

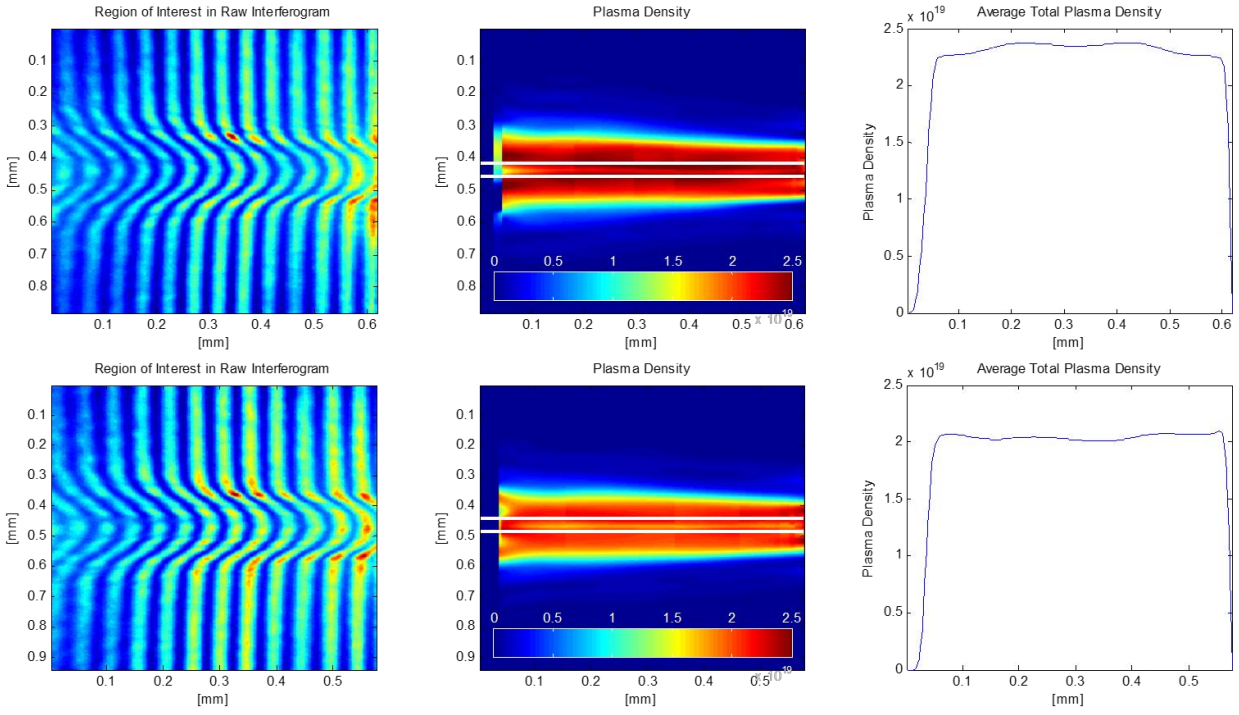

Figure 3. 3: Example density profiles from an 1140 μm gas cell. The plasma density profiles are uniform along the length of the cell. The white lines in the two center images indicate the region over which the average density is calculated. An average is used to compensate for the slight density depression on axis that is caused by the Abel inversion technique [5-7] used to determine the plasma density from the interferogram.

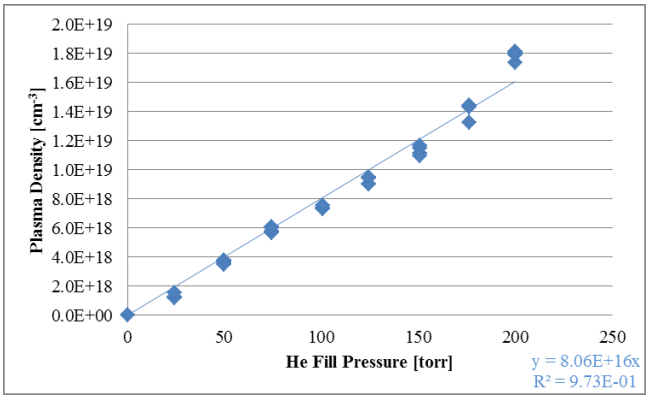

Figure 3. 4: Plot of the plasma density in the gas cell versus a 100% He fill pressure, which shows that the plasma density in the gas cell scales linearly with the backing pressure.

Section 3.2: Curve-Fitting Method for Finding Maximum Electron Energy

The energy of electron beams from an accelerator is typically measured by magnetically dispersing the electron beam onto a detector. Because the magnetic dispersion is highly nonlinear, the lower-energy charge generally experiences higher deflection and is well dispersed on the detector, whereas the higher-energy charge is deflected less and therefore is less dispersed. This small spatial separation leads to a reduced resolution at higher energies and makes it challenging to accurately determine the maximum energy of an electron beam in the 10s to 100s of MeV energy range using a non-imaging but dispersive magnet. The issue of determining the maximum energy of an electron beam is further complicated when that beam has a large transverse size at the detection plane. In such a case, it is difficult to determine whether the signal at high energies on the detector is actually high-energy electrons or if it is an artifact of the transverse size of the beam. We developed a curve fitting method [2] based on asymptotically fitting transverse size contributions to separate the effect of the transverse size of the electron beam at the detector from the energy dispersion, so that the maximum energy of the electron beam could be determined. This curve-fitting method was developed to accurately characterize the ~100 MeV electron beams produced in the gas cells [1, 3] just described in Section 3.1. The method described here was found

to converge on many real data sets and enabled us to determine the maximum energy of an electron beam regardless of its energy spread or its exponentially-decreasing tail.

This method separates out the transverse size contribution by comparing the signal in the dispersed plane to the signal in the transverse (undispersed) plane. In the dispersion plane, the lineout of the electron spectrum has the combined effects of energy dispersion and transverse size. The transverse lineout at a particular energy, however, only shows the effects of the transverse size. Therefore, by comparing the transverse and longitudinal lineouts of the electron spectrum at that particular energy, it is possible to determine if the signal at that point is due to electrons of that energy or if the signal is from the transverse size contribution of lower-energy electrons.

To compare the transverse lineout of the signal at a particular energy to the actual spectrum, the transverse size contribution of the transverse lineout must first be converted into a dispersed signal. This process is best illustrated on an actual electron spectrum. A raw electron spectrum is first linearized as shown in Figure 3.5(a) to correct for the energy dispersion of the spectrometer. Based on the energy scale of this linearized spectrum (Figure 3.5(a)), the maximum electron energy appears to be between 110 MeV and 160 MeV. Therefore, transverse lineouts of the raw spectrum are taken for a series of energies between 110 MeV and 160 MeV. A typical transverse lineout is shown in Figure 3.5(b).

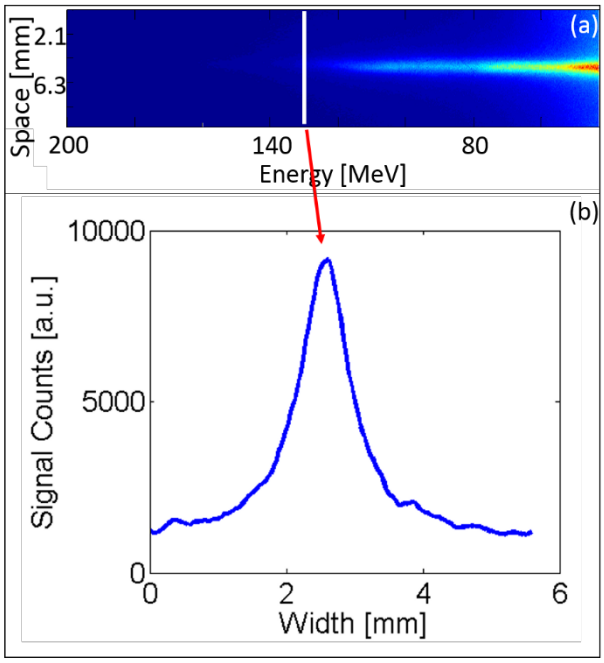

Figure 3. 5: (a) Linearized electron spectrum showing the location of the transverse lineout taken at 130 MeV. (b) Typical raw transverse lineout of the electron spectrum taken at 130 MeV before being rotated and linearized.

Each transverse lineout contains the transverse size contribution from the electrons at the energy where it was taken. Assuming that the transverse size effects are radially symmetric, this transverse lineout also includes the contributions of any lower-energy electrons whose transverse sizes are large enough to overlap the chosen energy. The selected transverse lineouts are rotated 90^0 to orient them in the dispersion plane. They are then linearized using the same process used to linearize the dispersed spectrum. Again, because the transverse lineout has no dispersion effects and therefore only accounts for the transverse size contribution, by rotating it into the dispersion plane and linearizing it, the transverse size contribution is converted into a linearized signal in the dispersion plane. This converted transverse lineout thus only shows the portion of the total signal at a given energy that is in fact due to the transverse size. Each converted transverse lineout can then be compared to the central lineout of the actual dispersed signal as shown in Figure 3.6. In this figure, the solid black curve is the central lineout of the dispersed electron spectrum, and the

blue, green, and red dashed curves are the converted transverse lineouts from 120 MeV, 130 MeV, and 146 MeV, respectively. If the tail of the longitudinal lineout has a greater magnitude than the tail of the converted transverse lineout, then the longitudinal signal cannot be caused by the transverse size of the energy of interest alone. There must be a contribution from higher-energy electrons. However, if the tail of the converted transverse lineout at a given energy has a higher signal, then the longitudinal signal at that energy can be attributed to the transverse size contributions of electrons at energies less than the energy being compared. Therefore, the comparison must be repeated with the transverse lineout at the next lowest energy.

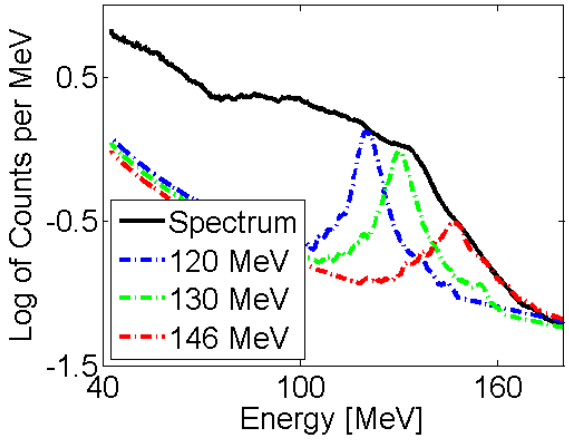

Figure 3. 6: Process of comparing the rotated and linearized transverse lineouts (dashed lines) against the central lineout of the electron spectrum (solid black line). The converted transverse lineout at 146 MeV (red dashed curve) is asymptotic with the central lineout; therefore the maximum electron energy is 146 MeV.

To illustrate this comparison, in Figure 3. 6, the tail of the blue curve (the transverse lineout at 120 MeV) is below the dispersed signal. Therefore, 120 MeV is not the maximum measured electron energy; there must be a contribution to the measured electron spectrum from higher-energy electrons. The tail of the red curve falls on the dispersed lineout. Therefore, the tail of the actual dispersed signal can be attributed to the transverse size contribution of the 146 MeV

electrons. Therefore, 146 MeV is the maximum energy of this electron spectrum. Note that this method does not account for errors in the measurement of the maximum electron energy due to the electron bunch leaving the plasma at an angle relative to the laser axis. However, if this method is used with a two-screen spectrometer [8, 9], both the transverse size and the exit angle of the electron bunch can be taken into account when calculating the maximum electron energy.

Conclusion

In this chapter, we discussed the laser and plasma parameters used in our experimental studies of DLA-assisted LWFA. We included a detailed analysis of the variable-length gas cells designed to provide reproducible, constant-density plasma profiles with short entrance and exit ramps. Finally, we detailed a curve-fitting method for determining the maximum energy gain of a dispersed electron beam with continuous energy spread regardless of its transverse size. In the next chapter, we show how this method was applied to experimental work at UCLA to produce initial results that suggest that DLA is an additional acceleration mechanism at work in LWFA when the laser pulse overlaps the trapped electrons.

Ch. 3 References

[1] J. L. Shaw et al., *Proceedings of the Advanced Accelerator Concepts Workshop* **315**, 315-320 (2013).

[2] J. L. Shaw et al. *Proceedings of the North American Particle Accelerator Conference*, MOPAC45 (2013).

[3] J. L. Shaw, *Characterization of Sub-millimeter-scale Gas Cells as Possible Injectors for Staged Laser Wakefield Acceleration*, Master's thesis, University of California Los Angeles (2013).

[4] F. Sharipov, J. Fluid Mech. **518**, 35-60 (2004).

[5] T. Mitsuo et al., J. Opt. Soc. Am. **7**, 156-160 (1982).

[6] K. Bockasten, J. Opt. Soc. Am. **51**, 943-947 (1961).

[7] M. Kalal and K. A. Nugent. Appl Opt. **27**, 1956-1959 (1988).

[8] B. B. Pollock et al., *Proceedings of the Particle Accelerator Conference*, WE6RFP101 (2009).

[9] C. E. Clayton et al., Phys. Rev. Lett. **105** (2010) 105003.

Ch. 4: Initial Results

Introduction

The goal of the experimental work completed for this dissertation was to demonstrate a definitive, observable signature of the DLA of electrons in a LWFA operating in the quasi-blowout regime. As shown through PIC simulations in Chapter 2, the DLA process can add a significant amount of energy to the highest-energy electrons, and the fraction of the total energy gained by the electrons from DLA can increase as the plasma density is increased for a given laser pulse length (i.e. as T_p increases). Therefore, our initial experimental effort was focused on showing an increase in the maximum electron energy with increasing values of T_p as a definitive experimental signature of DLA in LWFA. Though these experimental goals would evolve as our understanding of DLA-assisted LWFA evolved, in this chapter we show the initial experimental results. Although the results were tantalizing, we will also show that they were not definitive proof of DLA in LWFA and therefore led to a new direction of the experimental efforts to obtain a direct, observable signature of the DLA of electrons in a LWFA.

Section 4.1: Initial Experimental Results

The initial experiment results were collected on the system described in Section 3.1 for plasma densities between 8×10^{18} cm^{-3} and 2.5×10^{19} cm^{-3} using gas cell lengths of 430, 680, 710, and 1140 μm. These cells were longer than the ideal dephasing length given by Equation 1.5 for a matched laser pulse at a given density but shorter than the pump depletion length [1]. The associated T_p values as given by Equation 1.1 varied between 0.8 and 1.6. We note here that for the plasma densities used in these initial experiments, the laser spot size was not matched to the plasma density and therefore some spot size oscillations and self-focusing were to be expected.

The measured, linearized electron spectra have a continuous energy spread (albeit with some peaks), which is characteristic of ionization injection [2, 3] and exhibit a high-energy tail. The curve-fitting method described in Section 3.2 was applied to these electron spectra to determine the maximum energy of the electron beam. The maximum measured energy E_{max} was then compared to the theoretical maximum energy gain for the peak of a bunch produced by a LWFA operating in the nonlinear blowout regime as given by Equation 1.6.

Figure 4.1 shows electron energy spectra produced in the 1140 μm gas cell at three plasma densities and slightly different a_0s. For all three plasma densities, E_{max} of the electron spectra exceeds E_{theory} given by Equation 1.6. Furthermore, even the energies of the highest-energy peaks (marked by arrows in Figure 4.1) exceed E_{theory}.

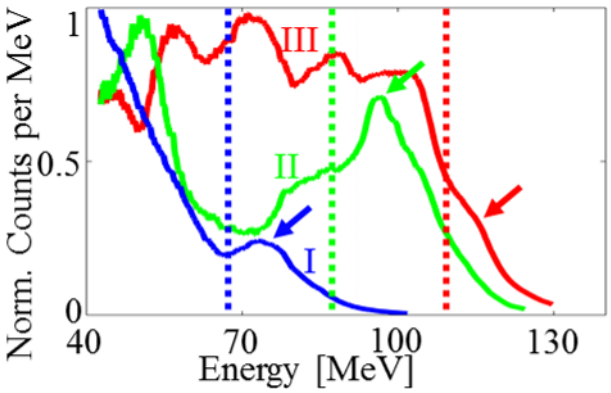

Figure 4. 1: Experimental electron energy spectra from the 1140 μm gas cell. The dashed lines indicate the values of E_{theory} calculated for each shot using Equation 1.6. The arrows mark the highest-energy peaks in the substructure of each spectrum. The parameters for each spectrum are: (I) $n_e = 1.3 \times 10^{19}$ cm^{-3}, $a_0 = 1.6$, $E_{max} = 93 \pm 1$ MeV, $E_{theory} = 68$ MeV; (II) $n_e = 1.1 \times 10^{19}$ cm^{-3}, $a_0 = 1.7$, $E_{max} = 112 \pm 2$ MeV, $E_{theory} = 88$ MeV; and (III) $n_e = 1.0 \times 10^{19}$ cm^{-3}, $a_0 = 2.0$, $E_{max} = 113 \pm 1$ MeV, $E_{theory} = 110$ MeV.

In Figure 4.2(a), E_{max} for each experimental spectrum is plotted versus n_e for different gas cell lengths. The dashed and solid black curves show E_{theory} calculated using Equation 1.6 for the highest ($a_0 = 2.2$) and lowest ($a_0 = 1.6$) vacuum a_0s used in this experiment, respectively. These theoretical curves illustrate the expected $1/n_e$ scaling predicted by Equation 1.6 for the electron

energy gain due to the wakefield alone. However, the experimental data points show that the measured E_{max} does not follow this scaling, which has previously been observed in several self-trapping experiments using gas jets [4-6]. Furthermore, the majority of the data points in Figure 4. 2(a) fall above these curves with the difference becoming larger at higher densities. To quantify this point, in Figure 4. 2(b) we have plotted the data shown in Figure 4.2(a) as $(E_{max} - E_{theory})/E_{theory}$ in percent against the dimensionless pulse length parameter T_p, where again $T_p > 1$ indicates a significant overlap between the transverse laser field and the trapped electrons.

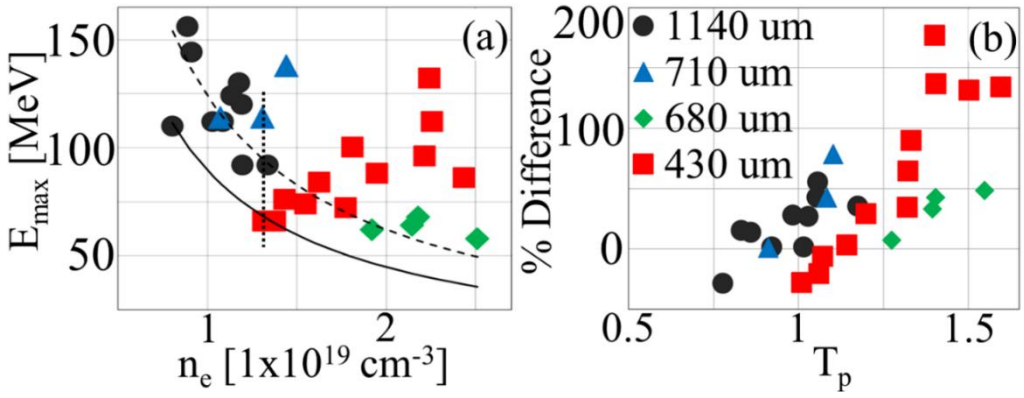

Figure 4. 2: (a) Plot of E_{max} versus the measured n_e for four different gas cells with lengths greater than L_d. The black curves are values of E_{theory} given by Equation 1.6 calculated for vacuum $a_0 = 2.2$ (dashed) and $a_0 = 1.6$ (solid). The vertical dotted line marks the experimental points that are compared to simulations in Figure 4. 3. (b) Plot of the percent difference between E_{max} and E_{theory} versus normalized parameter T_p.

At the lowest T_p values of ~ 0.8 (n_e = 8 x 10^{18} cm^{-3}), the electric field from the falling intensity of the laser pulse overlaps with the electrons, but the observed E_{max} is close to the expected value given by Equation 1.6, which assumes only wakefield acceleration. However, the simulations [7] shown in Section 2.2 revealed that even at this low density, there is some contribution from the transverse laser field to the total observed energy gain, which suggests that in the experiment, the energy gain due to the wakefield does not reach that predicted by Equation 1.6. In other words, the apparent agreement between the theoretical value and the experimental value at this plasma density is a coincidence. Also, it should be noted that even in the absence of

DLA, the location of electron trapping is different for ionization injection than for self-trapping, and therefore different energy gains may be expected.

For larger values of T_p (which correspond to higher plasma densities), the spectra have maximum measured energies clearly greater than those predicted by the 3D nonlinear wakefield theory [1]. For instance, for the 430 μm gas cell (red squares in Figure 4.2), these deviations are quite large and reach 180% of the theoretical value for a plasma density of 2.3×10^{19} cm^{-3}. We also found that at these high densities, when the gas cell length was further increased to 680 μm (green diamonds), the maximum energies of the electrons were lower than those taken with the 430 μm cell for the same high plasma densities (i.e. $> 2 \times 10^{19}$ cm^{-3}). At these high densities, the LWFA is transitioning from the forced LWFA regime [8] to a self-modulated regime [9, 10], and therefore the length scaling of the energy gain might be somewhat different. The general trend of E_{max} increasing with T_p seen in Figure 4.2 suggests that there may be an additional acceleration mechanism contributing to the maximum energy of the produced electron beams.

To explore this possibility, we have carried out an extensive set of 2D PIC simulations using OSIRIS with a moving window and the ADK ionization package to unravel the relative contributions of the various acceleration mechanisms to the total energy gain. As an illustration, here we will describe the results of three simulations that modeled the parameters of three experimental shots taken on different length gas cells but at the same plasma density $n_e = 1.3 \times 10^{19}$ cm^{-3} such that $T_p = 1.00 – 1.16$ (these points are marked by the vertical dotted line in Figure 4.2(a)). In each simulation, the neutral gas was comprised of 99.9% He and 0.1% N_2 and was laser-ionized. For all three cases, the 45-fs laser pulse was linearly polarized and focused half way up the density entrance ramp. The simulations were run once to identify and tag the 15 highest-energy electrons and subsequently re-run to track the momenta and trajectories of those electrons.

To show the contribution of DLA to the total electron energy in these simulations, the relative contributions to the energy gain of these 15 electrons due to LWFA and DLA was calculated using Equations 2.1 and 2.2, respectively. The relative importance of DLA to the maximum electron energy can be clearly observed by comparing the total energy gain (black curves) and the DLA contribution (blue curves) in Figure 4. 3(a), (b), and (c). We see that for the 430 μm gas cell (Figure 4. 3(a)), the total energy gain can be accounted for by the work done by DLA. The total electron energy is slightly below the energy gain due to DLA because the electrons are propagating in the decelerating field of the wake and therefore are returning some energy gained from DLA to the wake. As the inset in Figure 3(a) shows, at the exit of the plasma, these electrons are bunched at twice per laser wavelength as is expected from DLA [11, 12].

As the cell length is increased to 710 μm (Figure 4. 3(b)), LWFA (red curve) begins to make a contribution. In the case of the 1140 μm cell (Figure 4. 3(c)), the wakefield contributes about half of the total energy gained by the electrons. In other words, for $T_p \sim 1$, these simulations suggest that DLA is at least equally as important as LWFA as an acceleration mechanism. Although it appears as if no electrons begin to gain energy until well into the plateau region of the simulated plasma, note that Figure 4. 3 shows the origin of only the highest-energy electrons at the end of the simulation. Other electrons were trapped earlier on and interacted with $\mathbf{E}_{\parallel}$ and $\mathbf{E}_{\perp}$ in a similar manner while gaining and losing energy. For all three cases shown in Figure 4. 3(a)-(c), the total energy gain from the simulations is in reasonably good agreement with E_{max} observed in experiment (red dots).

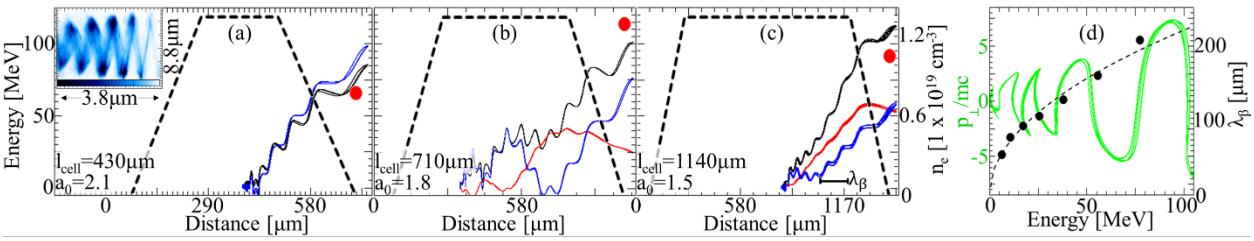

Figure 4. 3: (a)-(c) DLA contributions (blue curves) and wakefield contributions (red curves) to the total energy gain (solid black curves) of electrons for the highest-energy electrons at the end of the simulation for three different gas cell lengths. The simulation parameters were close to the parameters of the three experimental points marked by the dotted line in Figure 4. 2(a). The black dashed curve marks the plasma profile. The red dots mark E_{max} in the experiment. The simulation parameters for each frame are: c/ω_p = 1.46 μm; simulation box size = 48 x 54 c/ω_p = 70.6 x 79.4 μm; grid = 2608 x 356; transverse resolution $k_p dx_\perp$=0.15; longitudinal resolution $k_0 dx_\parallel$ =0.21; and 16 particles per cell. (inset in (a)) Bunching of all the trapped electrons on a laser-wavelength scale. Linear color scale indicates charge density from 0 to 1.9 x 10^7 cm^{-2}. (d) Measured wavelengths of the oscillations in the blue curve in (c) (black dots) and theoretical betatron wavelength (black dashed curve) versus electron energy. The theoretical curve was calculated assuming 70% blowout of the plasma electrons from the laser axis, which is approximately the degree of blowout seen in the simulation. The green curve is the plot of the transverse momentum of the electrons versus their energy.

Because DLA arises from the betatron motion of the electrons in the ion column, a signature of that motion is reflected in the DLA contribution to the total energy gain. This signature is shown in Figure 4. 3(d), where the wavelengths of the modulations in the blue curve in Figure 4. 3(c) are plotted (black dots) with the theoretical betatron wavelength given by Equation 2.4 (black dashed curve) as a function of the total energy. The agreement between the two is very good. A similar trend was observed for Figure 4. 3(a) and 3(b) as well. Furthermore, the transverse momentum $\mathbf{p}_\perp$ (green curve) gained by the electrons in the laser field is continuously converted into longitudinal momentum as expected in DLA (Figure 4. 3(d)). Together with the bunching on a laser-wavelength scale, these observations strongly suggest that it is indeed DLA that significantly enhances the energy gain of the electrons.

By measuring the maximum electron energies over a range of plasma densities for a fixed laser pulse length, we showed strong evidence that DLA can be a major contributor to the maximum electron energy and that the energy gain due to DLA can exceed that due to LWFA for

certain laser and plasma parameters. However, due to a limitation in the curve-fitting method used to determine the maximum electron energy and to utilizing 2D simulations, these results were not definitive proof of DLA in LWFA. These two limitations will be explained next.

Section 4.2: Limitations on the Initial Experimental Results

Though these early experimental results strongly suggested that a second acceleration mechanism was at play, two aspects of the analysis left room to interpret the data in a different way. First, the main assumption of the curve-fitting method used to determine the maximum energy of the electron beams may not be valid if DLA is present. As discussed in Section 3.2, the key assumption of the curve-fitting method is that the divergence of the produced electron beams is radially symmetric (i.e. the divergence is the same parallel and orthogonal to the direction of dispersion in the magnetic spectrometer). However, this assumption was not tested in our initial experimental work, and two factors could lead to asymmetries in the divergence of the produced electron beams. First, ionization injection can produce slightly-asymmetric electrons beams with the divergence being larger in the direction of the laser polarization [13, 14]. Second, if DLA is indeed an additional acceleration mechanism, the electron beams would be expected to have larger divergence in the direction of the laser polarization because the transverse motion of the electrons is coupled to the transverse laser field. Either of these scenarios could lead to an asymmetry in the divergence of the produced electron beams in the plane of the laser polarization relative to the orthogonal plane, and because the electrons were dispersed in the direction of the laser polarization, it means that the curve-fitting method may over-estimate the maximum energy of the produced electron beams. If this asymmetry in the divergence is taken into account, it could be possible that the maximum electron energies would not exceed E_{theory} given by Equation 1.6.

A second process could also void our finding that the measured maximum electron energies exceed $E_{theory.}$ In the initial analysis, E_{theory} was calculated using the vacuum a_0 value for the laser system. However, because the laser parameters are not matched to the plasma density, the laser is expected to evolve as it propagates through the plasma. As it evolves, the laser will self-focus towards the matched spot size, which ranges from 2.7 to 5.5 μm for the plasma densities and laser powers used in the initial experimental results present above. This self-focusing could lead to a_0 enhancements up to an a_0 value ~ 5 in the LWFA. These enhancements could lead to the self-trapping of electrons in the wake. A larger a_0 will drive a wake with a higher acceleration gradient [1], which can cause both the self-trapped and ionization-injected electrons to gain energies that are higher than the expected energies from the LWFA mechanism alone. Additionally, an a_0 enhancement could also increase the DLA contribution to the electron energy. Therefore, to accurately compare against E_{theory}, the evolution of a_0 over the length of the gas cell would need to be known. The OSIRIS simulations used to model these initial experiments were 2D, which limits their ability to accurately model the self-focusing of the drive laser pulse. Without knowledge of the possible increase in a_0 due to laser evolution, the enhanced energy gains that we measured could simply be attributed to self-focusing.

Conclusion

In conclusion, we were able to produce high-energy electron beams with modest laser parameters. The curve-fitting method described in Chapter 3 was utilized to determine the maximum energies of those electron beams, and those measured values were compared to the maximum theoretical electron energies expected for LWFA. This comparison revealed that the maximum measured electron energies often exceeded the energies predicted for LWFA and that this deviation increased with plasma density. This finding suggested that an additional

acceleration mechanism was at play, and 2D OSIRIS simulations showed that that mechanism was DLA. However, the key assumption that the electrons beam have a radially-symmetric divergence used in the curve-fitting method may not be accurate in the case of this experiment because both the ionization injection mechanism and DLA are expected to increase the electron divergence in the direction of the laser polarization. Additionally, because the degree to which the laser self-focuses is not known in the experiment, the comparison to the maximum theoretical electron energy calculated using the vacuum value of a_0 may not be valid.

Despite these two limitations, these initial experimental findings pointed towards a path in both simulation and experiment to definitively show that DLA was indeed an additional acceleration mechanism in a nonlinear LWFA operating in a regime where the laser pulse overlaps the trapped electrons. The next chapter addresses this next step in experimental and simulation work where we fully characterized the structure of the electron beam in the direction transverse to the laser polarization and use the resulting spectral features to demonstrate the presence of DLA in LWFA.

Ch. 4 References

[1] W. Lu et al., Phys Rev. Spec. Top. – Accel. Beams **10**, 061301 (2007).

[2] A. Pak et al., Phys. Rev. Lett. **104**, 025003 (2010).

[3] C. E. Clayton et al., Phys. Rev. Lett. **105**, 105003 (2010).

[4] D. H. Froula et al., Phys. Rev. Lett. **103**, 215006 (2009).

[5] S. Kneip et al., Phys. Rev. Lett. **103**, 035002 (2009).

[6] S. P. D. Mangles et al., IEEE Trans. Plasma Sci. **36**, 1715-1721 (2008).

[7] J. L. Shaw et al., Plasma Phys. Contr. F. **56**, 084006 (2014).

[8] V. Malka et al., Science **298**, 598 (2002).

[9] E. Esarey et al., Phys. Rev. Lett. **72**, 2887-2890 (1994).

[10] A. Modena et al., Nature **377**, 6550 (1995).

[11] A. Pukhov et al., Phys. Plasmas **6**, 2847 (1999).

[12] N. Lemos et al., *Proceedings of the 2014 Advanced Accelerator Concepts Workshop. http://arxiv.org/abs/1502.07764v1*.

[13] W. P. Leemans et al., Phys. Rev. Lett. **68**, 3 (1992).

[14] A. Doepp et al. (2015) *http://arxiv.org/pdf/1509.08629.pdf*.

Ch. 5: Experimental Results

Introduction

In the previous chapter, we explained how the scaling of the maximum electron energy as a function of T_p suggested that DLA was occurring simultaneously with LWFA in the range of plasma densities used in the experiment. However, the results were not conclusive because the ellipticity of the divergence of the electron beams was not taken into account in the curve-fitting method used to determine the maximum energy of the dispersed electron beams. Additionally, the effect of self-focusing on the maximum electron energy needed to be determined.

In this Chapter, we show definitive experimental evidence of DLA in nonlinear LWFAs where the laser pulse overlaps the trapped electrons. We first demonstrate that the undispersed electron beams are indeed elliptical in shape as might be expected in a DLA-assisted LWFA experiment. We then show that the transverse structure of the dispersed electron beams exhibits characteristic features that are indicative of DLA as an additional acceleration mechanism when $T_p \sim 1$. These characteristic spectral features are reproduced in 3D OSIRIS simulations and are indeed attributed to DLA. These 3D simulations are also used to show that although the laser pulse indeed self-focuses at the plasma densities used in the experiment, DLA is still present and contributes to the energies gained by the highest-energy electrons.

Section 5.1: Divergence of Produced Electron Beams

Under the laser-plasma parameters described in Chapter 4, the measured divergence of undispersed electron beams emanating from the plasma shows ellipticity that is correlated to the polarization of the laser pulse. The white ellipses in Figure 5. 1(a) are fits to the 50% contour of the undispersed electron beams from 10 consecutive shots where the laser had horizontal, linear

polarization and a vacuum a_0 of ~1.5. The plasma density was ~1.7 x 10^{19} cm^{-3}, which yields a T_p value of ~1.3, and the gas cell length was 900 μm. The fits show a strong ellipticity in the direction of the laser polarization with an average measured HWHM divergence of 12.2 mrad. In contrast, the average measured HWHM divergence in the perpendicular direction was 5.6 mrad. The direction of the linear polarization of the drive laser was then rotated 90^0 using a thin (1 mm) quartz half waveplate for high-laser-energy applications. The ellipticity of the undispersed electron beams rotated with the laser polarization as shown in Figure 5. 1(b), which indicates that the trapped electrons' transverse momentum is being enhanced in the polarization plane. With the vertical laser polarization, the average measured HWHM divergence in the direction of the laser polarization was 13.0 mrad, and the average measured HWHM divergence in the perpendicular direction was 6.5 mrad.

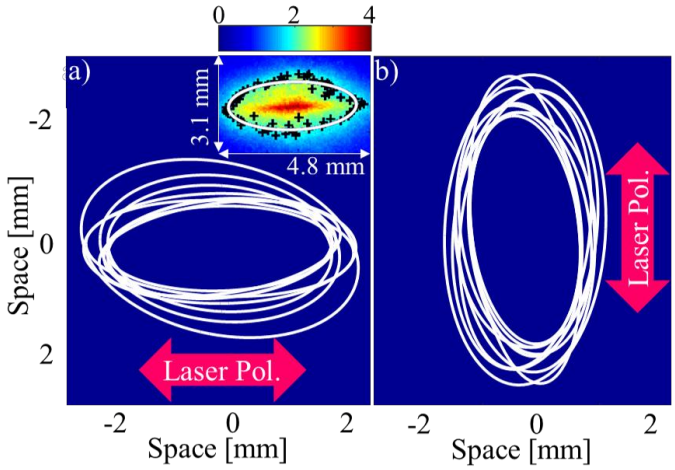

Figure 5. 1: (a, b) Fits (white ellipses) to the 50% contour of undispersed electron beams from a series of 9 and 10, respectively, consecutive laser shots when using horizontal and vertical, respectively, linear laser polarization. (Inset) Typical undispersed electron beam from data shown in (a) with 50% contour points marked by the black crosses and the fit to that point marked by the white ellipse.

Although DLA preferentially increases the divergence of the electron beam in the plane of the laser polarization, the observed ellipticity in the divergence of the undispersed electron beams

in Figure 5.1 in itself is not proof that DLA is present in the LWFA. Even if the laser pulse does not overlap the trapped electrons, the tunnel ionization process can give electrons an initial asymmetry in momentum when the electrons escape the laser pulse to become trapped in the plasma wave [1]. At the plasma density used here, T_p is ~1.3, and the ionization-injected electrons do not escape the laser pulse and acquire initial momentum in the laser polarization direction until exiting the plasma where the laser diffracts away. The maximum transverse momentum from this interaction can be estimated. From the single particle equations of motion of an electron in an intense laser field, it is possible to find two constants of motion for an electron born at rest in a field-free region

$$\gamma - \overline{p_z} = 1 \tag{5.1}$$

$$\overline{p_x} - \overline{a_{0x}} = 0 \tag{5.2}$$

Here, $\bar{p}$ is the normalized momentum ($p/mc \rightarrow \bar{p}$) and $\overline{a_0}$ is the normalized vector potential ($eA/mc^2 \rightarrow \overline{a_0}$). In normalized units, the Lorentz factor of the electron can be written as

$$\gamma = \sqrt{1 + \overline{p_x}^2 + \overline{p_y}^2 + \overline{p_z}^2} \tag{5.3}$$

For a linearly-polarized laser pulse, $\overline{p_y} \rightarrow 0$. Equation 5.1 can be set equal to Equation 5.3 to solve for $\overline{p_z}$. The result is

$$\overline{p_z} = \frac{\overline{p_x}^2}{2} = \frac{\overline{a_{0x}}^2}{2} \tag{5.4}$$

The value of $\overline{p_z}$ from Equation 5.4 can be substituted back into Equation 5.1 to relate γ to the normalized vector potential

$$\gamma = 1 + \frac{\overline{a_{0x}}^2}{2} \tag{5.5}$$

For the seventh electron to be ionized from 99% of the nitrogen atoms in the LWFA, the laser a_0 must self-focus to a value of 2.5. The threshold for the ionization of the seventh electron is an a_0 of 2.3, so that electron will be ionized over a range of phases ϕ from 0 to 0.44 for an electric field of the form $E_0\cos\phi$. Therefore, the range of a_0 values seen by the electrons as they are ionized will range from 0 to 1.08 for a normalized vector potential of the form $a_0\sin\phi$. This maximum a_0 value can be substituted into Equation 5.5 to find the maximum transverse momentum of the electrons due to ionization, which ranges from $\gamma_\perp = 1$ to 1.6 for the possible a_0 values. This transverse momentum due to ionization would give a divergence $\gamma_\perp/\gamma_\parallel = 1.58/240$ of ~ 6.6 mrad in the direction of laser polarization.

3D OSIRIS simulations were carried out at a plasma density of 8×10^{18} cm^{-3} and with a laser a_0 of 2.1 but with two different laser pulse lengths of 25 fs and 45 fs such that T_p was 0.4 and 0.8, respectively. In these simulations, the self-focusing of the laser increased the value of a_0 to over 2.8, i.e. well above the threshold for the ionization of the last nitrogen electron. When the laser intensity exceeds 2.5, 99% of the nitrogen is fully ionized as explained above. In the $T_p = 0.4$ case, the inner-shell nitrogen electrons were ionized within the laser pulse and then escaped the laser to become trapped in the back of the wake, which causes the initial transverse momentum that they gain from the laser to become apparent. In this case, the projection of the accelerated electrons on a screen (Figure 5.2(a)) shows an elliptical beam with an RMS divergence of 8.6 mrad along the major axis. In the case of $T_p = 0.8$, the ionized electrons remain within the laser field

and gain energy from both LWFA and DLA. These electrons also show an elliptical beam when projected on a screen (Figure 5.2(b)); its RMS divergence along the major axis is 24.8 mrad. Although both simulations produce an elliptical beam, the observation of increased divergence in the $T_p = 0.8$ is qualitatively consistent with expectations if DLA is present as an additional acceleration mechanism. As discussed in Chapter 2, if DLA contributes significantly to the energy of the highest-energy electrons, those electrons have increased transverse momentum in the direction of the laser polarization and therefore these electrons may populate the outer contours of the major axis of the ellipse.

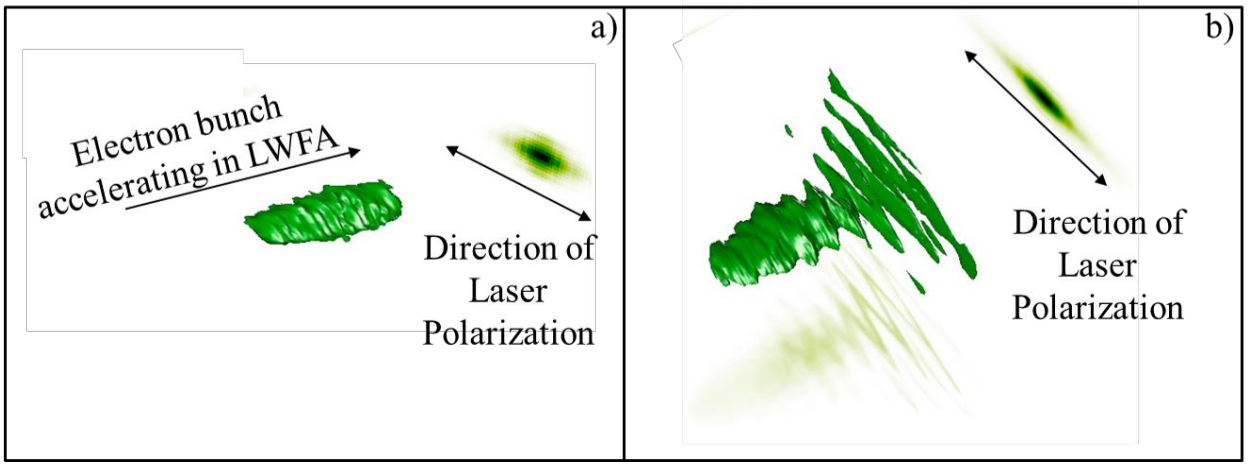

Figure 5. 2: Contour plot of electron bunch propagating in a 3D OSIRIS simulation (left) and projection of that electron bunch on a screen (right) for (a) a $T_p = 0.4$ simulation and (b) a $T_p = 0.8$ simulation. Parameters for these simulations were: $a_0 = 2.1$, $\lambda_0 = 815$ nm, $w_0 = 6.7$ µm, $n_e = 8 \times 10^{18}$ cm^{-3}, plasma length = 1 mm with 100 µm up- and downramps.

Section 5.2: Maximum Electron Energy Scaling Corrected for Divergence

With this measurement of the asymmetry of the divergence of the produced electron beams, one limitation of the finding presented in Figure 4.2 can be addressed. In the initial results shown in Figure 4.2(a), the maximum electron energy E_{max} does not scale as $1/n_e$ as expected for a system where the wakefield is the only source of acceleration. Additionally, Figure 4.2(b) showed that

the percent difference between E_{max} and E_{theory} (calculated using Equation 1.6) scales approximately linearly with T_p. However, as explained in Section 4.2, this result is not direct proof that DLA is active in the experiment partly because the assumption of the curve-fitting method that the divergence is radially symmetric would not be valid if DLA is present in a LWFA and partly because there is the possibility of a density-dependent increase in the a_0 of the laser pulse due to self-focusing. We can correct for the first of these two factors. As shown in Figure 5.1, the measured divergence of the undispersed electron beam is elongated in the direction of the laser polarization. This measurement can be used to correct the assumption of the curve-fitting method.

To briefly revisit the curve-fitting method that was fully described in Section 3.2, the effect of the transverse size of the electron beam at the detector was separated from the energy dispersion by taking the transverse lineout at a given energy, linearizing that lineout to account for dispersion, and then comparing that lineout to the measured signal in the dispersion plane. While this process assumes that the electron beam has a radially-symmetric divergence, the measurement of the undispersed electron beams in Figure 5.1 shows that assumption is not valid in our system. Rather, the elliptical fits to the divergence of the undispersed electron beams show that the ratio of the semi-major axis to the semi-minor axis is ~ 2 for these laser and plasma parameters. Therefore, the curve-fitting method can be modified to account for this elliptical divergence by doubling the width of the transverse size contribution at each energy. After this correction, the modified lineout can then be rotated into the dispersion plane, linearized, and compared to the measured signal in the dispersed plane as before.

Using the curve-fitting method corrected for the elliptical divergence of the electron beams, the electron beams used to generate Figure 4.2 were re-analyzed to find their maximum energies. Figure 5.3(a) shows that this correction does reduce the maximum electron energies (filled data

points) for most of the data points. Despite this reduction, the maximum electron energies still do not follow the $1/n_e$ scaling expected if LWFA was the only acceleration mechanism. Rather, at higher plasma densities, the maximum electron energy still increases with n_e. In Figure 5.3(b), the percent difference is shown for the corrected maximum electron energies. The values of those percent differences have decreased slightly, but there is still a clear trend that the percent difference increases approximately linearly with the degree of overlap between the laser and the trapped electrons. Unfortunately this correction for the ellipticity still does not address the issue of laser pulse self-focusing. There is also the issue of the self-injection of electrons as the plasma density is increased particularly if laser self-focusing is occurring. We therefore concentrated on one value of plasma density (T_p) and then looked for a definite signature of DLA contribution to the energy gained by the electrons while ruling out any self-injection of electrons using 3D PIC code simulations.

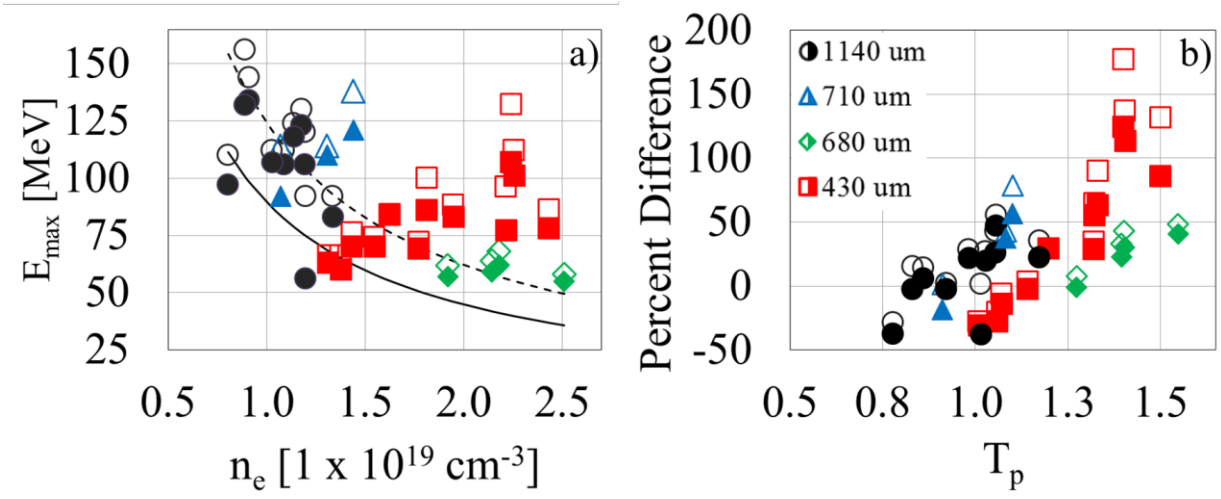

Figure 5. 3: (a) Plot of E_{max} versus the measured n_e for four different gas cells. The black curves are values of E_{theory} given by Equation 1.6 calculated for vacuum $a_0 = 2.2$ (dashed) and $a_0 = 1.6$ (solid). (b) Plot of the percent difference between E_{max} and E_{theory} versus normalized parameter T_p. The unfilled points show the original measurement where the curve-fitting method was used assuming that the divergence of the electron beam was radially symmetric. The filled points show the corrected measurement where the elliptical divergence was taken into account.

Section 5.3: Characteristic Spectral Features of DLA

Figure 5. 4 shows two examples of the experimental electron spectra when the electrons were dispersed in the (a) same and the (b) orthogonal plane of the laser polarization for similar experimental parameters. When dispersed in the direction of the laser polarization, the measured electron beam spectra exhibited a narrower divergence than when it was dispersed orthogonal to the direction of the laser polarization. An example of the former is shown in Figure 5. 4(a), where the electron beam has an average measured HWHM divergence of 4.3 mrad for electron energies greater than 40 MeV. The continuous energy spread is characteristic of ionization injection [2, 3]. However, when the electron beams were dispersed perpendicular to the laser polarization, they had a much larger divergence and additionally split at the highest electron energies resulting in a forked structure. This behavior of the dispersed electron beam is shown in Figure 5. 4(b), where the average divergence increased to 11.8 mrad and the forked structure is clearly visible above 90 MeV. The divergence was calculated using the HWHM for electron energies below 90 MeV and using the fork centroid for energies above 90 MeV, which is where the fork structure begins. Such a fork structure has been observed in experimental electron spectra for plasma densities between 1.1-1.5 x 10^{19} cm^{-3} (T_p = 1.0 - 1.3). The transverse shape (Figure 5. 4(c)) of the spectrum clearly transitions from a center-peaked distribution to the forked structure. In the center-peaked distribution, the electrons gain the majority of their energy from LWFA and can originate from the first and subsequent buckets, in which the laser does not overlap the electrons. The electrons in the forked region of the spectrum originate in the first bucket of the wake and gain a majority of their energy via DLA, as we will show next.

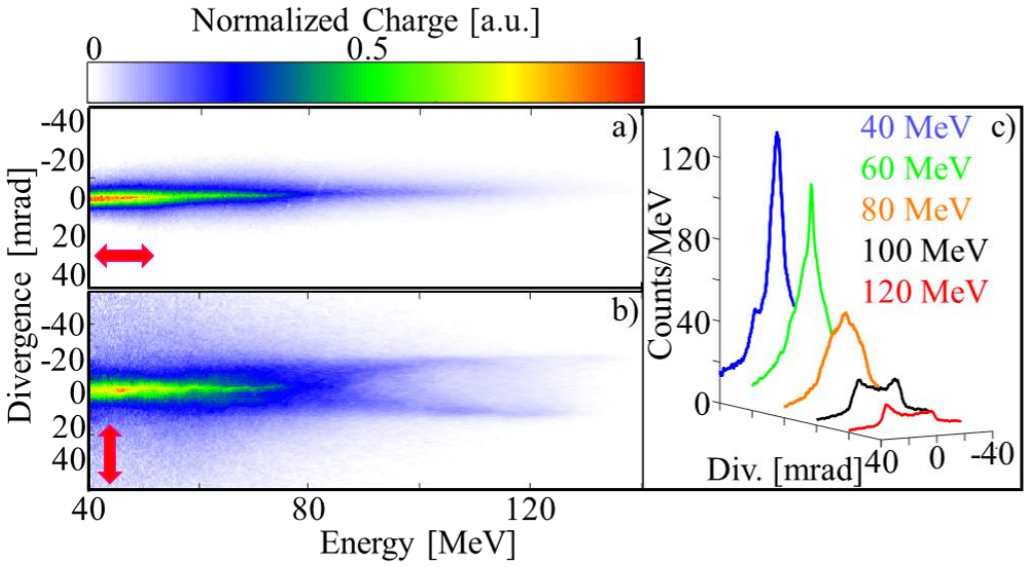

Figure 5. 4: (a,b) Experimental electron spectra dispersed parallel and perpendicular, respectively, to the laser polarization (red arrows). The experimental parameters for the shot shown in (a) and (b) are: gas cell length = 800 and 900 µm, n_e = 1.7 x 10^{19} and 1.4 x 10^{19} cm^{-3}, a_0 = 2.0 and 1.9, and T_p = 1.1 and 1.1, respectively. (c) Transverse lineouts of (b) at 20 MeV intervals.

Section 5.4: Simulations of Characteristic Spectral Features

We have carried out 3D OSIRIS simulations to interpret these observed features. These simulations modeled the above experimental parameters and employed particle tracking to elucidate the roles of LWFA and DLA to the energy gain of the electrons in this experimental regime. We again used the code OSIRIS with a moving window and the ADK ionization package. The grid was 1814 x 320 x 320 with 2 x 2 x 2 particles per cell and $k_0\Delta z$ = 0.209 and $k_p\Delta x,\Delta y$ = 0.120. The resulting normalized time step was 0.01877. The laser in this simulation was linearly polarized with a central wavelength of 815 nm, a pulse length of 45 fs FWHM, and a focused spot size of 6.7 µm. The laser was focused to an a_0 of 2.03 halfway up a 100-µm density upramp and then propagated through a 430-µm constant-density region before exiting through a 150-µm density downramp. The laser ionized an initially-neutral gas comprised of 99.9% He and 0.1% N_2 to produce a plasma density of 1.43 x 10^{19} cm^{-3}.

The laser self-focused [4] to a peak a_0 value of 4.0 at a distance of 20 μm into the constant-density region of the plasma as seen in Figure 5.5. Its a_0 value then fell approximately linearly to a value of 2.9 at the exit of the constant-density region of the plasma. Despite this evolution, the self-trapping of the He electrons in the simulation was negligible compared to the trapping due to ionization injection as shown in Figure 5. 6.

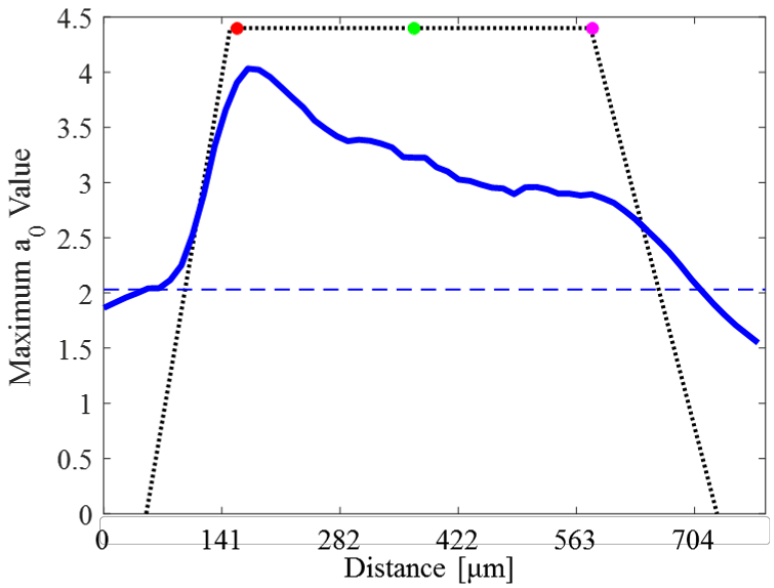

Figure 5. 5: Plot of the a_0 evolution (solid blue curve) as a function of distance in the simulation. The blue dashed curve shows the initial a_0 value launched in this simulation. The plasma density profile is shown by the black dotted line. The wake structure and amount of self-trapped charge due to the a_0 evolution in this simulation is investigated at the start of the constant-density region (marked by the red point), the center of the plasma (marked by the green point), and just before the density downramp (marked by the magenta point). The results of this analysis are presented in Figure 5. 6

A snapshot of the wake structure just after the laser has entered the constant-density region of the plasma is shown in Figure 5. 6(a). By this point in the simulation, the value of a_0 has evolved from 2.03 to 3.9 as seen in Figure 5.5. The first bucket of the wake has formed and though not shown, charge from the inner-shell N electrons is being trapped. However, no self-trapping of the He electrons that form the background plasma has yet occurred despite the substantial increase of a_0. This lack of self-trapping can be seen in Figure 5. 6(a) by the absence of a bunch of He electron

in the first bucket of the wake. Halfway through the constant-density region of the plasma (Figure 5. 6(b)), the wake structure has evolved to a larger radius. The maximum a_0 value has fallen to 3.2, and there is still no self-trapping of He electrons. Just before the plasma density downramp, the wake has evolved further (Figure 5. 6(c)), and the a_0 value has fallen to 2.9 as seen in Figure 5.5. At this point in the simulation, there are some He electrons that have gained energies exceeding 2.5 MeV. These electrons are marked by the colored points in Figure 5. 6(c), where the color bar indicates the energy of the electrons. Though these electrons have gained some energy as they slip back relative to the wake, few of them are in the correct position of the wake to be trapped. The amount of self-trapped charge at the end of the simulation is 0.04% of the amount of ionization-injected charge.

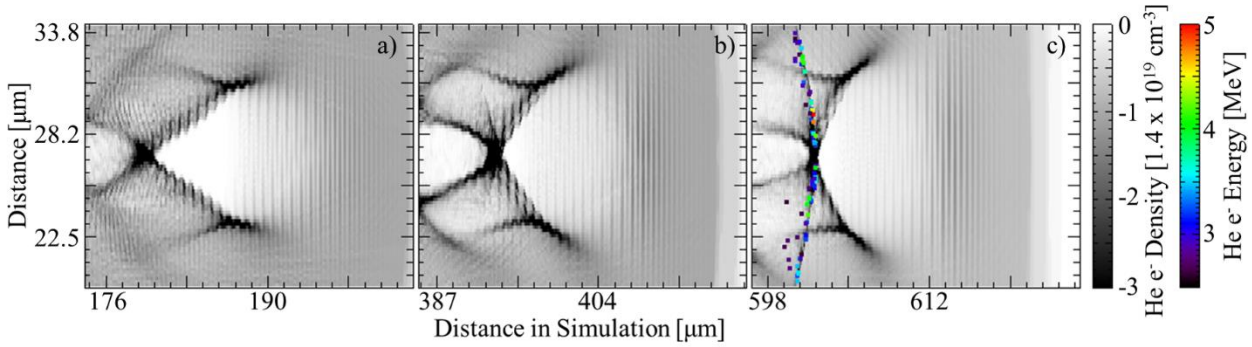

Figure 5. 6: (a-c) Density plots of the plasma electrons from the ionization of the neutral He that makes up the wake structure at (a) the start of, (b) halfway through, and (c) at the end of the constant-density region of the simulation. These locations are marked in Figure 5. 5 by the red, green, and magenta dots, respectively. The points in (c) mark the locations of He electrons that have gained more than 2.5 MeV of energy and are color coded by their energy.

The simulation was run to completion once to identify and tag 550 random electrons that were accelerating in the first bucket of the wake and that exited the plasma. The simulation was subsequently re-run to record the position, momentum, and fields sampled by each tagged electron at each time step of the simulation. To unravel the relative contributions of DLA and LWFA to the total energy gain of the electrons, the energy gain of these tracked electrons due to LWFA and

DLA was calculated using Equations 2.1 and 2.2, respectively. The LWFA and DLA contributions are plotted as a function of the final electron energy in Figure 5. 7. The best linear fits through those contributions show that the curves intersect at 25 MeV. Below this energy, the final energy of the electrons is primarily dominated by LWFA, and above this energy, DLA becomes the dominant contribution.

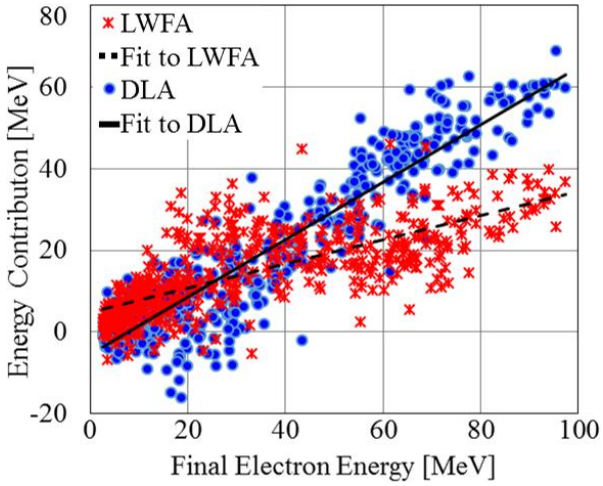

Figure 5. 7: Plot of the DLA contribution $W_{\perp}$ (blue circles) and the LWFA contribution $W_{\parallel}$ (red stars) to the final energy of each of the 550 random electrons versus their final energies. The solid curve shows the best linear fit $E_{DLA} = 0.70\ E_{final} - 5.36$ [MeV] with an R^2 fit of 0.88 for the DLA contribution, and the dashed curve shows the best linear fit $E_{LWFA} = 0.30\ E_{final} + 4.77$ [MeV] with an R^2 fit of 0.57 for the LWFA contribution.

As Figure 5. 7 shows, at final electron energies greater than 90 MeV, where we observed the forked structure in the experimental spectrum (Figure 5. 4(b)), the electrons have gained almost 2/3 of their energy from DLA. Because the energy gain from DLA relies on the coupling between the transverse laser field and the betatron motion of the electrons, a signature of this transverse coupling should be present in the energy gain of the electrons in the simulations as well. Indeed, as shown in Figure 5. 8(a), when the electron beam from the simulation is dispersed perpendicularly to the laser polarization, it shows a forked structure similar to the experimental case in Figure 5. 4(b). Such a fork has been observed in simulations with T_p values between 0.8 -

1.4 but is not present in simulations (Figure 5. 9) where the laser pulse does not overlap the trapped electrons ($T_p \leq 0.5$). In Figure 5. 8(b), the randomly-tagged electrons with energies 40 MeV and above are superimposed on a contour plot of the data shown in Figure 5. 8(a). These electrons are color coded by their DLA contribution to the final energies. Those electrons that fall within the fork structure have the highest DLA contributions, and thus the fork shows a clear signature of DLA that was also seen in the experimental results of Figure 5. 4(b). The origin of the forked structure becomes evident when the transverse structure of the electron beam is examined. When DLA is present in a LWFA, the higher-energy electrons owe a significant portion of their energy to DLA. Consequently, as seen in the inset of Figure 5. 8(c), they tend to bunch at the extrema of their large-radii betatron oscillations [5] and therefore will exit the plasma with a transverse separation, which leads to a forked structure. Additional 3D simulations (Figure 5. 10) show that the center-peaked transverse shape of the experimental data shown in Figure 5. 4(b) and Figure 5. 4(c) is a signature of LWFA being the dominant energy mechanism for the lower-energy electrons. For further comparison with the experimental data, in Figure 5. 8(c), the simulated electron beam was dispersed in the direction of the laser polarization. Similar to the experimental case shown in Figure 5. 4(a), the electron beam has a continuous energy spread and a narrow divergence. When the electron beam is dispersed in the same direction of the laser polarization, any structure associated with the enhanced oscillation of the electrons in the direction of the laser polarization cannot be discerned.

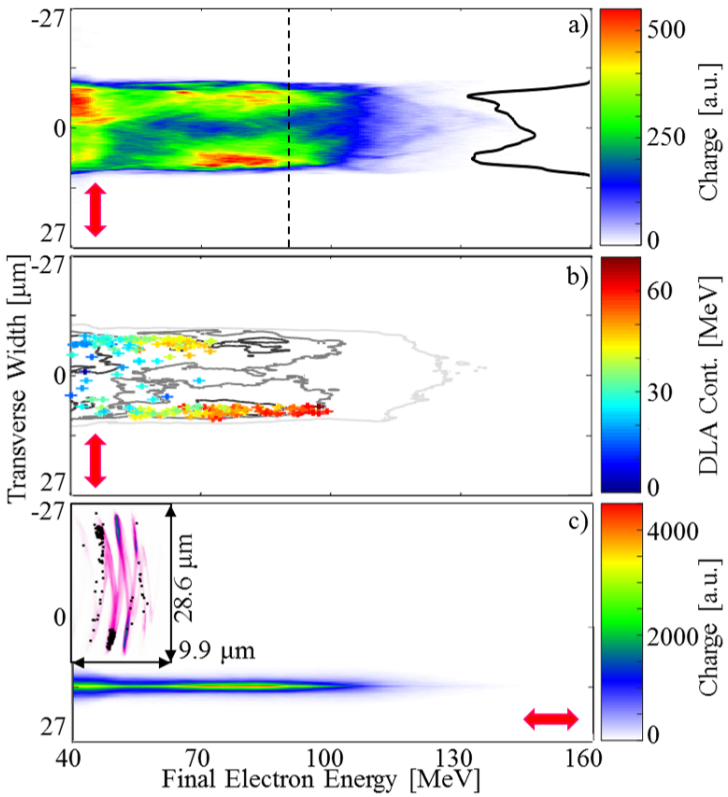

Figure 5. 8: (a) Simulated electron spectrum perpendicular to the linear laser polarization (red arrows). The black curve shows the lineout of the forked structure at 90 MeV, which is marked by the black dashed line. (b) Contour plot of (a) showing the 4% (light grey line), 35% (dark grey line), and 61% (black line) contours. Crosses represent the randomly-tagged electrons with energies over 40 MeV and are color-coded by their DLA contribution. (c) Simulated electron spectrum parallel to the linear laser polarization. (Inset) Transverse profile of electron beam showing the electrons were primarily bunched at the extrema of their betatron oscillations when exiting the plasma. Black dots mark the randomly-tagged electrons with energies over 40 MeV.

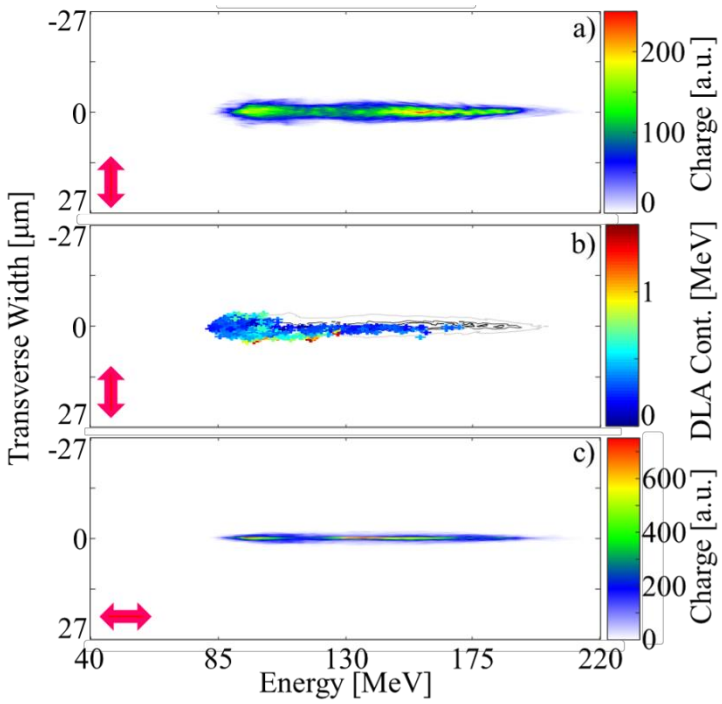

Figure 5. 9: (a) Simulated electron spectrum perpendicular to the linear laser polarization (red arrows) for a simulation where $T_p = 0.4$. This figure shows that no fork structure exists when the electrons do not overlap the drive laser pulse. (b) Contour plot of (a) showing the 8% (light grey line), 40% (dark grey line), and 60% (black line) contours. The crosses represent the randomly-tagged electrons with energies over 40 MeV and are color-coded by their DLA contribution. The maximum DLA contribution in this case is 1.5 MeV, and DLA contributes no more than 1.5% of the energy to any given tagged electron. (c) Simulated electron spectrum parallel to the linear laser polarization. Parameters for this simulation were: $a_0 = 2.1$, $\tau_{laser} = 25$ fs, $\lambda_0 = 815$ nm, $w_0 = 6.7$ μm, $n_e = 8 \times 10^{18}$ cm^{-3}, plasma length = 1 mm with 100 μm up- and downramps.

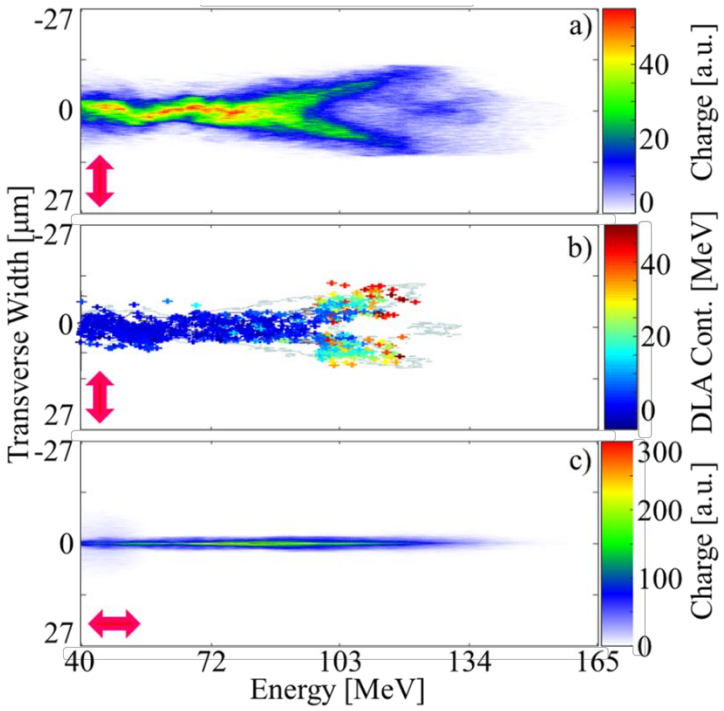

Figure 5. 10: (a) Simulated electron spectrum perpendicular to the linear laser polarization (red arrows) for a simulation where $T_p = 0.8$. (b) Contour plot of (a) showing the 18% (light grey line), 44% (dark grey line), and 74% (black line) contours. Crosses represent the randomly-tagged electrons with energies over 40 MeV and are color-coded by their DLA contribution. This figure shows that the on-axis charge, such as that seen in the experiment (Figure 5. 4), was primarily accelerated by the wake. The fork structure arises when DLA begins to make a sizeable contribution. (c) Simulated electron spectrum parallel to the linear laser polarization. Parameters for this simulation were: $a_0 = 2.1$, $\tau_{laser} = 45$ fs, $\lambda_0 = 815$ nm, $w_0 = 6.7$ μm, $n_e = 8 \times 10^{18}$ cm^{-3}, plasma length = 1 mm with 100 μm up- and downramps.

Like the experimental electron spectrum shown in Figure 5. 4(b), the transverse shape of the simulated spectrum in Figure 5. 10(a) transitions from a center-peaked feature to a forked feature. This electron beam spectrum was produced from a 3D OSIRIS simulation that had the same physical parameters as the simulation that produced Figure 5. 8 except that a_0 was 2.1, the plasma density was 8×10^{18} cm^{-3}, and the constant-density region of the plasma was 1 mm long.[1] 1,080 electrons were tracked in this simulation, and their final transverse position and energy are plotted on the contour plot of Figure 5. 10(a) in Figure 5. 10(b). These tracked electrons are color coded by their DLA contribution, which again was calculated using Equation 2.1. Figure 5. 10(b)

[1] We note that although simulations with plasma densities of 8×10^{18} cm^{-3} have produced forks, we have not yet observed forks for these densities in experiment. For our particular experimental parameters, the number of DLA electrons at these densities are likely too low in number to detect.

shows that for final electron energies below ~ 95 MeV, where the transverse shape of the electron spectrum is peaked at the center, the DLA contribution to the final electron energies is 15 MeV or less. Rather, the center-peaked charge at lower energies, which was also seen in the experimental data in Figure 5. 4(b), is predominately accelerated by the wake. Beginning at final electron energies ~ 95 MeV, the DLA contribution to the electron energy increases, and the electron spectrum splits into a forked structure similar to the one seen in the experimental data (Figure 5. 4(b)). Thus, this simulation again shows that the fork structure is a characteristic spectral signature when DLA contributes to the energy gain of the electrons in a LWFA.

As was shown in the inset of Figure 5. 8, in a LWFA where DLA is present, the transverse structure of the accelerating electron beam becomes modulated at the half laser wavelength. For the simulation case shown in Figure 5. 8, the value of T_p was 1.0, and the laser filled the entire first bubble of the wake and strongly overlapped all the accelerating charge. This strong overlap resulted in a large transverse charge separation for all the energies of the produced electron beam as shown in Figure 5. 8(a) and Figure 5. 8(b). For the simulation case shown in Figure 5. 10, the T_p value was 0.8. This slightly lower value of T_p means that the accelerating charge in the back of the first bubble is only overlapped by the falling intensity of the laser pulse. The transverse density profile of the electron beam for the $T_p = 0.8$ simulation is shown in Figure 5. 11(a). The head of this electron beam overlaps a high-intensity portion of the laser pulse and similar to the electron beam in the inset in Figure 5. 8, it is strongly modulated at the half-laser wavelength and the charge is bunched at the extrema of the betatron oscillations. This bunching causes the charge at the front portion of the electron beam to exit the plasma with some transverse separation, which leads to the fork seen in Figure 5. 10(a) and Figure 5. 10(b). The laser intensity falls from the head of the electron beam to its tail, and consequently the modulation at the half-laser wavelength

becomes less pronounced and the charge is no longer bunched at the extrema of the betatron oscillations. At the tail of the electron beam, the energy contribution of DLA to the overall charge of the electrons is small, and there is only a small transverse modulation of the accelerated charge. Though this transverse modulation is small at the tail of the beam, it leads to the serpentine structure in the dispersed electron beam in Figure 5. 10(a) for the lower electron energies (40 MeV to ~ 95 MeV). In Figure 5. 11(b), the transverse structure of the electron beam is this time shown using a sampling of the electrons from the $T_p = 0.8$ simulation color-coded by their final energy. Figure 5. 11(b) shows that there is a general correlation between the position of the electrons in the beam and their energies. The higher-energy electrons are predominantly found at the head of the electron beam, and the lower-energy electrons are predominantly found at the tail. For the lower-energy electrons, each half oscillation in the transverse structure contains electrons in different bins of final energies. For example, the charge slightly above the laser axis at the point marked "I" has final energies ~ 40 MeV, the charge at "II" had ~ 50 MeV, the charge at "III" has ~ 70 MeV and so on. These steps in final energy associated with a given transverse position mean that the different-energy electrons will exit the plasma with slightly different transverse positions and divergences, which produces the serpentine structure when the electron beam is dispersed orthogonal to the direction of the laser polarization as seen in the center-peaked electron feature for energies from 40 MeV to ~ 95 MeV in Figure 5. 10(a). This serpentine structure is absent when the electron beam is dispersed in the direction of the laser polarization as seen in Figure 5. 10(c).

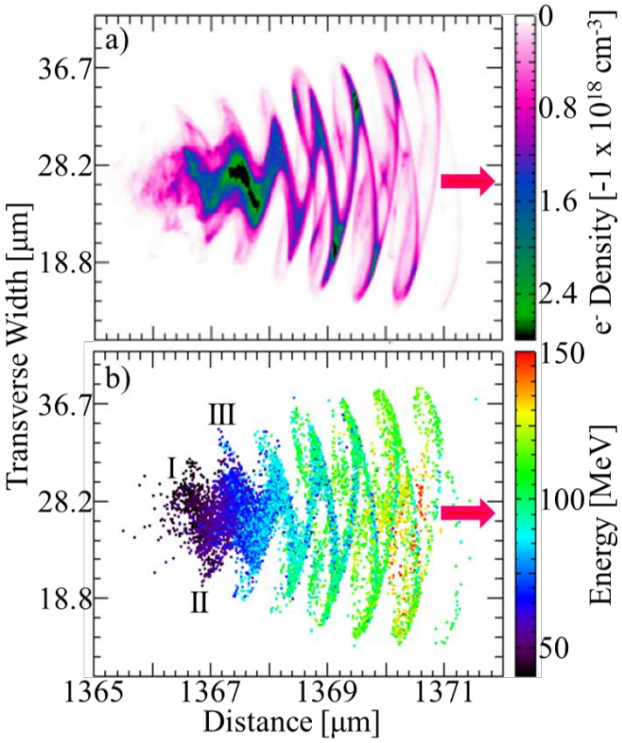

Figure 5. 11: (a) Transverse density profile of electron beam after propagating 100 μm in vacuum from the T_p = 0.8 simulation used to generate Figure 5. 10. (b) Transverse profile of the same electron beam as in (a) showing a sampling of 0.04% of the total electrons in the simulation color coded by their final energy. The red arrow marks the direction of the electron beam propagation in both.

In addition to the serpentine structure in the dispersed spectrum for electron energies below ~ 95 MeV, Figure 5. 10(a) and Figure 5. 10(b) have a second, small forked structure in the interior of the large fork at an energy of approximately 125 MeV. As already discussed, the main fork structure in Figure 5. 8 and Figure 5. 10 arises because the electrons are bunched at the extrema of their betatron oscillation and exit the plasma with a transverse separation but a small divergence. The secondary fork in Figure 5. 10(a) and Figure 5. 10(b) also arises due to the betatron motion of the electrons. However, this fork is formed differently. The electrons that form this fork are also executing large-radii betatron oscillations. However, they are phased one quarter of a betatron period from those that form the main fork. Therefore, unlike the electrons that form the main fork, which exit the plasma with a large transverse separation but small divergence, these electrons exit

the plasma with a small transverse separation but with a large divergence. Because the electron beam spectrum from the simulation is calculated 100 μm after the exit of the plasma, these electrons are captured as they cross the betatron axis due to their large divergence. However, such electrons would not be captured in our experiment because their divergence is so large that they would be lost during the transport to the detector.

Conclusion

In conclusion, in this Chapter, we have demonstrated experimentally and through supporting simulations that when there is a significant overlap between the trapped electrons and the laser ($T_p \sim 1$) in a LWFA cavity, the resulting electrons can gain energy from both the LWFA and the DLA mechanisms. In fact, the DLA mechanism can provide comparable energy to the LWFA mechanism.

Ch. 5 References

[1] W. P. Leemans et al., Phys. Rev. Lett. **68**, 3 (1992).

[2] A. Pak et al., Phys. Rev. Lett. **104**, 025003 (2010).

[3] C. E. Clayton et al., Phys. Rev. Lett. **105**, 105003 (2010).

[4] G. Z. Sun et al., Phys. Fluids **30**, 526 (1987).

[5] J. L. Shaw et al. Plasma Phys. Contr. F. **58**, 034008 (2016).

Ch. 6: Conclusion

In this dissertation, the direct laser acceleration (DLA) of electrons in a laser wakefield accelerator (LWFA) operating in the forced or quasi-blowout regimes has been investigated through experiment and simulation. We have demonstrated that when there is a significant overlap between the trapped electrons and the laser ($T_p \gtrsim 1$) in a LWFA cavity, the resulting electrons can gain energy from both the LWFA and the DLA mechanisms. In the experimental work, we investigated the properties of the electron beams produced in a LWFA with ionization injection by dispersing those beams in the direction perpendicular to the laser polarization. We found that these electron beams show certain features (ellipticity in the plane of the laser polarization and an energy spectrum that splits into a fork at higher energies when the beam is dispersed orthogonal to the laser polarization direction) that are characteristic of DLA. Furthermore, because the fork-like structure appears for the higher-energy electrons, it suggests that DLA is an additional acceleration mechanism for these electrons. These characteristic spectral features were reproduced in OSIRIS simulations, where particle tracking was used to demonstrate that such spectral features are signatures of the presence of DLA in LWFA.

Through additional simulation work, it was found that the onset of DLA in a LWFA typically occurs for T_p values > 0.5 when ionization injection is used. The contribution of DLA to the energy gained by the electron was calculated in simulations. Its magnitude was found to be on the order of the LWFA contribution and actually exceeded the LWFA contribution to the highest-energy electrons in some cases. It was also shown that in the LWFAs studied here, both DLA and LWFA participate in accelerating the bulk of the electrons in the produced electron beam. The presence of DLA in a LWFA can lead to enhanced betatron oscillation amplitudes and

increased divergence in the direction of the laser polarization. Additionally, it was shown through simulations that in a LWFA system where both the properties of the electrons and the properties of the drive laser are evolving, trapped electrons can gain energy from DLA for extended acceleration distances.

The DLA process in LWFA can be optimized further in the future. One potential path to optimizing DLA in LWFA would be to tailor the laser profile to enhance the DLA. For example, the drive laser could be chirped so that the quasi-resonance required for energy gain from DLA is better maintained [1-3]. The two-laser DLA scheme presented by Zhang et al. [4, 5] could be tested experimentally to see if it permits better control of the DLA process in LWFA. The effect of ion motion on DLA in a LWFA could be explored through further simulations. Additionally, the gas mix used for ionization injection could be better tailored to trap charge farther forward in the wake. Though such electrons would gain less energy from LWFA, they would overlap with a larger laser amplitude and therefore should gain more energy from DLA. DLA could also be explored in LWFA experiments that employ other injection schemes [6, 7]. Finally, it would be very interesting to investigate whether DLA could be introduced in a beam-driven plasma wakefield accelerator (PWFA) cavity using an intense laser pulse that trails the particle bunch that drives the wake.

The presence of DLA in LWFA provides insight into possible reasons why the overall quality (i.e. emittance, divergence, energy spread) of the electron beams produced from LWFA experiments is not always competitive with that from conventional radiofrequency accelerators. Although DLA-assisted LWFA can lead to maximum electron energies greater than those provided by LWFA alone, the energy gain from DLA relies on the coupling between the transverse laser field and the betatron motion of the electrons, which causes the transverse momentum of the

electrons to be larger than in a LWFA-only case. This increased transverse momentum can lead to an increase in the divergence of the electron beam in the direction of the laser polarization. Additionally, because the energy gain due to DLA varies depending on the magnitude of the transverse laser field sampled by the electron as well as whether or not that electron is able to gain energy from DLA for extended acceleration distances, DLA can contribute to energy spread in LWFA systems such as those studied here. Understanding that DLA can play a role in LWFA systems may provide a path for such experiments to improve the emittance, divergence, and energy spread of their LWFA-produced electron beams if that is a major goal of such experiments. It will also allow DLA to be exploited in future LWFA experiments, such as betatron x-ray experiments, where the maximum energy of the produced electron beams is the primary outcome.

Not only can DLA enhance the maximum energy of the accelerating electrons in a LWFA, but it can also lead to an increase in the amplitude of the betatron oscillations of those electrons. The critical energy of the betatron x-ray spectrum emitted by electrons in a LWFA scales as $\gamma^2 r_0$, where r_0 is the amplitude of the betatron oscillation, and its radiated power scales as $\gamma^2 r_0^2$. If we consider the more than 5X increase in r_0 due to DLA that was presented in Section 2.3, we see that the critical energy would increase by a factor of 5 and the radiated power by a factor of 25 due to the change in r_0 alone from DLA. Furthermore, the number of emitted photons scales as $\gamma^{1/2} r_0$ and should therefore increase with the enhanced energy and r_0 from DLA. Thus, DLA shows much promise as a path to enhance the betatron radiation generated from LWFAs. In fact, the role of DLA in betatron x-ray production could have been inferred indirectly from the MV photon emission observed in the forward direction in prior LWFA experiments [8]. The renewed interested in the betatron radiation from LWFAs operating in the SMLWFA regime further motivates additional investigation into the role that DLA plays in betatron radiation [7].

Finally, DLA could also be exploited to microbunch electron beams on femtosecond to attosecond timescales [9]. When DLA is present in a LWFA, the electrons tend to bunch at the extrema of their large-radii betatron oscillations [10]. This bunching is spaced at half of the laser wavelength [1, 9], which can yield electron bunches with temporal durations ~ 1 fs for a LWFA driven by a Ti:Sapphire laser. It may be possible to diagnose this bunching from the (coherent) optical transition radiation that these bunched beams may emit as they exit the plasma-vacuum boundary.

Ch. 6 References

[1] A. Pukhov et al., Phys. Plasmas **6**, 2847 (1999).

[2] A. Pukhov, Reports on Progress in Physics **66**, 47 (2003).

[3] J. L. Shaw et al., *Proceedings of the 2014 Advanced Accelerator Concepts Workshop. http://arxiv.org/abs/1502.07664v1.*

[4] X. Zhang et al., Phys. Rev. Lett. **114**, 184801 (2015).

[5] X. Zhang et al., Plasma Phys. Contr. F. **58**, 034011 (2016).

[6] S. Kneip et al. Phys. Rev. Lett. **100**, 105006 (2008).

[7] N. Lemos et al., Plasma Phys. Contr. F. **58**, 034018 (2016).

[8] S. Cipiccia et al., Nature Physics **7**, 867 (2011).

[9] N. Lemos et al., *Proceedings of the 2014 Advanced Accelerator Concepts Workshop. http://arxiv.org/abs/1502.07764v1.*

[10] J. L. Shaw et al. *Submitted to Phys. Rev. Lett.*

Appendix

Included in the following pages are all the electron spectra with potential fork features. This data was taken by dispersing the electron beam orthogonal to the direction of the laser polarization. The data is sorted by shot day with ascending T_p values. Both the raw and the linearized data are shown for each day, as the fork features look somewhat different in each form. Each spectrum also indicates the T_p value, plasma density, and laser a_0 for that shot. All raw data is stored in the XPL DropBox account.

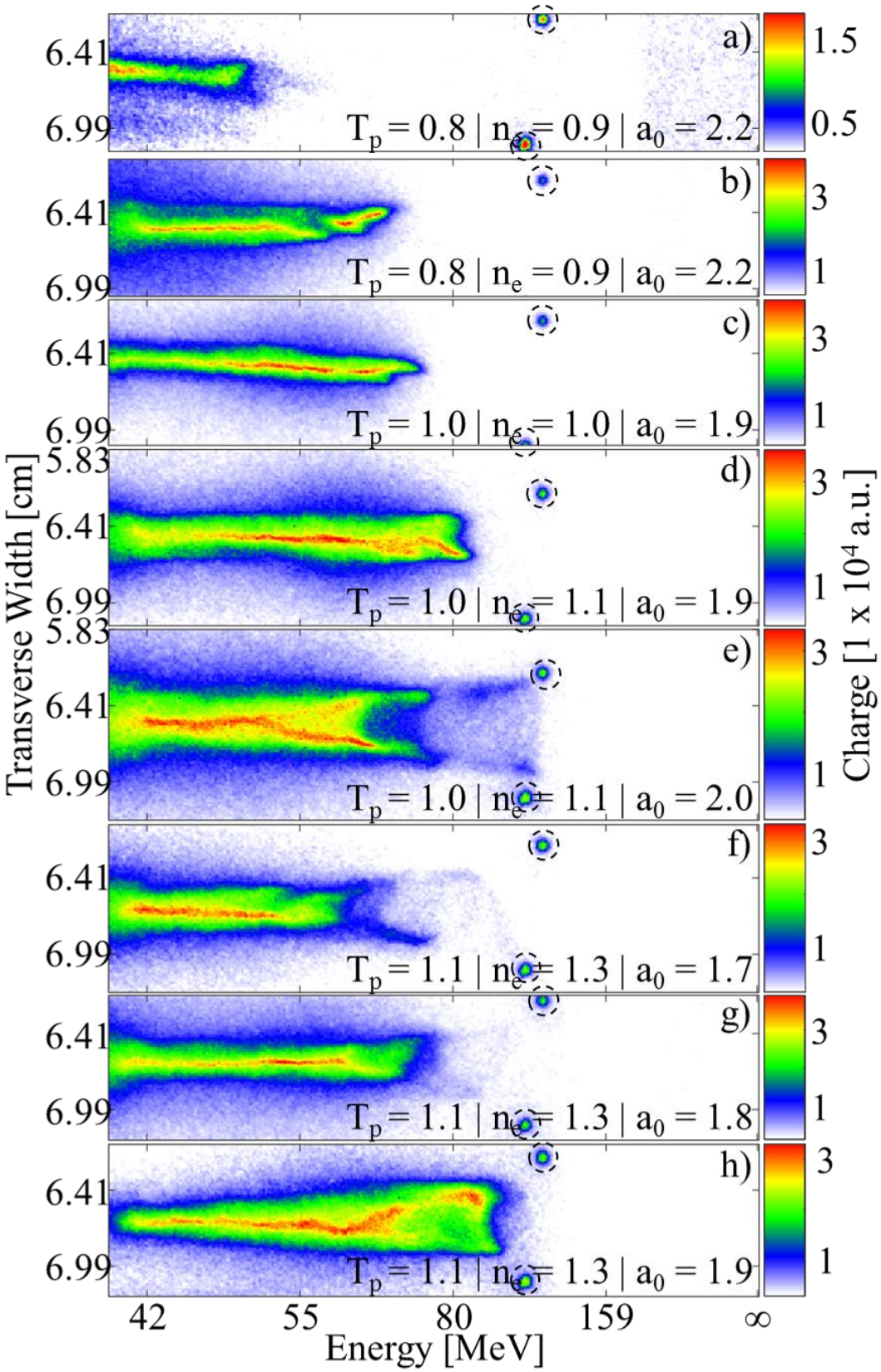

Figure A. 1: Raw data with energy scale taken on June 23, 2015. Dotted circles mark fiducial locations and are not real signal due to electrons.

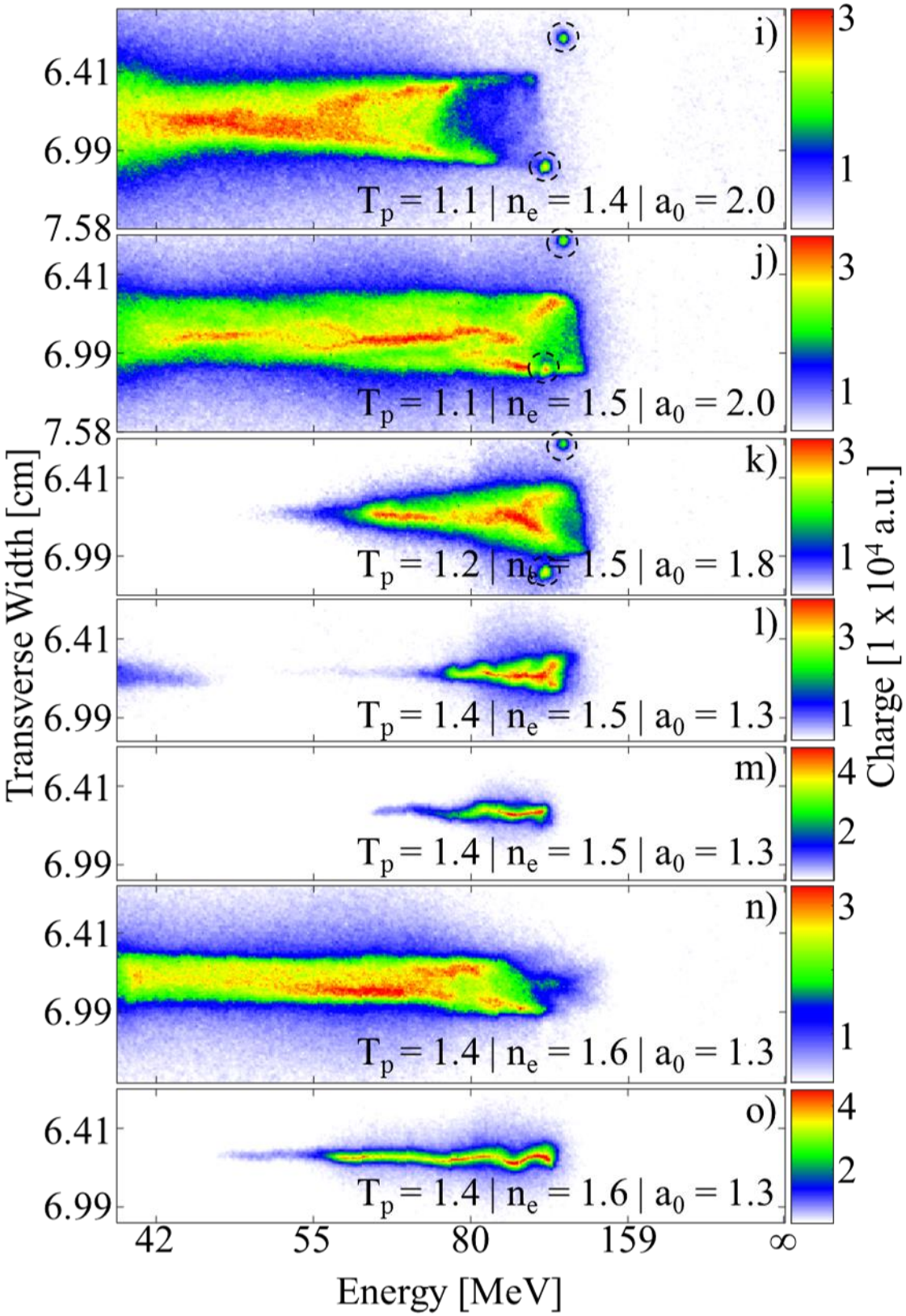

Figure A. 2: Continuation of raw data with energy scale taken on June 23, 2015. Dotted circles mark fiducial locations and are not real signal due to electrons.

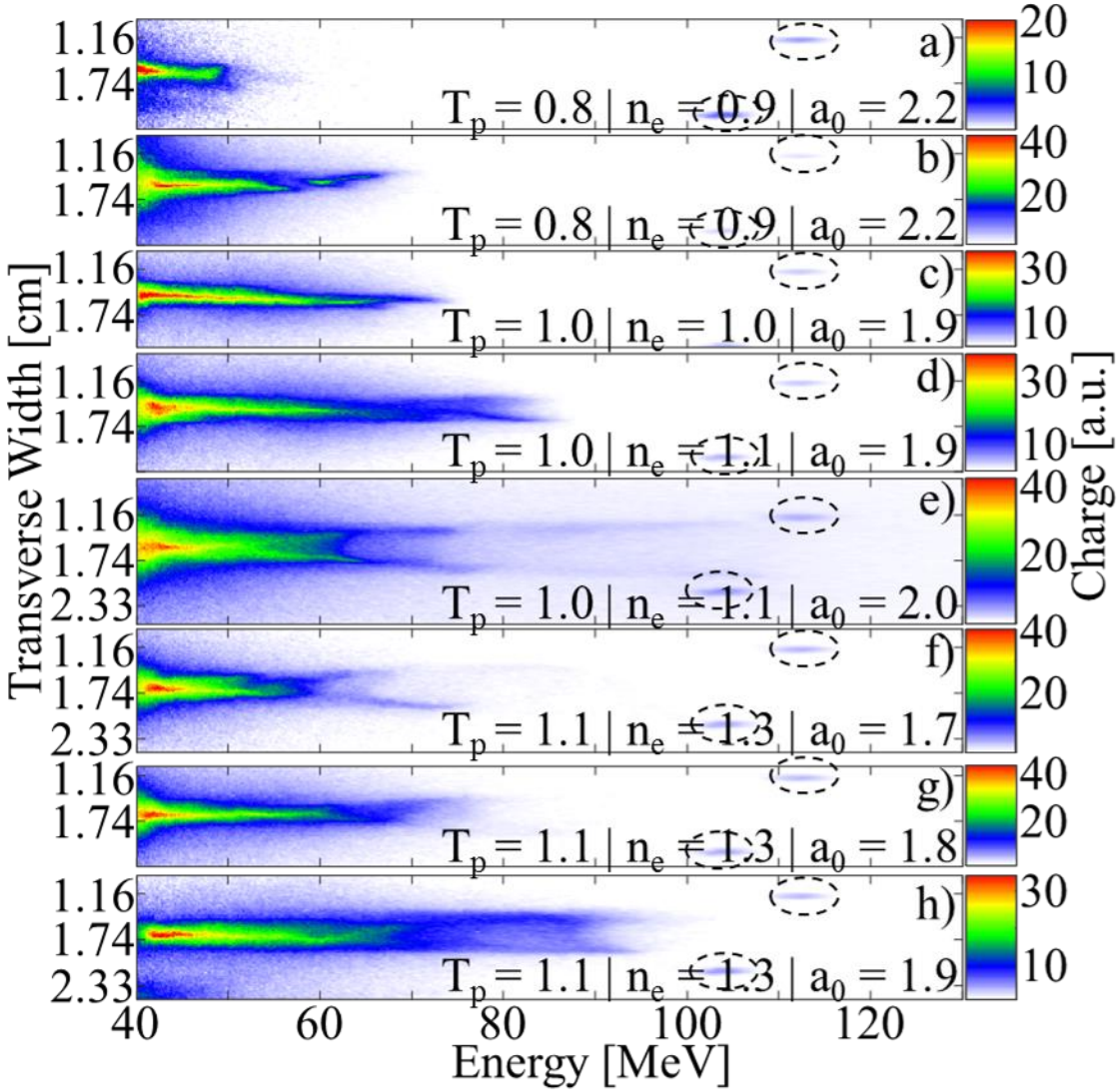

Figure A. 3: Linearized version of the data from Figure A. 1. Dotted ovals mark fiducial locations and are not real signal due to electrons.

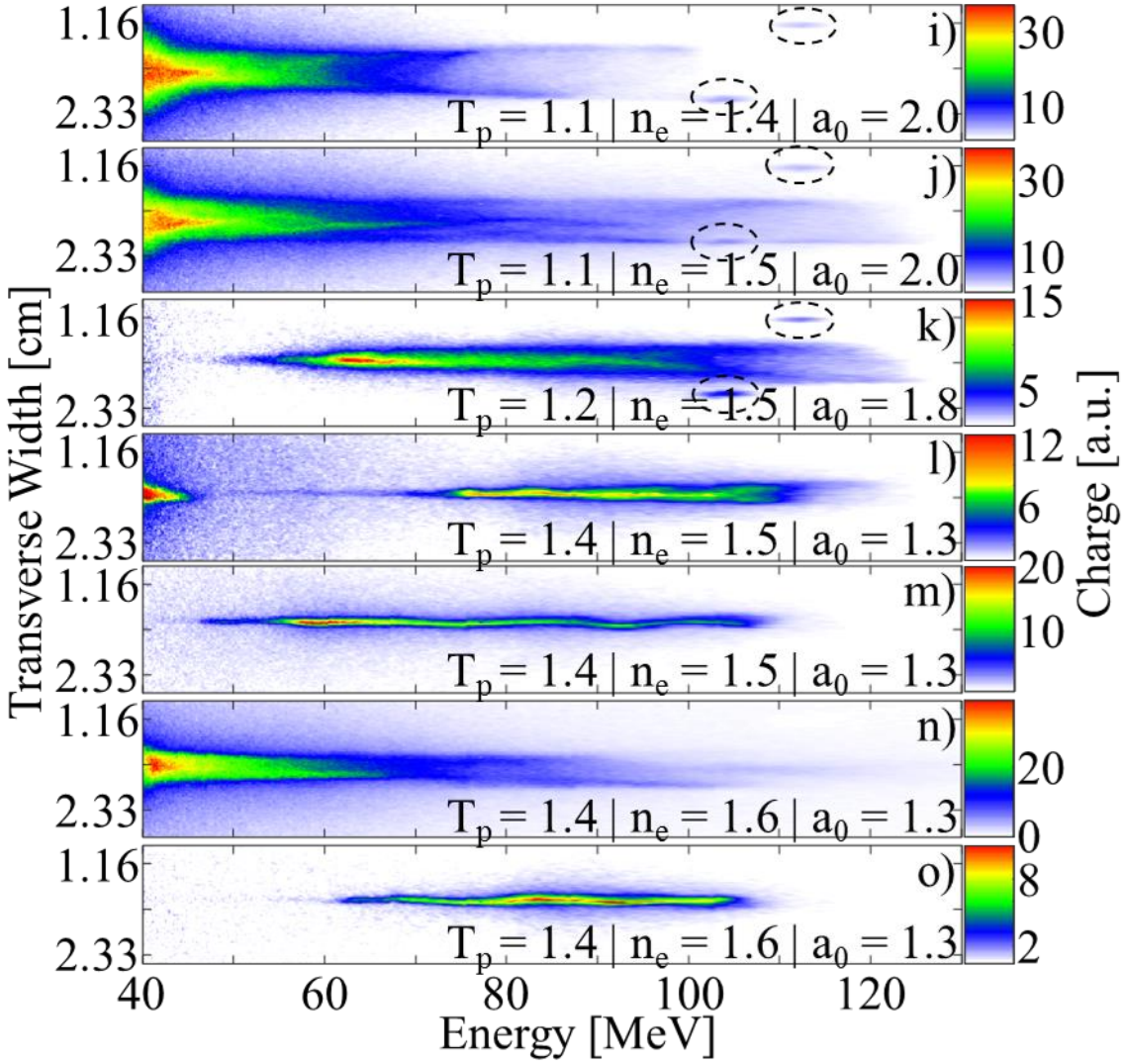

Figure A. 4; Linearized version of the data from Figure A. 2. Dotted ovals mark fiducial locations and are not real signal due to electrons.

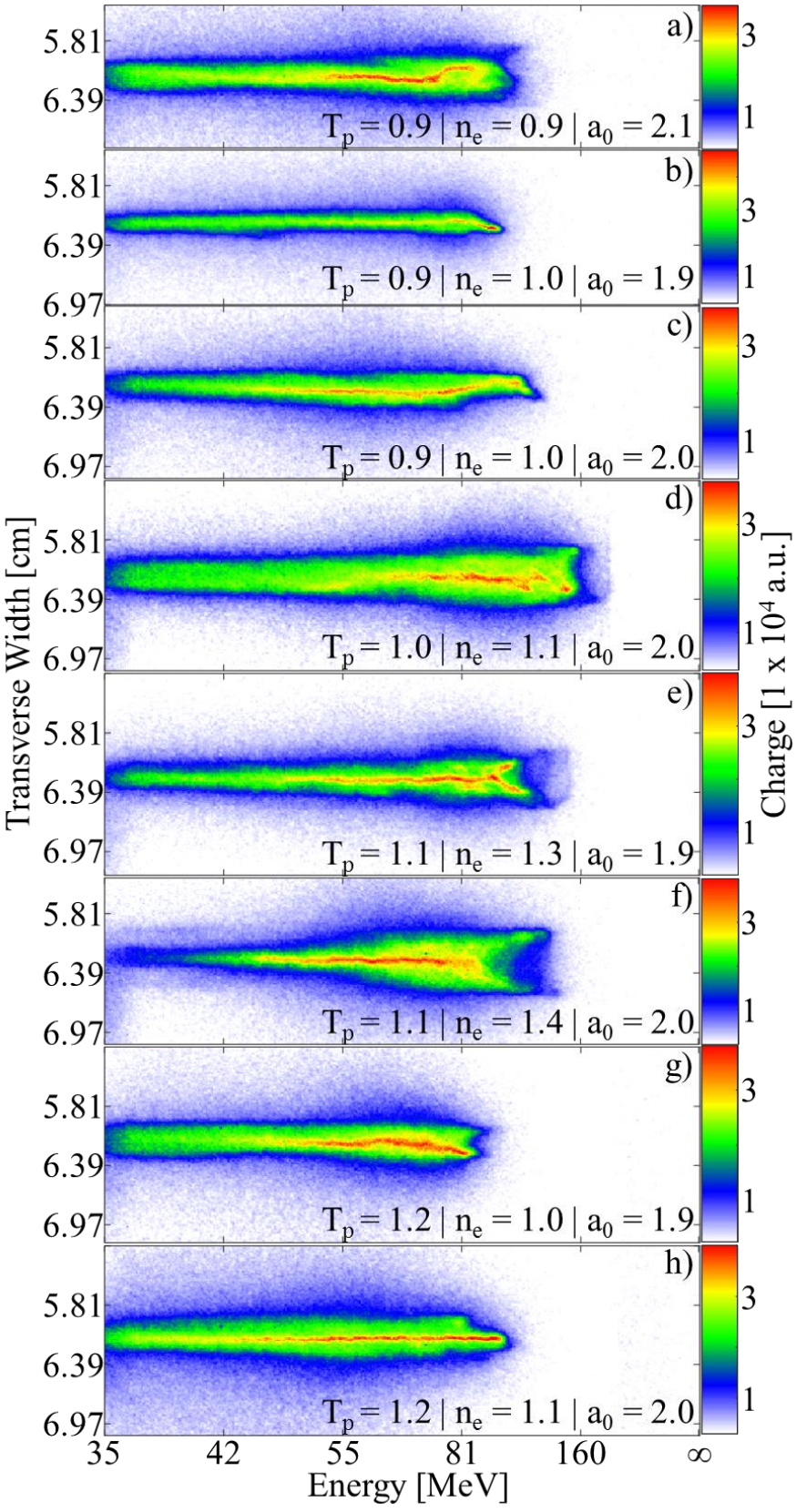

Figure A. 5: Raw data with energy scale taken on July 21, 2015.

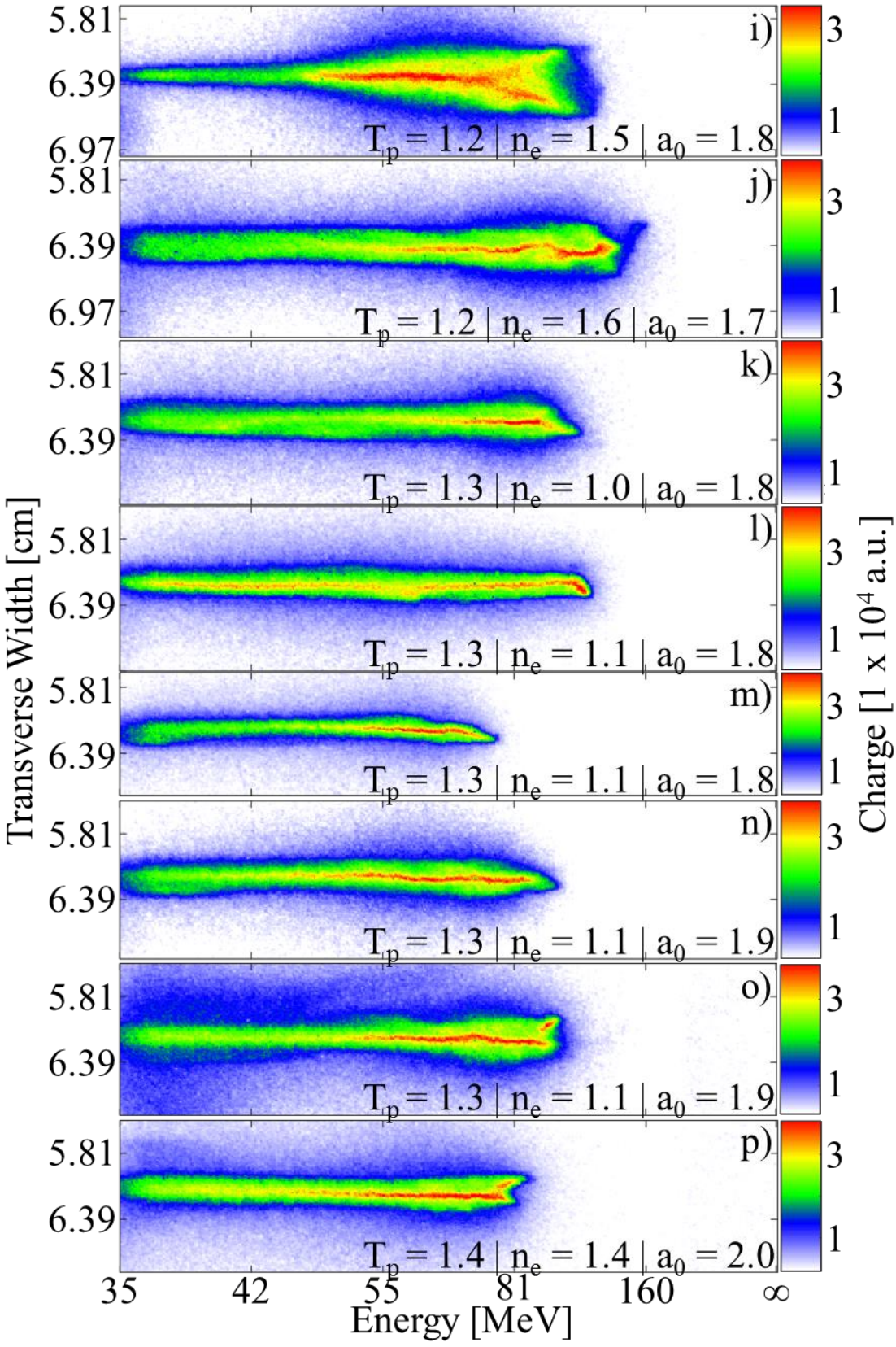

Figure A. 6: Continuation of the raw data with energy scale taken on July 21, 2015.

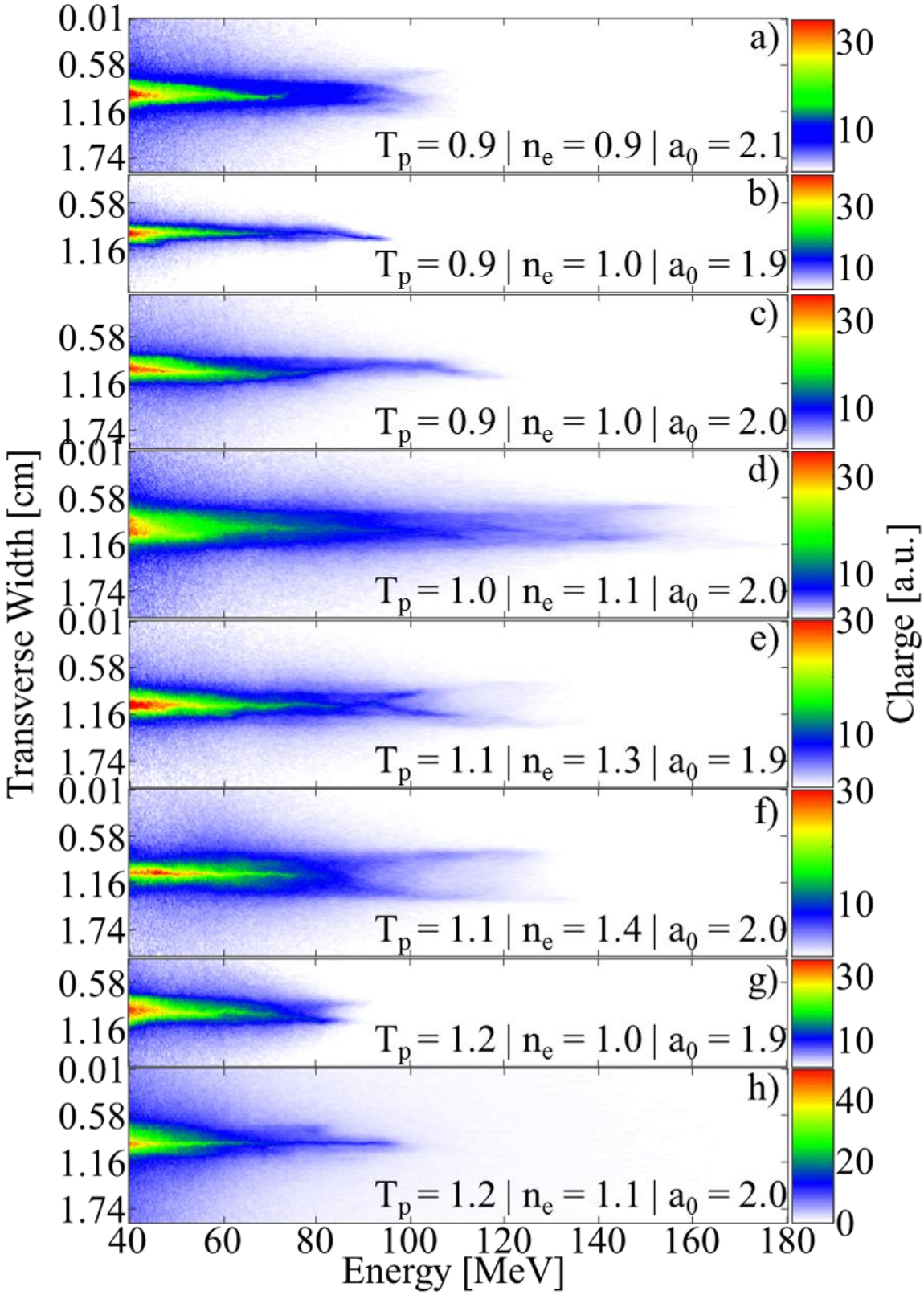

Figure A. 7: Linearized version of the data from Figure A. 5.

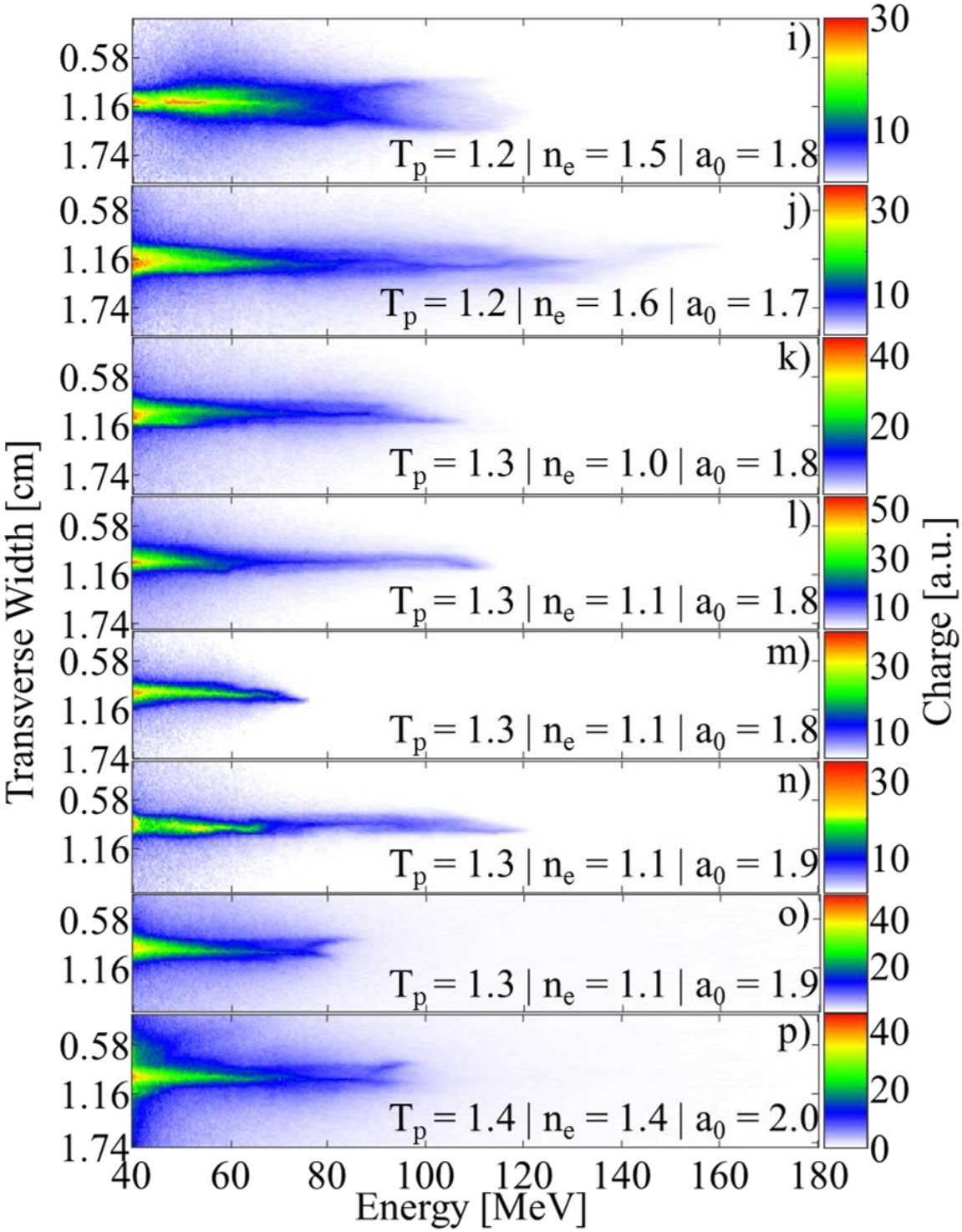

Figure A. 8: Linearized version of the data from Figure A. 6.

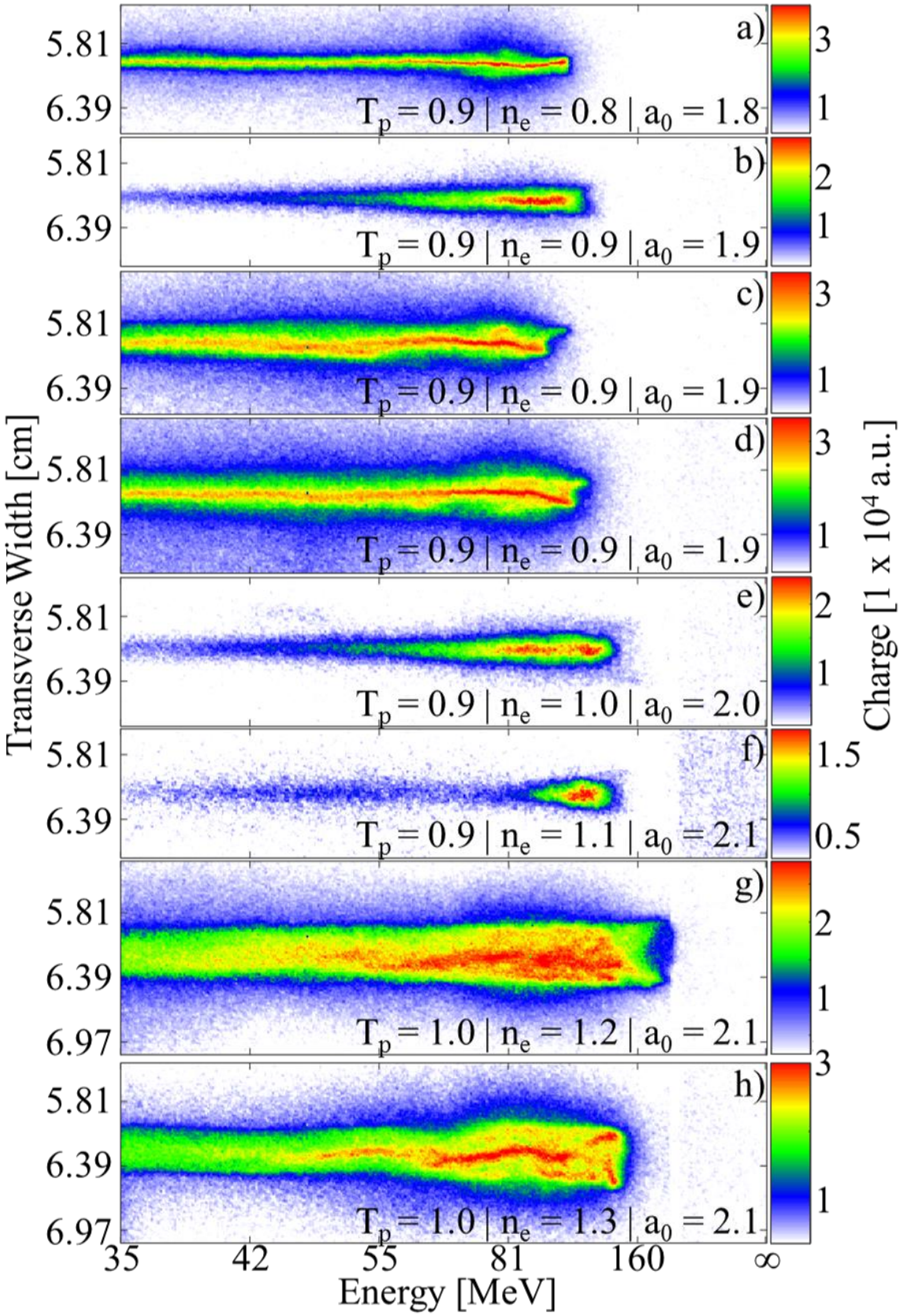

Figure A. 9: Raw data with energy scale taken on July 27, 2015.

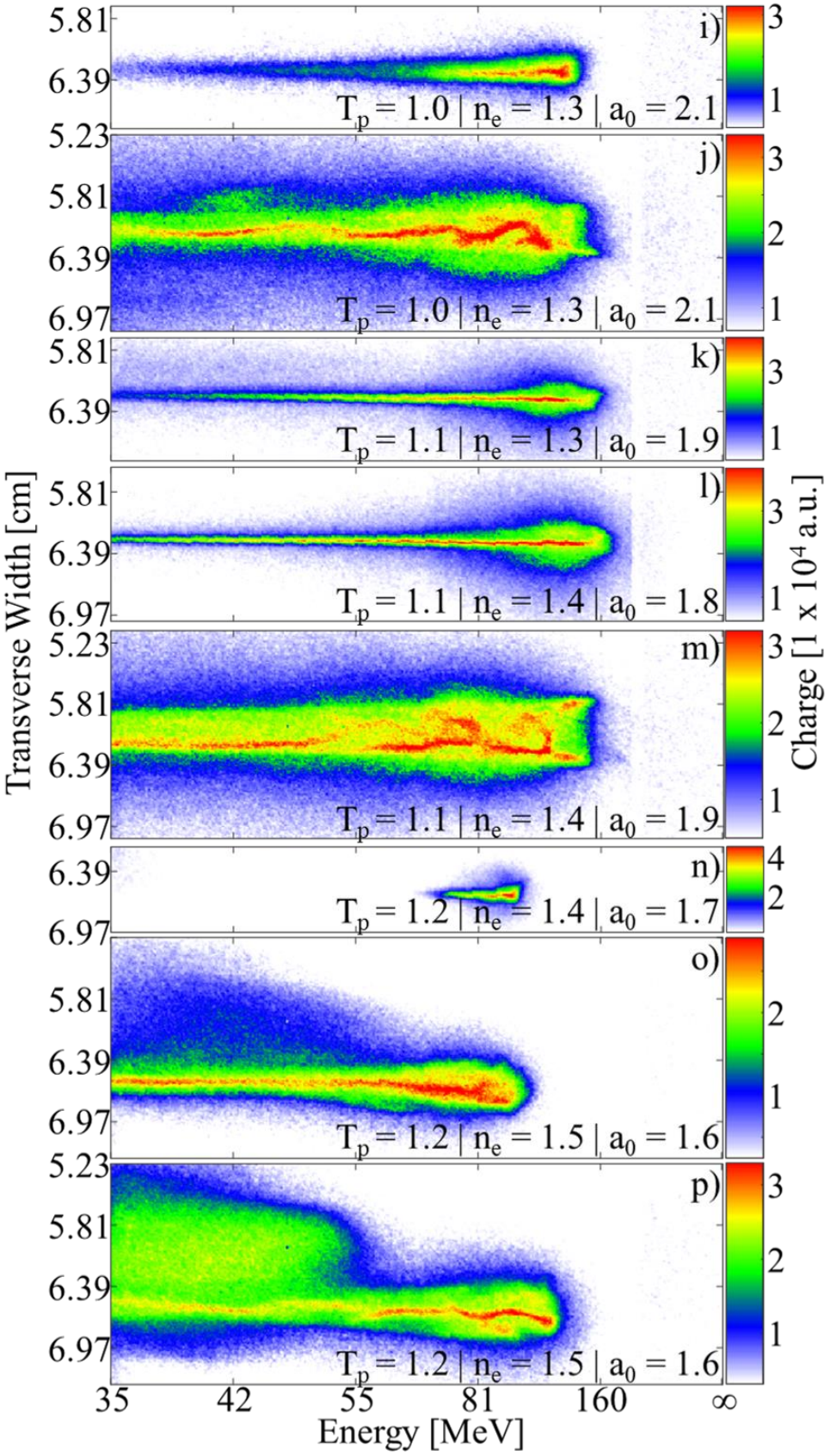

Figure A. 10: Continuation of the raw data with energy scale taken on July 27, 2015.

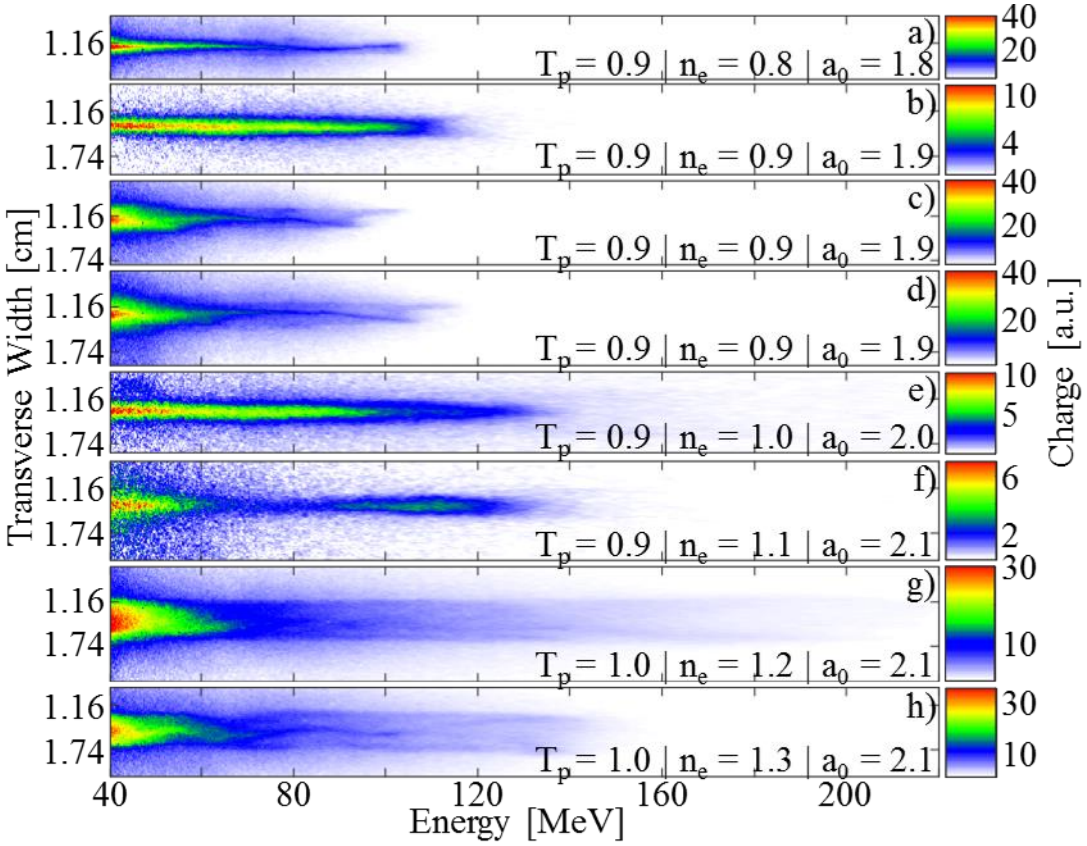

Figure A. 11: Linearized version of the data from Figure A. 9.

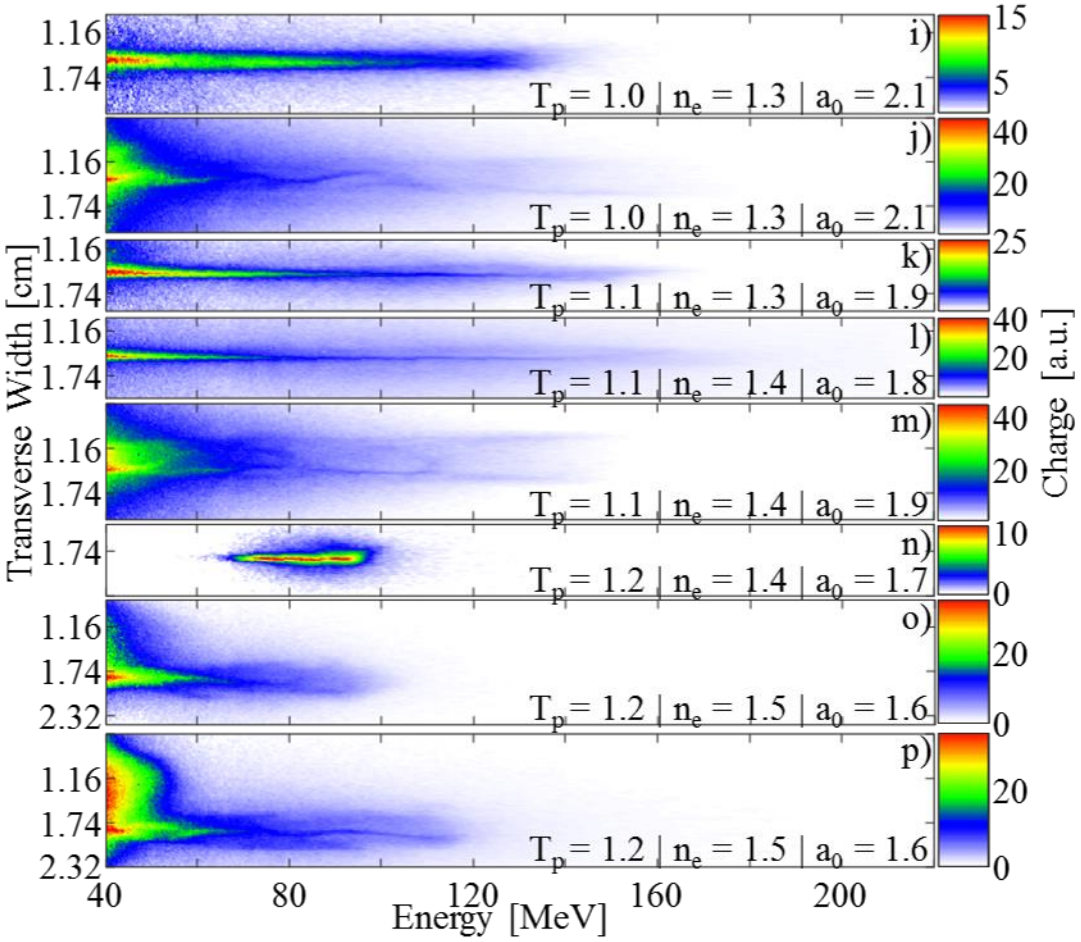

Figure A. 12: Linearized version of the data from Figure A. 10.